

Variational Phase-field modeling of hydraulic fracture interaction with natural fractures and application to Enhanced Geothermal Systems

Baptiste Lepillier¹, Keita Yoshioka², Francesco Parisio³, Richard R. Bakker⁴, and David Bruhn⁵

¹Delft University of Technology

²Helmholtz Centre for Environmental Research UFZ

³Freiberg University Of Mining And Technology

⁴TU Delft

⁵GFZ Potsdam

November 24, 2022

Abstract

In every tight formation reservoir, natural fractures play an important role for mass and energy transport and stress distribution. Enhanced Geothermal Systems (EGS) make no exception and stimulation aims at increasing the reservoir permeability to enhance fluid circulation and heat transport. EGS development relies upon the complex task of predicting accurate hydraulic fracture propagation pathway by taking into account reservoir heterogeneities and natural or pre-existing fractures. In this contribution, we employ the variational phase-field method which handles hydraulic fracture initiation, propagation and interaction with natural fractures and is tested under varying conditions of rock mechanical properties and natural fractures distributions. We run bi-dimensional finite element simulations employing the open-source software OpenGeoSys and apply the model to simulate realistic stimulation scenarios, each one built from field data and considering complex natural fracture geometries in the order of a thousand of fractures. Key mechanical properties are derived from laboratory measurements on samples obtained in the field. Simulations results confirm the fundamental role played by natural fractures in stimulation's predictions, which is essential for developing successful EGS projects.

1 **Variational Phase-field modeling of hydraulic fracture**
2 **interaction with natural fractures and application to**
3 **Enhanced Geothermal Systems**

4 **Baptiste Lepillier¹, Keita Yoshioka², Francesco Parisio³, Richard Bakker¹,**
5 **David Bruhn^{1,4}**

6 ¹Delft University of Technology, Stevinweg 1, Delft 2628CN, The Netherlands

7 ²Department of Environmental Informatics, Helmholtz Centre for Environmental Research – UFZ,
8 Leipzig, Germany

9 ³Chair of Soil Mechanics and Foundation Engineering, Institute of Geotechnics, Technische Universität
10 Bergakademie Freiberg, Germany

11 ⁴GFZ German Research Centre for Geosciences, Telegrafenberg, Potsdam, Germany

12 **Key Points:**

- 13 • A novel approach for reservoir stimulation applied to an Enhanced Geothermal
14 System.
15 • A robust numerical modeling of hydraulic fracture propagation and interaction
16 with natural pre-existing fractures modeled using the variational Phase-field.
17 • The numerical model is applied to the field case of Acoculco geothermal reservoir.

Abstract

In every tight formation reservoir, natural fractures play an important role for mass and energy transport and stress distribution. Enhanced Geothermal Systems (EGS) make no exception and stimulation aims at increasing the reservoir permeability to enhance fluid circulation and heat transport. EGS development relies upon the complex task of predicting accurate hydraulic fracture propagation pathway by taking into account reservoir heterogeneities and natural or pre-existing fractures. In this contribution, we employ the variational phase-field method which handles hydraulic fracture initiation, propagation and interaction with natural fractures and is tested under varying conditions of rock mechanical properties and natural fractures distributions. We run bi-dimensional finite element simulations employing the open-source software OpenGeoSys and apply the model to simulate realistic stimulation scenarios, each one built from field data and considering complex natural fracture geometries in the order of a thousand of fractures. Key mechanical properties are derived from laboratory measurements on samples obtained in the field. Simulations results confirm the fundamental role played by natural fractures in stimulation's predictions, which is essential for developing successful EGS projects.

1 Introduction

Interest in predicting Hydraulic Fracture propagation is picking up since the Enhanced Geothermal System (EGS) concept could become a competitive solution as a sustainable and essentially carbon-free energy resource. In EGS, the reservoir is stimulated by injecting pressurized fluids in reservoir rock formations with the aim of enhancing permeability. Early application of permeability enhancement were performed in oil and gas reservoirs (Economides & Nolte, 1989) while nowadays the principles of hydraulic fracture mechanics are applied to a broad range of problems, such as nuclear waste disposal (Zoback et al., 2003), carbon-capture storage (Fu et al., 2017), glacier dynamics (Tsai & Rice, 2010), earthquake nucleation (D. I. Garagash & Germanovich, 2012) and geothermal systems (Legarth & Saadat, 2005; McClure & Horne, 2014; Fox et al., 2013). Hydraulic fracture propagation is intrinsically a multi-scale problem (D. I. Garagash et al., 2011), with a wide range of scales of time and length controlling the fluid-driven crack propagation (Detournay, 2016). Under simplified assumptions of problem geometry and physical behavior, analytical solutions (D. Garagash & Detournay, 2000; J. I. Adachi & Detournay, 2002; Savitski & Detournay, 2002; Detournay, 2016) give good predictions of multi-scale asymptotic behavior which has been confirmed by laboratory experiments in highly controlled environments (Bunger & Detournay, 2008). Numerical methods are more computationally costly but can also overcome the simplifications typical of analytical solutions (Lecampion et al., 2018), such as planar cracks and homogeneous material properties (Bunger et al., 2013). Most numerical methods are based on Linear Elastic Fracture Mechanics (LEFM) (J. Adachi et al., 2007) and the problem of hydraulic fracture propagation has been addressed either by i) assuming planar and single mode crack propagation or ii) accounting for non-planar propagating cracks that interact with pre-existing natural fractures (Weng, 2014).

The first approach assumes the crack as a planar object splitting the material in two parts with a displacement discontinuity that evolves over time: the dimensions of the hydraulic fracture (such as its length, height and aperture) change as the fluid is injected. Models of three-dimensional (3D) bi-wing planar fractures rely upon the known fracture models from Perkins, Kern and Nordgren (PKN) (Perkins & Kern, 1961), Geertsma and de Klerk (GDK) (Geertsma & De Klerk, 1969) and more generalized three-dimensional models (Nordgren, 1972). The crack propagation criterion is based on the energy-release rate (Griffith, 1921) and propagation occurs if the stress intensity factor reaches the critical value (J. Adachi et al., 2007). Viscous dissipation of fluid is an additional source of energy dissipation in hydraulic fracturing where the LEFM solution is coupled with Poiseuille's

70 flow in the fracture and Carter’s equation for leak-off from the fracture to the formation
 71 (Detournay & Cheng, 1993). The crack propagates along trajectories in a parametric space
 72 whose asymptotic regimes are characterized by a prevailing mechanism among leak-off,
 73 toughness, storage and viscosity (Detournay, 2016). Rock’s stiffness, strength and per-
 74 meability, fluid’s viscosity and injection rate control the trajectories of the parametric
 75 space. Although single mode-I planar crack models give good estimates of the fracture
 76 dimensions whenever the basic assumptions hold valid, they fall short whenever hetero-
 77 geneities cannot be neglected—a typical occurrence in geothermal reservoirs.

78 Models of fracture interaction (Warpinski & Teufel, 1987; Jeffrey et al., 1994, 2009;
 79 Renshaw & Pollard, 1995; Weng, 2014; McClure Mark et al., 2015) have to account for
 80 hydraulic fracture arrest, cross or branch at the intersection with a natural fracture (Fig-
 81 ure 1). Although Yew & Weng (2015) report the Unconventional Fracture Model (UFM)
 82 by Weng et al. (2011) as one of the first models of hydraulic fracture propagation that
 83 accounts for fluid flow and complex network of natural fractures, several problems re-
 84 garding the computational mechanics of hydraulic fracture remain unsolved. Two main
 85 approaches have so far emerged: i) the first one employs the Displacement Discontinu-
 86 ity Method (DDM), such as the Unconventional Fracture Model (UFM) or Crack Tip
 87 Open Displacement (CTOD) and ii) the second one uses Finite Elements or Finite Vol-
 88 umes Methods (FEM or FVM), where natural fractures are either smeared using an im-
 89 plicit approach (Non-local Damage or Phase-Field) or embedded into Cohesive Zone Mod-
 90 els. The DDM is computationally inexpensive, as it requires discretization of the bound-
 91 aries only, but cannot handle reservoir heterogeneities. The FEM with explicit embed-
 92 ded discontinuities faces two main drawbacks: i) it requires fine crack-tip discretization
 93 to preserve accuracy, hampering its applicability to real-case scenarios where the hydraulic
 94 fracture is expected to propagate for several hundreds of meters, and ii) it suffers from
 95 element-distortion issues that generate inaccuracies in crack opening calculations and
 96 induce numerical instabilities. The eXtended Finite Element Method (Belytschko & Black,
 97 1999; Belytschko et al., 2001; Moës et al., 1999; Yazid et al., 2009; Gupta & Duarte, 2016;
 98 Wang, 2019) overcomes the classical finite elements limitations of resolving field discon-
 99 tinuities by use of enriched shape-function, although it is computationally expensive, can
 100 hardly handle *hydraulic fracture - natural fractures* interaction and can on occasions be
 101 numerically unstable.

102 The phase-field method of fracture is a valid and promising alternative. Given its
 103 success in modeling propagation of brittle fracture, its development has been extended
 104 to ductile (Ambati et al., 2015; Miehe, Hofacker, et al., 2015; Kuhn et al., 2016; Alessi
 105 et al., 2017), fatigue (Alessi et al., 2018; Seiler et al., 2018; Carrara et al., 2019), and dy-
 106 namic fractures (Bourdin et al., 2011; Borden et al., 2012; Hofacker & Miehe, 2012; Schlüter
 107 et al., 2014; Li et al., 2016; Fischer & Marigo, 2019). The variational phase-field (V-pf)
 108 is a generalized Griffith criterion (Francfort & Marigo, 1998) numerically implemented
 109 using a phase-field variable, which smears the sharp interface fracture with a smooth tran-
 110 sition function (Bourdin et al., 2000). The phase-field variable describes the transition
 111 from intact to fully damaged state of the material over a specific length scale. Seminal
 112 works of the application of the V-pf approach to hydraulic fracture include Bourdin et
 113 al. (2012); Chukwudozie et al. (2013) while following studies addressed problems related
 114 to poro-elasticity (Wheeler et al., 2014; Mikelić et al., 2015; Miehe, Mauthe, & Teicht-
 115 meister, 2015; Wilson & Landis, 2016; Santillán et al., 2017), fracture width computa-
 116 tion (Xia et al., 2017; Lee et al., 2017), coupling with the theory or porous media (Ehlers
 117 & Luo, 2017; Heider & Markert, 2017), pressure dependent failure mechanisms (Choo
 118 & Sun, 2018), mass conservation (Chukwudozie et al., 2019), in-situ stresses (Shiozawa
 119 et al., 2019). The smeared representation can handle complex fracture topology where
 120 natural fractures can be represented within non-conforming discretizations, without a-
 121 priori assumptions on their geometry or restriction on hydraulic fracture growth trajec-
 122 tories (Yoshioka & Bourdin, 2016).

123 In this study, we solve the toughness dominated hydraulic fracturing problem with
 124 a V-pf approach formulated with the constitutive model known as no-tension or masonry
 125 model (Freddi & Royer-Carfagni, 2011; Del Piero, 1989). The main goal is to study the
 126 hydraulic fracture interaction with reservoir heterogeneities in the form of pre-existing
 127 natural fractures with efficient computational V-pf models. We apply the V-pf method
 128 to a real case study of a potential EGS system, i.e., the Acoculco geothermal field lo-
 129 cated in Puebla, Mexico. Two exploration wells were drilled within the geothermal field
 130 and, through log data analysis, a high temperature ($T \sim 300^\circ\text{C}$) and low permeable
 131 ($k = 1 \times 10^{-18} \text{ m}^2$) reservoir was identified at $\sim 2 \text{ km}$ depth. Natural fractures are
 132 modeled as complex Discrete Fracture Networks (DFN) calculated from outcrop field mea-
 133 surements and mechanical rock properties are derived from laboratory testing on sam-
 134 ples collected in the field.

135 This article is structured as follows: in section 2, we introduce the governing equa-
 136 tions of the V-pf model, their implementation in the open-source software OpenGeoSys
 137 (Kolditz et al., 2012), the experimental program and the stochastic method to build DFNs.
 138 In Section 3 we introduce applications of simple computational scenarios and geother-
 139 mal reservoir stimulation. Section 4 presents the results of the simulations and contains
 140 a wider discussion of our results as well as broader implications of our main findings. Fi-
 141 nally, we draw general conclusions of the study in section 6.

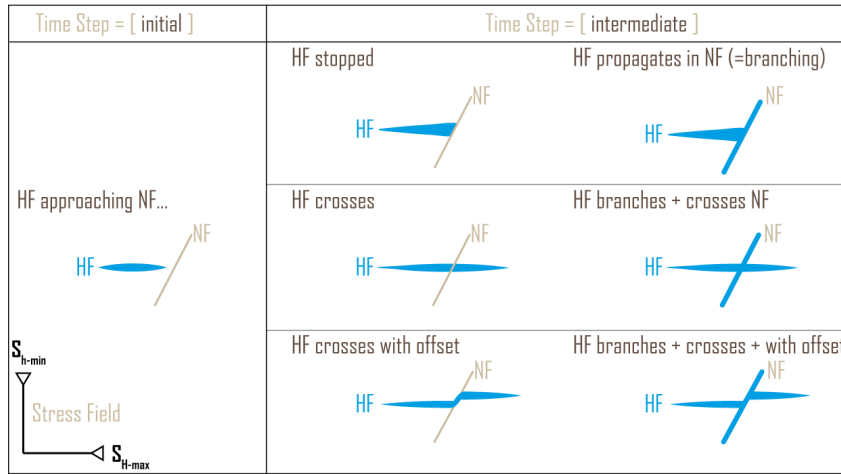


Figure 1: Possible interaction process of hydraulic fracture and natural fractures: i) Hydraulic fracture encounters a natural fracture can either arrests, cross or be deviated by the natural fracture; ii) hydraulic fracture encounters a natural fracture and propagates along its direction, which can generate branching.

142 2 Variational Phase-field Model

143 2.1 Variational approach to fracture

144 LEFM is based on Griffith’s observation that the energy dissipation by a propa-
 145 gating crack equals the mechanical energy decay (Griffith, 1921). Thus the criterion for
 146 fracture propagation is given as

$$G_c = G, \tag{1}$$

147 where G_c is the critical surface energy release rate and G is the mechanical energy resti-
 148 tution rate. The energy restitution rate is defined as the derivative of the elastic energy
 149 \mathcal{P} with respect to a crack increment length a , which is often derived using the concept
 150 of stress intensity factor Irwin (1957). Griffith criterion reads then as

$$\frac{\partial \mathcal{P}}{\partial a} = G_c, \quad (2)$$

151 which was revisited by Francfort & Marigo (1998) noticing that it can be described
 152 in terms of critical values of the following total energy along a prescribed path as

$$\mathcal{P} + G_c a. \quad (3)$$

153 The Griffith's criterion was generalized in the variational framework by consider-
 154 ing a total energy with any crack set Γ as opposed to a prescribed path a as

$$\underbrace{\mathcal{F}}_{\text{Total energy}} = \underbrace{\mathcal{P}}_{\text{Mechanical energy}} + \underbrace{\int_{\Gamma} G_c dS}_{\text{Surface energy}}, \quad (4)$$

155 such that the fracture propagation criterion is obtained by solving for the set of
 156 mechanical energy \mathcal{P} and the crack geometry Γ that minimizes Equation (4). For a pre-
 157 scribed crack path (e.g., a), the approach converges to Griffith's criterion which can be
 158 viewed as a local energy minimum problem.

159 2.2 Governing Equations

160 The linear elastic constitutive equation of a brittle-elastic porous medium occupy-
 161 ing a domain Ω can be expressed as (Biot, 1941)

$$\boldsymbol{\sigma} = \mathbf{C} : \boldsymbol{\varepsilon}(\mathbf{u}) + \alpha p_p \mathbf{I}, \quad (5)$$

162 where \mathbf{C} is the fourth order linear elastic tangent operator, α is the Biot's coeffi-
 163 cient, p_p is the pore-pressure, \mathbf{I} is the identity matrix, and $\boldsymbol{\varepsilon}$ is the linearized strain ten-
 164 sor defined as the symmetric part of the displacement gradient $\nabla \mathbf{u}$

$$\boldsymbol{\varepsilon}(\mathbf{u}) := \frac{\nabla \mathbf{u} + \nabla \mathbf{u}^t}{2}. \quad (6)$$

165 Also, consider crack set Γ filled with a fluid at pressure p_f and let $\partial\Omega_N$ be a por-
 166 tion of its boundary and $\partial\Omega_D := \partial\Omega \setminus \partial\Omega_N$ the remaining part, static equilibrium and
 167 continuity of stress at the interfaces mandates that

$$\begin{cases} \nabla \cdot \boldsymbol{\sigma}(\mathbf{u}) = \mathbf{0} & \text{in } \Omega \setminus \Gamma, \\ \boldsymbol{\sigma} \cdot \mathbf{n} = \boldsymbol{\tau} & \text{on } \partial\Omega_N, \\ \mathbf{u} = \mathbf{u}_0 & \text{on } \partial\Omega_D, \\ \boldsymbol{\sigma}^\pm \cdot \mathbf{n}_{\Gamma^\pm} = p_f \mathbf{n}_{\Gamma^\pm} & \text{on } \Gamma^\pm. \end{cases} \quad (7)$$

168 where \mathbf{f} denotes an external body force and $\boldsymbol{\tau}$ is a traction force. Multiplying (7)
 169 by a test function $\delta \mathbf{u} \in H^1(\Omega \setminus \Gamma)$ that vanishes on $\partial\Omega_D$ and using Green's theorem,
 170 we obtain

$$\int_{\Omega \setminus \Gamma} \mathbf{C} \left(\boldsymbol{\varepsilon}(\mathbf{u}) - \frac{\alpha}{N\kappa} p_p \mathbf{I} \right) \cdot \boldsymbol{\varepsilon}(\delta \mathbf{u}) \, dV = \int_{\partial \Omega_N^m} \boldsymbol{\tau} \cdot \delta \mathbf{u} \, dS + \int_{\Gamma} p_f [\delta \mathbf{u} \cdot \mathbf{n}_\Gamma] \, dS + \int_{\Omega \setminus \Gamma} \mathbf{f} \cdot \delta \mathbf{u} \, dV, \quad (8)$$

171 where $N = 2$ and $N = 3$ for 2D and 3D respectively and κ denotes the mate-
 172 rial's bulk modulus. We recall that given p_p , p_f , and Γ , Equation (9) is the unique so-
 173 lution of the minimization among all kinematically admissible displacement of

$$\mathcal{P} = \int_{\Omega \setminus \Gamma} W(\boldsymbol{\varepsilon}(\mathbf{u}), p_p) \, dV - \int_{\partial \Omega_N^m} \boldsymbol{\tau} \cdot \mathbf{u} \, dS - \int_{\Gamma} p_f [\mathbf{u} \cdot \mathbf{n}_\Gamma] \, dS - \int_{\Omega \setminus \Gamma} \mathbf{f} \cdot \mathbf{u} \, dV, \quad (9)$$

174 where

$$W(\boldsymbol{\varepsilon}(\mathbf{u}), p) := \frac{1}{2} \mathbf{C} \left(\boldsymbol{\varepsilon}(\mathbf{u}) - \frac{\alpha}{N\kappa} p_p \mathbf{I} \right) \cdot \left(\boldsymbol{\varepsilon}(\mathbf{u}) - \frac{\alpha}{N\kappa} p_p \mathbf{I} \right), \quad (10)$$

175 is the poro-elastic strain energy density (Yoshioka & Bourdin, 2016).

176 2.3 Phase-field Approximation

177 The numerical implementation of the minimization of Equation (4) involves dis-
 178 continuous deformation across unknown discontinuity surfaces (the cracks), Γ , which pose
 179 significant challenges in terms of numerical implementation. Instead, Equation (4) is reg-
 180 ularized using the phase-field approach (Bourdin et al., 2000, 2008).

181 Introducing a scalar phase-field variable, $v : \Omega \mapsto [0, 1]$, which represents a state
 182 of the material from intact material ($v = 1.0$) to fully broken ($v = 0.0$) with a con-
 183 tinuous function and a regularization parameter with the dimension of a length, $\ell_s >$
 184 0 , which controls the transition length of the phase-field variable, Equation (4) can be
 185 approximated as (Bourdin et al., 2012)

$$\mathcal{F}_{\ell_f} = \int_{\Omega} v^2 W \, dV - \int_{\partial \Omega_N^m} \boldsymbol{\tau} \cdot \mathbf{u} \, dS - \int_{\Omega} \mathbf{f} \cdot \mathbf{u} \, dV + \int_{\Omega} p_f \mathbf{u} \cdot \nabla v \, dV + \frac{1}{4c_n} \int_{\Omega} G_c \left(\frac{(1-v)^n}{\ell_s} + \ell_s |\nabla v|^2 \right) \, dV, \quad (11)$$

186 where c_n is a normalization parameter defined as $c_n := \int_0^1 (1-s)^{n/2} \, ds$. Case $n =$
 187 1 is often referred as AT_1 ($c_n = 3/2$) and case $n = 2$ as AT_2 ($c_n = 1/2$) (Tanné et al.,
 188 2018). It can then be shown (Ambrosio & Tortorelli, 1990, 1992; Braides, 1998) that as
 189 ℓ_s approaches 0, the minimizers of Equation (11) converge to that of Equation (4) in the
 190 sense that the phase-field function v takes value 1 far from the crack Γ and transitions
 191 to 0 in a region of thickness of order ℓ_s along each crack faces of Γ .

192 We can observe that in Equation (11), the evolution of the phase-field (v) is driven
 193 by the strain energy (W) regardless of the deformation direction, which leads to equal
 194 strength in tension and compression – a wrong approximation for granular material such
 195 as rock. To overcome the limitation, the strain energy can be decomposed into the pos-
 196 itive (extension) and negative (shortening) parts

$$W = W^+ + W^-. \quad (12)$$

197 Among the several approaches for the strain decomposition (Amor et al., 2009; Miehe
 198 et al., 2010; Freddi & Royer-Carfagni, 2011), we employ the so-called masonry model (Freddi
 199 & Royer-Carfagni, 2011), in which the material will not withstand tensile stresses.

200 We represent discontinuous interfaces by a diffused variable of the phase-field type
 201 (v) whose fracture toughness or cohesive strength is different from the surrounding (Fig.
 202 2). To compensate the fracture toughness in the smeared interface $x < b$, we solve the
 203 surface energy functional in Equation (11) for the effective fracture toughness, \tilde{G}_c^{int} (Hansen-
 204 Dörr et al., 2019). The surface energy equality can be imposed as

$$\tilde{G}_c^{\text{int}} \int_{\Omega} S \, dV = G_c^{\text{int}} \int_{\xi=0}^{\xi=b} S \, dV + G_c^{\text{bulk}} \int_{\xi=b}^{\infty} S \, dV, \quad (13)$$

205 where

$$S = \frac{1}{4c_n} \left(\frac{(1-v)^n}{\ell_s} + \ell_s |\nabla v|^2 \right), \quad (14)$$

206 and ξ is the distance from the crack ($v = 0$). We built the FEM model contain-
 207 ing natural fractures by assigning the equivalent fracture toughness computed in Equa-
 208 tion (13) to the region within distance b from the fractures.

209 2.4 Numerical Implementation

210 We neglect leak-off to the rock mass because the permeability of the rock mass is
 211 sufficiently low. The pore-pressure p_p can be considered invariant and set as $p_p = 0$,
 212 and $p'_f = p_f - p_p$ in the governing equations. We adopt the notation $p'_f = p$ and we
 213 assume that p is spatially constant, which implies that the pressure loss within the crack
 214 is negligible. Equation (11) is solved by the alternate minimization with respect to the
 215 displacement \mathbf{u} and the phase-field v with a constraint of prescribed time-evolving fluid
 216 volume which must be equal to the crack volume, i.e., $V_{\text{inj}} = V_{\text{crack}} = \int_{\Omega} \mathbf{u} \cdot \nabla d \, d\Omega$
 217 (Yoshioka et al., 2019). The minimisation problem can be stated as

$$(\mathbf{u}, v, p)^* = \arg \min \mathcal{F}_{\ell_f}(\mathbf{u}, d, p), \quad (15)$$

$$\begin{cases} \mathbf{u} \in H^1 \\ v \in H^1, v^t \subset v^{t+\Delta t} \end{cases}$$

218 with the constrain

$$V_{\text{inj}} = \int_{\Omega} \mathbf{u} \cdot \nabla v \, d\Omega. \quad (16)$$

219 The first variation of the energy functional with respect to \mathbf{u} is

$$\begin{aligned} \delta \mathcal{F}_{\ell_f}(\mathbf{u}, v, p; \delta \mathbf{u}) &= \frac{1}{2} \int_{\Omega} \boldsymbol{\varepsilon}(\delta \mathbf{u}) : (v^2 \mathbf{C}^+ + \mathbf{C}^-) : \boldsymbol{\varepsilon}(\mathbf{u}) \, d\Omega \\ &\quad - \int_{\partial_N \Omega} \boldsymbol{\tau} \cdot \delta \mathbf{u} \, d\Gamma - \int_{\Omega} \mathbf{f} \cdot \delta \tilde{\mathbf{u}} \, d\Omega + \int_{\Omega} p \delta \mathbf{u} \cdot \nabla v \, d\Omega, \end{aligned} \quad (17)$$

220 where \mathbf{C}^{\pm} is the tangent stiffness tensor

$$\mathbf{C}^{\pm} = \frac{\partial}{\partial \boldsymbol{\varepsilon}} \left(\frac{\partial W^{\pm}}{\partial \boldsymbol{\varepsilon}} \right). \quad (18)$$

221 The first variation of the energy functional with respect to v for AT₁ is

$$\delta\mathcal{F}_{\ell_s}(\mathbf{u}, v, p; \delta v) = \int_{\Omega} v \delta v \mathbf{C}^+ \boldsymbol{\varepsilon}(\mathbf{u}) \cdot \boldsymbol{\varepsilon}(\mathbf{u}) dV + \frac{3}{8} \int_{\Omega} G_c \left(-\frac{\delta v}{\ell_s} + 2\ell_s \nabla v \cdot \nabla \delta v \right) dV - \int_{\Omega} p \mathbf{u} \cdot \nabla \delta v dV, \quad (19)$$

and for AT₂ is

$$\delta\mathcal{F}_{\ell_s}(\mathbf{u}, v, p; \delta v) = \int_{\Omega} v \delta v \mathbf{C}^+ \boldsymbol{\varepsilon}(\mathbf{u}) \cdot \boldsymbol{\varepsilon}(\mathbf{u}) dV + \int_{\Omega} G_c \left(\frac{v-1}{\ell_s} \delta v + \ell_s \nabla v \cdot \nabla \delta v \right) dV - \int_{\Omega} p \mathbf{u} \cdot \nabla \delta v dV. \quad (20)$$

222 Equation (7) is linear to p and if we let the displacement solution with $p = 1.0$
 223 be equal to \mathbf{u}_1 , the displacement solution $p = p$ is obtained as $\mathbf{u} = p\mathbf{u}_1$ and the crack
 224 volume is

$$\int_{\Omega} \mathbf{u} \cdot \nabla v d\Omega = p \int_{\Omega} \mathbf{u}_1 \cdot \nabla v d\Omega. \quad (21)$$

225 At a given time step, a volume V_{inj} is injected and equation (16) yields the mass
 226 balance in the porous medium such that the corresponding p is

$$p = \frac{V_{\text{inj}}}{V_p}, \quad (22)$$

227 where

$$V_p = \int_{\Omega} \mathbf{u}_1 \cdot \nabla v d\Omega, \quad (23)$$

228 and the whole solution procedure is described in Algorithm 1.

229 Parallel simulations were run on the high-performance computing system JUWELS,
 230 maintained at the Jülich Supercomputing Centre. The total number of degree of free-
 231 dom for the Aocolco case scenarios is 513 108 with 170 996 linear quadrilateral elements
 232 with a few triangular elements in the mesh resolution transition zone. Domain-decomposition
 233 was done using METIS (Karypis & Kumar, 1998) and both linear and non-linear solvers
 234 from PETSc Balay et al. (2019) were used. More specifically, the Newton–Raphson solver
 235 for the deformation problem and a Newton based variational inequality solver for the
 236 phase-field, since the phase-field solution is bounded in $[0, 1]$ domain and constrained by
 237 the irreversibility. The simulations were distributed into 384 cores over 8 nodes (Dual
 238 Intel Xeon Platinum 8168) with 2×24 cores. While the computation time differs depend-
 239 ing on the non-linearity of each problem, all the simulations shown in the subsequent sec-
 240 tion were completed within ~ 20 h.

Algorithm 1 Incorporation of the volume constraint in the phase-field model.

```

1: repeat
2:   Update the injected volume,  $V_{inj}(t_n + \Delta t)$ 
3:   repeat
4:     Solve for  $\mathbf{u}_1^i$ , given  $v^{i-1}$  and  $p = 1.0$ 
5:     Solve for  $v^i$ , given  $\mathbf{u}^i$  and  $p = p^{i-1}$ 
6:     Calculate  $V_p^i$  from  $\int_{\Omega} \mathbf{u}^i \cdot \nabla v^i \, d\Omega$ 
7:     Update pressure,  $p^i = V_{inj}/V_p^i$ 
8:   until  $\|v^i - v^{i-1}\| < 10^{-4}$ 
9: until  $V < V_{final}$ 

```

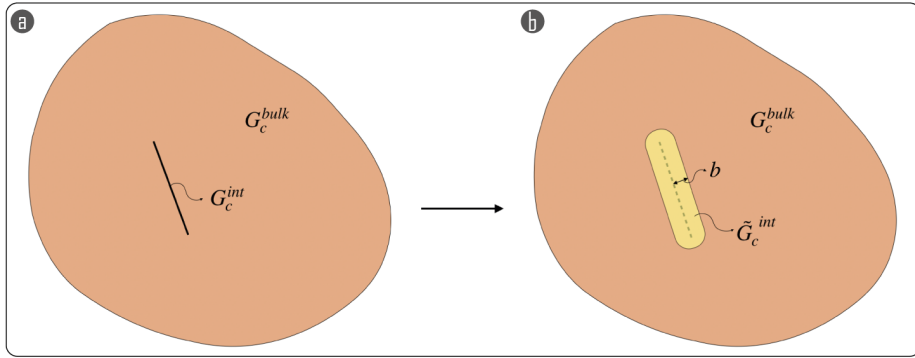


Figure 2: Diffused representation of a discontinuous interface

3 Applications

3.1 Sensitivity Analyses

We perform a sensitivity analysis to highlight the complex interactions between fluid-driven propagating fractures and existing ones. We analyze simplified models assuming a perfectly homogeneous brittle linear elastic material containing one or two pre-existing natural fractures. We evaluate the impact on fracture initiation and propagation given by stiffness (elastic parameters) and strength (fracture toughness) of the bulk rock, existing fractures, state of stress and orientation angle of the natural fractures. The base case parameters of the sensitivity analysis are in the range of the studied rocks of the Acoculco reservoir, i.e., $G_c = 100 \text{ Pa m}$, $E = 25 \text{ GPa}$ and $\nu = 0.2$.

As implemented in the V-pf, the interaction with the pre-existing natural fractures is partly controlled by the critical energy release rate of the natural fracture \tilde{G}_c^{int} . We compare results for $G_c = 1$ with different values of \tilde{G}_c^{int} spanning four orders of magnitude, i.e., $\tilde{G}_c^{\text{int}} = 0.01, 0.05, 0.1, 10$. We analyze the impact of the far-field deviatoric stress by increasing the S_{Hmax} from 21 MPa to 60 MPa with a fixed $S_{Hmin} = 20 \text{ MPa}$. All case scenarios are presented in Table 1. We finally analyze the influence of a natural fracture oriented 45° from the direction of hydraulic fracture propagation to study the effect of the incidence angle between the direction of propagation and the orientation of a natural fracture.

Table 1: Case scenarios of the sensitivity analysis with different stress fields applied. Stress values are expressed in MPa.

Case	S_{Hmax}	S_{hmin}
A	21	20
B	30	20
C	40	20
D	60	20

3.2 The Acoculco Geothermal Reservoir

In this manuscript, we analyze the potential permeability enhancement in a fractured reservoir by modeling the fracture growth from a well-bore injection. We apply the developed numerical methodology described in section 2 on the Acoculco case scenario, considering the local geological features and the rock properties gathered from field campaigns and laboratory measurements. Here we report a brief synthesis of the experimental program, field campaign, DFN construction algorithm and results, while further details can be found in the original works (Lepillier et al., 2020, 2019).

The Acoculco geothermal field, located in Mexico, hosts two vertical exploration wells (named EAC1 and EAC2) drilled at ~ 500 m apart horizontally, both reaching a total depth of ~ 2 km (López-Hernández et al., 2009; Canet et al., 2015; Weydt et al., 2018). On the one hand, Acoculco is considered a tight reservoir because the rock formations are little permeable (10^{-18} m²) and the fractures are scarcely connected (Lepillier et al., 2020); on the other hand, it is a suitable candidate for EGS development because of its high geothermal energy potential given that the geothermal gradient is above average (~ 150 °C km⁻¹). The stratigraphy encountered during drilling is simplified into three lithological units: Limestones, Marbles, Skarns. Stiffness (E and ν), strength and critical energy release rate (G_c) of the three lithologies were measured in the rock physics laboratory. Young's modulus and Poisson's ratio were determined by Unconfined Compression Strength (UCS) tests (UCS - 20 experiments). Brazilian disc (BD - 80 experiments) and Chevron Bend tests (CB - 12 experiments) were employed to determine the fracture toughness K_{Ic} of the rock formations, which was later employed to derive the critical energy release rate (G_c). Fracture toughness was determined from the two sets of experiments: i) from BD tests, it was done following the method proposed by Guo et al. (1993) and ii) for CB tests, following the method suggested by Franklin et al. (1988). All material parameters employed in the model are summarized in Table 2.

Table 2: Rock mechanical properties from rock physics laboratory measurements. This table summarizes the main results of the laboratory measurements for the concerned lithologies: Limestones, Marbles and Skarns. For each of them the table gives: the Young’s modulus (E), the Poisson’s ratio (ν), the fracture toughness (K_{Ic}), and Griffith’s critical energy release rate (G_c). A single final value for specific lithology was selected as the average between different locations outcrops.

Lithology	E GPa	ν -	K_{Ic} MPa m ^{1/2}	G_c Pa m
Limestone Late Cretaceous	37.8	0.31	2.76	201
Limestone Early Cretaceous	37.9	0.23	2.49	164
Limestone	37.9	0.27	2.63	182
Marble from Pueblo Nuevo	46.8	0.25	1.90	77.3
Marble from Tatatila	51.6	0.29	1.85	66.2
Marble	49.2	0.27	1.87	71.4
Exo-skarn from Eldorado	56.9	0.11	2.70	127
Endo-skarn from Boquillas	41.1	0.13	1.92	89.3
Skarn	49.0	0.13	2.31	108

286 The general DFN is derived from scanline measurements from multiple outcrops
287 analogues of the Acochulco geothermal system (Lepillier et al., 2020) that are later ex-
288 trapolated using the multiple point statistic method (Bruna et al., 2019). The method
289 yields three separate DFNs, i.e., one per lithology. Each one of the three DFNs is a bi-
290 dimensional geo-referenced section of $600 \times 600 \text{ m}^2$ (fig. 3). Some further processing is
291 necessary to build the FEM models. In the first step, we extracted from each DFN a smaller
292 sub-domain of $100 \times 100 \text{ m}^2$ (Figure 3). Each extraction has a specific fracture distri-
293 bution: to analyze the impact of stimulating one or another specific section of the do-
294 main. In the second step we extracted an additional three sub-domain from each of the
295 DFNs. The three sub-DFNs, one for each DFN, are then rotated in the third step to align
296 the maximum horizontal stress S_{Hmax} with the x -axis and further down-scaled in the
297 fourth step to fit the a-dimensional V-pf formulation.

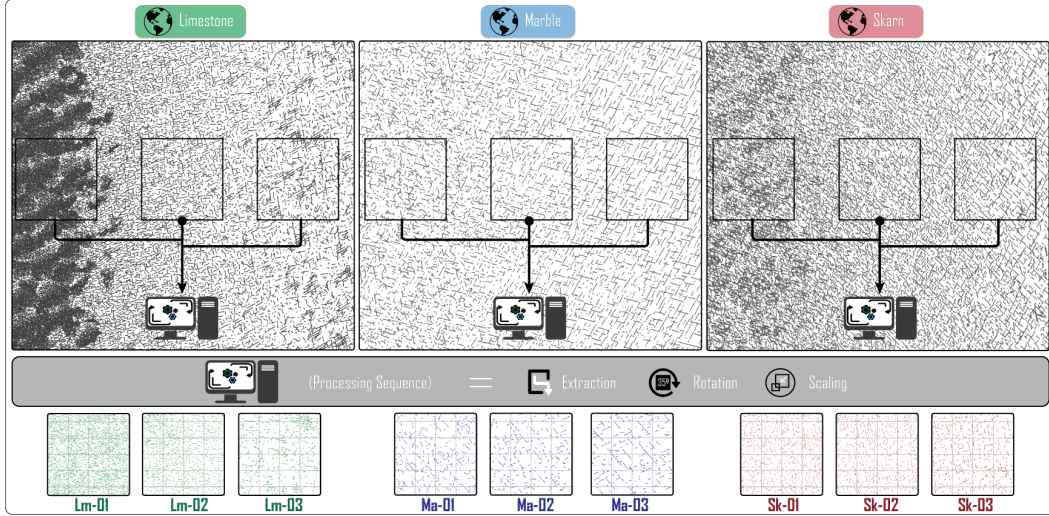


Figure 3: This figure presents the pre-processing sequence: from original reservoir scale DFN, to extracted, rotated and scaled models to fit the numerical analyzes requirements. From left to right, the DFN for the Limestone formation, the DFN for the Marble formation and the DFN for the Skarn formation. Symbols Lm/Ma/Sk-01,-02,-03 are referred to the sub-DFN extracted from initial DFN.

298 The in-situ stress state is believed to be of the normal faulting type and the orientation of the stress tensor is taken from the World Stress Map (Lepillier et al., 2019; Heidbach et al., 2016). Based on this assumption, having $sv > sh_{max} > sh_{min}$, we defined certain values for $S_{H_{max}}$ and $S_{h_{min}}$. In normal-faulting regime, the hydraulic fracture propagates along the vertical plane oriented perpendicular to $S_{h_{min}}$. Because of this, we assume 2-dimensional plane-strain conditions were we assign only $S_{H_{max}}$ and $S_{h_{min}}$.

305 4 Results

306 4.1 Sensitivity Analysis

307 Figure 4 shows the influence of strength (G_c) and stiffness (E and ν) on the internal fracture over-pressure and length evolution during hydraulic fracture propagation at constant fluid injection-rate. The critical energy release rate G_c is the dominant parameter controlling the hydraulic fracture response (fig. 4a): G_c represents the resistance to fracture propagation, hence is proportional to the maximum overpressure reached and inversely proportional to the rate of crack length growth during injection. The stiffness parameters play a smaller role on the problem evolution, and, whilst the influence of Poisson's ratio seems to be negligible over the selected range (Figure 4c), an increase in Young's modulus entails an increase in fracture propagation resistance (fig. 4b). Maximum overpressure is proportional to Young's modulus and inversely proportional to the injected volume at propagation onset.

318 The delay in crack propagation onset is a consequence of lower stiffness: the more the rock is compliant, the larger the volume of fluid needs to be injected before the crack internal pressure reaches the propagation condition and the energy release rate equals its critical value. Globally, it can be interpreted as a higher system compressibility, where more compliant systems require higher volume of injected fluids.

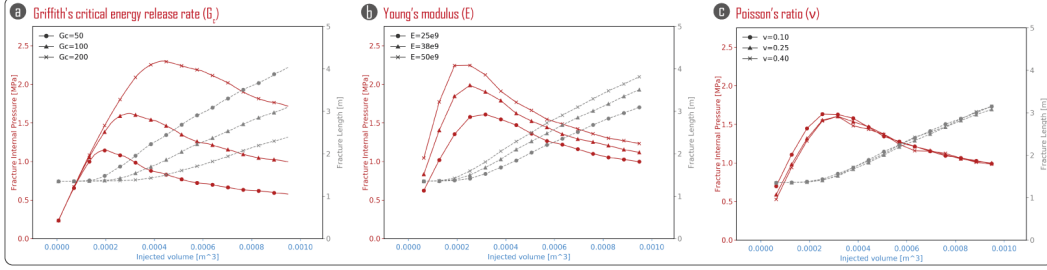


Figure 4: Sensitivity analysis of mechanical material properties. The plots report the evolution of fracture internal over-pressure (reds) and fracture length (greys) against the injected volume: in (a) for different values of the critical energy release rate of the bulk solid $G_c = 50, 100, 200 \text{ Pa m}^{-1}$; in (b) for different elastic parameters of Young's modulus with $E = 25, 38, 50 \text{ GPa}$; and (c) different Poisson's ratio $\nu = 0.10, 0.25, 0.40$.

323 Figure 5 shows results of the sensitivity analysis of the interaction between a fluid-
 324 driven fracture (the phase-field) and two natural fractures at equivalent time steps. When
 325 the contrast between bulk rock and natural fractures in terms of G_c is high, i.e., for rel-
 326 atively low \tilde{G}_c^{int} , the fracture propagates within the bulk rock before interacting with
 327 the natural fractures (fig. 5) as for $\tilde{G}_c^{\text{int}} = 0.01$ and $\tilde{G}_c^{\text{int}} = 0.05$. Once it propagates
 328 within the vertical natural fractures, it then turns into two sub-vertical wing-type cracks.
 329 For $\tilde{G}_c^{\text{int}} = 0.1$, the natural fractures do not have low enough strength and are crossed
 330 by the hydraulic fracture without branching (fig. 5). For $\tilde{G}_c^{\text{int}} > G_c$, the natural fracture
 331 act as a barrier to the hydraulic fracture. After the crack hits the natural fracture,
 332 it propagates in a path avoiding the natural fracture. In this case, the natural fracture
 333 acts as a barrier, shielding the hydraulic fracture propagation. Note that branching in
 334 general is energetically more expensive (less favored) but does happen when the surface
 335 energy of the natural fractures are so low that crack propagation along them becomes
 336 more attractive.

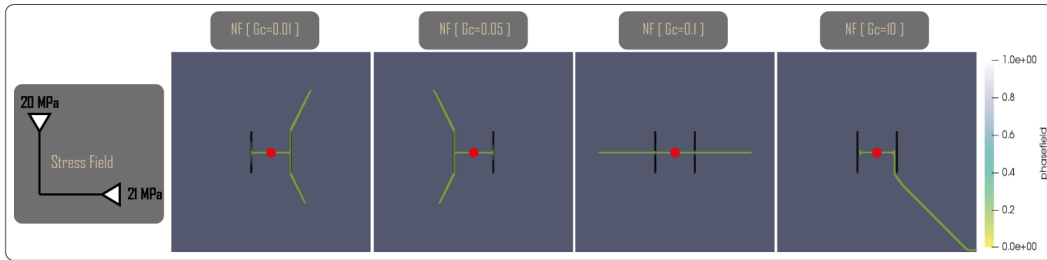


Figure 5: Sensitivity analysis of the influence of two vertical natural fractures. The results show the phase-field distribution contour map in the domain at the same time step for a constant stress field and different critical energy release rate of the natural fracture \tilde{G}_c^{int} . The stress field is oriented such that S_{Hmax} is aligned along the horizontal direction. The red dots represent the well-bore and initial fracture position (and initial phase-field implementation)

337 At increasing values of differential stress (fig. 6), and for fixed $\tilde{G}_c^{\text{int}} = 0.01$, the
 338 branching observed at low deviatoric stress disappears for $S_{Hmax} \geq 30 \text{ MPa}$. The critical
 339 stress intensity factor at the tip of the natural fracture is proportional to the hor-

340 horizontal stress and propagating a fracture parallel to S_{Hmax} through the bulk rock requires
 341 less energy than propagating it through the vertical natural fracture. Therefore, with
 342 higher deviatoric stress, considering a natural fracture oriented 90° will not change the
 343 propagation direction as the stress dictates the propagation direction.

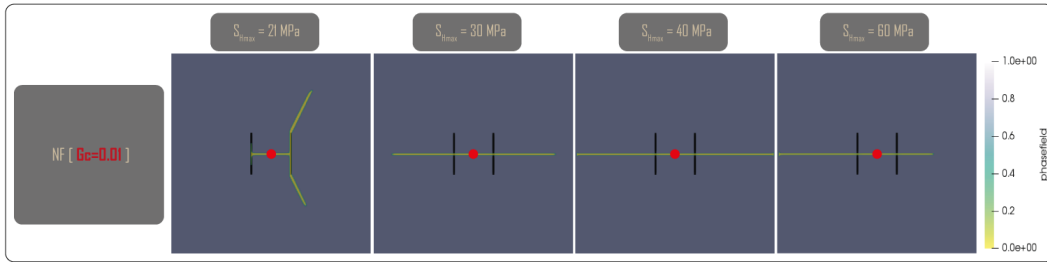


Figure 6: Sensitivity analysis of the influence of two vertical natural fractures. The results show the phase-field distribution contour map in the domain at the same time step for a constant critical energy release rate of the natural fracture \tilde{G}_c^{int} and different stress field values $\tilde{G}_c^{\text{int}} = 0.01$. The stress field is oriented such that S_{Hmax} is aligned along the horizontal direction. The red dots represents the well-bore and initial fracture position (and initial phase-field implementation)

344 A 45° -oriented fracture has an orientation which is closer to the critical one for the
 345 given state of stress, hence it influences the propagation and interaction regime differ-
 346 ently than vertical natural fracture (fig. 7). With only one natural fracture present, the
 347 problem is intrinsically asymmetric. At $\tilde{G}_c^{\text{int}} = 0.01$, the hydraulic fracture first inter-
 348 acts with the natural fracture and later propagates in the direction of S_{Hmax} (fig. 7a)
 349 and at $\tilde{G}_c^{\text{int}} = 0.1$, the hydraulic fracture propagation is still attracted by the inclined
 350 natural fracture but not as much as the case with $\tilde{G}_c^{\text{int}} = 0.1$. For high values of the
 351 natural fractures' critical energy release rate, i.e., for $\tilde{G}_c^{\text{int}} = 10$, even though the nat-
 352 ural fracture is more favorably oriented, it becomes once again a barrier to fracture prop-
 353 agation (fig. 7a). For $\tilde{G}_c^{\text{int}} = 0.01$ with varying horizontal stresses S_{Hmax} , the hydraulic
 354 fracture propagation along the natural fracture is progressively hindered with increas-
 355 ing S_{Hmax} (fig. 7b). At $S_{Hmax} = 40$ MPa, the hydraulic fracture shows a small offset
 356 at the natural fracture's crossing point while the hydraulic fracture becomes agnostic to
 357 the natural fracture with $S_{Hmax} = 60$ MPa.

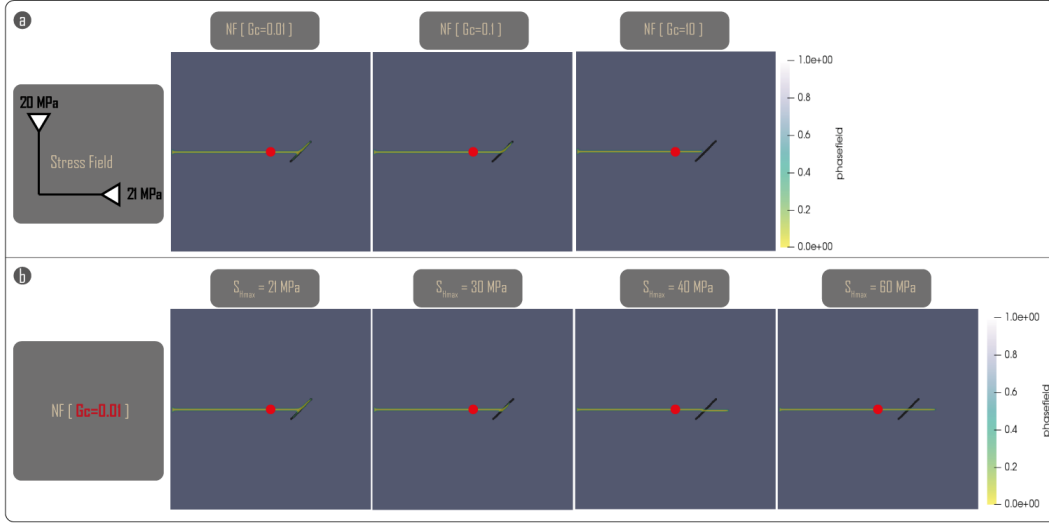


Figure 7: Sensitivity analysis of the influence of one natural fracture inclined at 45° from the horizontal axis. The results show: (a) the phase-field distribution contour map in the domain at the same time step for a constant stress field and different critical energy release rate of the natural fracture \tilde{G}_c^{int} ; and in (b) for different values of the stress field and a constant critical energy release rate of the natural fracture $\tilde{G}_c^{\text{int}} = 0.01$ (b). The stress field is oriented such that S_{Hmax} is aligned along the horizontal direction. The red dots represents the well-bore and initial fracture position (and initial phase-field implementation)

358

4.2 Stimulation of the Acoculco Geothermal Reservoir

359

360

361

362

363

364

365

366

367

368

369

370

371

372

373

374

Figures 8, 9 and 10 show the results of the stimulation scenarios in the Acoculco geothermal reservoir for the different lithologies and for different DFNs. On the left of all figures is plotted the fracture pressure and length with injected volume, while on the right is shown the contour map of the phase-field along with the distribution of natural fractures. For all the cases, the propagation pressure decreases with injected volume as the crack length increases. The pressures started declining rapidly from the onset of the injection/stimulation. This is because the simulations were initiated with a borehole without setting a priori (initial) fracture lengths, as often done in practice, which led to the high breakdown pressures. Such high pressure responses may not be observed in fields because: 1) the borehole intersects with pre-existing fractures or defects or 2) the borehole is completed with perforations or well production packers. However, if fracture is initiated in a intact rock, this level of high pressure should be expected. The fracture length increment with time shows a burst-like behavior: whenever the hydraulic fracture interacts with a natural fracture, the pressure drops as a consequence of the increase in available fluid storage capacity given by the crack sudden propagation over a finite distance within the natural fracture.

375

376

377

378

Considering all lithologies, the final fracture length ranges between ~ 75 m to ~ 95 m and a the lowest propagation pressure is observed for the Marble stimulation cases (fig. 9), whilst the highest propagation pressure is observed for the stimulation into the Limestone formation (fig. 8)—a result in agreement with the sensitivity analysis.

379

380

381

Figure 11 shows a polar representation of the hydraulic fracture deviation from the x direction during propagation. The Limestone simulations show the larger range of fracture lengths spanning from ~ 75 m to ~ 95 m while the Marble's one have the small-

382 est range, spanning from ~ 78 m to ~ 79 m. The angular deviation ranges in an inter-
 383 val of 20° above and below the reference axis given by S_{Hmax} direction. Maximum devi-
 384 ations are observed in Marble and Skarn simulations, reaching 30° in both simulations,
 385 while the deviation angle for the Limestone simulations is contained in a 20° interval.

386 The asymmetrical propagation of hydraulic fracture from the borehole is a conse-
 387 quence of the intersection angle between natural fracture and the approaching hydraulic
 388 fracture. Assuming θ as the angle between a natural fracture and the S_{Hmax} axis, we
 389 observed that: i) low- θ natural fracture act as pathways for the hydraulic fracture, which
 390 propagates faster along natural fractures; ii) high- θ natural fracture ($\sim 90^\circ$) are by-passed
 391 by the hydraulic fracture and no interaction takes place. Intermediate values of θ offer
 392 a pathway for hydraulic fracture to propagate along a certain distance, until the pres-
 393 sure build-up is sufficiently high to allow further propagation within in the matrix.

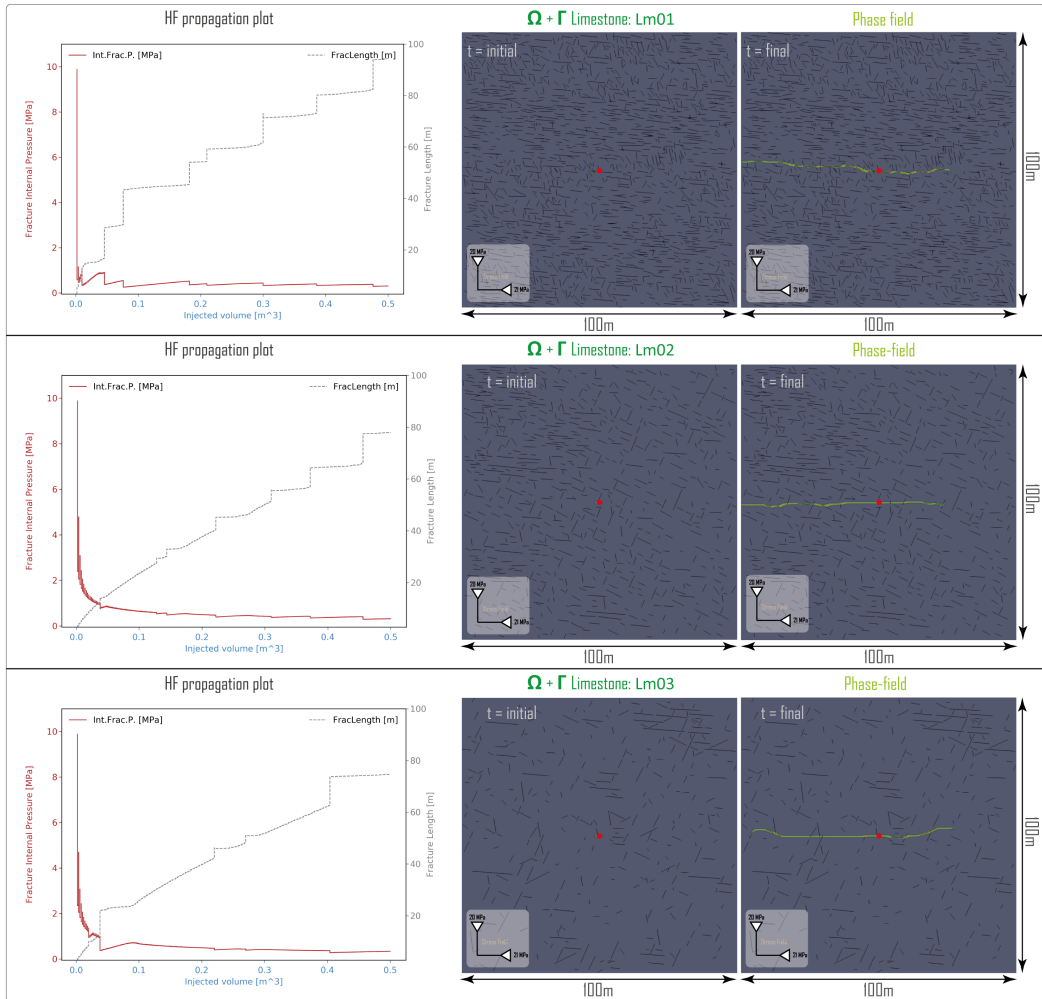


Figure 8: Hydraulic fracture models using V-pf with the sub-DFN of the Limestone reservoir. The matrix material domain Ω is represented in grey, the natural fracture Γ are discretized in black. Lm01 is composed with 1483 natural fractures, Lm02 is composed with 709 natural fractures, Lm03 is composed with 327 natural fractures. The stress field is oriented such that S_{Hmax} is aligned along the horizontal direction. The red dots represent the well-bore and initial fracture position (and initial phase-field implementation)

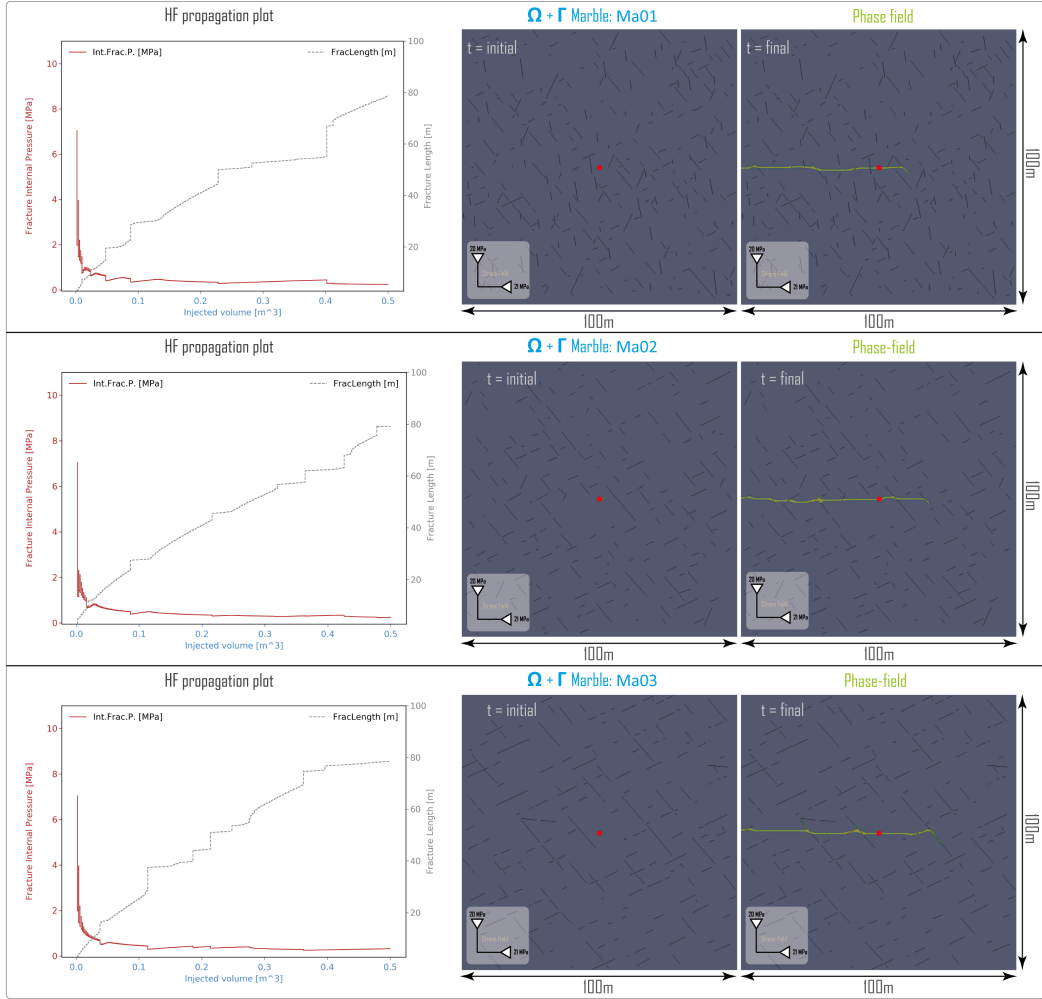


Figure 9: Hydraulic fracture models using V-pf with the sub-DFN of the Marble reservoir. The matrix material domain Ω is represented in grey, the natural fractures Γ are discretized in black. Ma01 is composed with 295 natural fractures, Ma02 is composed with 215 natural fractures, Ma03 is composed with 198 natural fractures. The stress field is oriented such that S_{Hmax} is aligned along the horizontal direction. The red dots represent the well-bore and initial fracture position (and initial phase-field implementation)

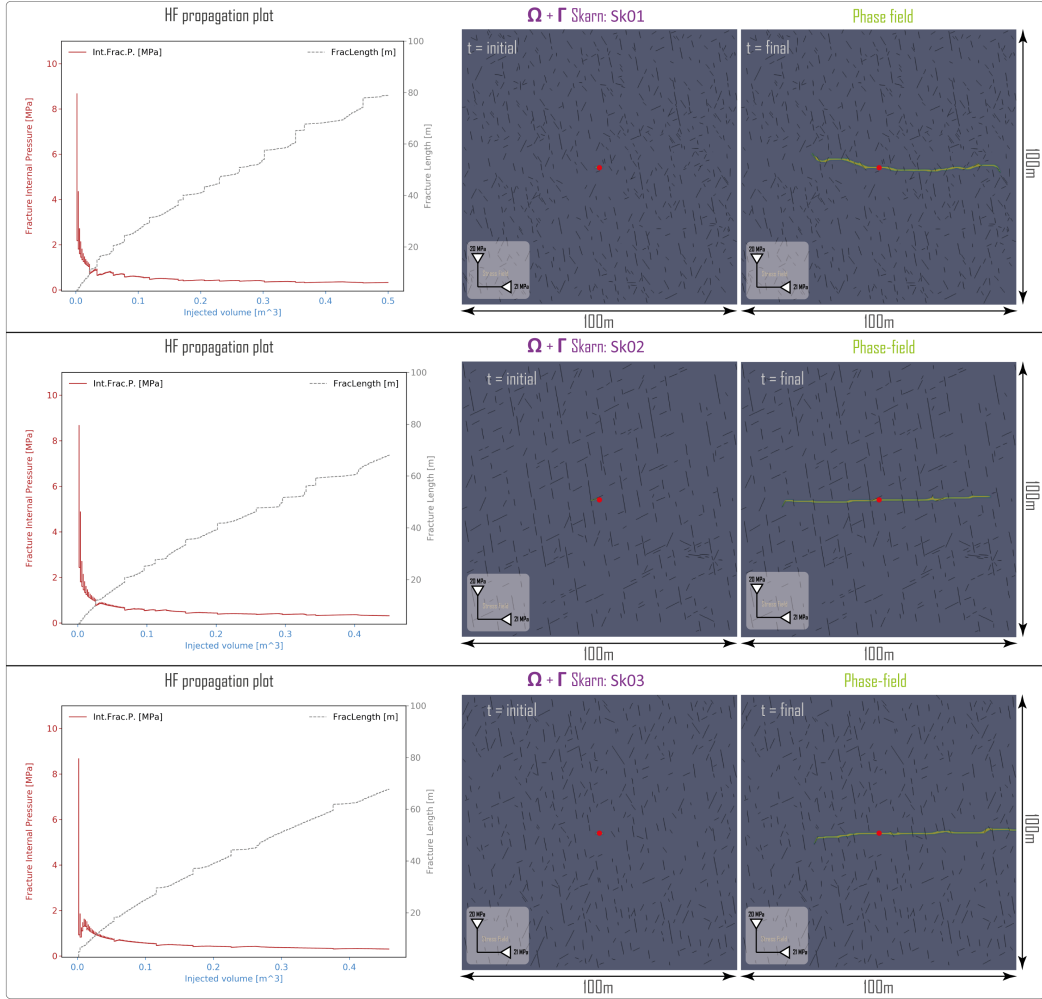


Figure 10: Hydraulic fracture models using V-pf with the sub-DFN of the Skarn reservoir. The martix material domain Ω is represented in grey, the natural fractures Γ are discretized in black. Sk01 is composed with 706 natural fractures, Sk02 is composed with 495 natural fractures, Sk03 is composed with 375 natural fractures. The stress field is oriented such that S_{Hmax} is aligned along the horizontal direction. The red dots represent the well-bore and initial fracture position (and initial phase-field implementation)

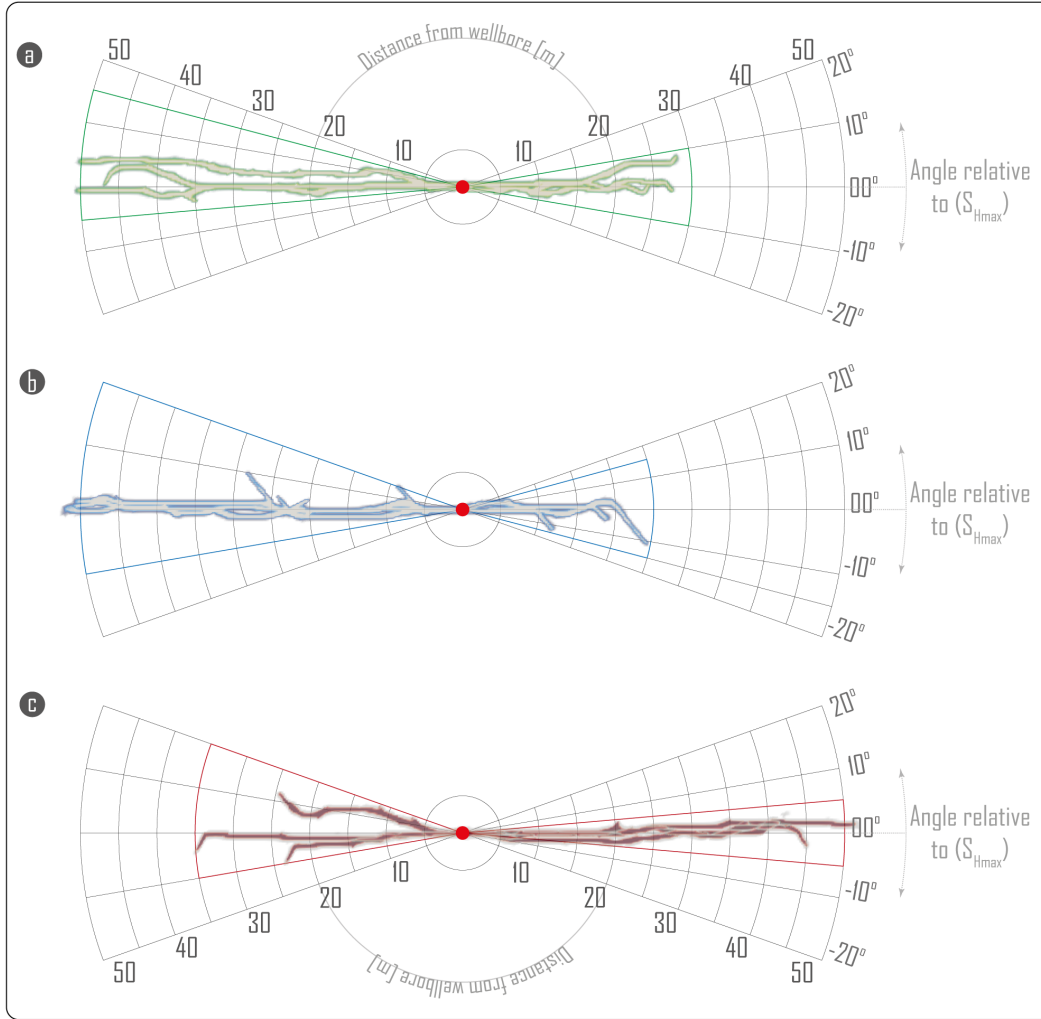


Figure 11: A comparison of hydraulic fracture simulation V-pf models for : a) the Limestones (green color); b) the Marbles (blue color); c) the Skarns (red color); hydraulic fracture lengths are given by the concentric dividers, and hydraulic fracture angles compared to S_{Hmax} 's orientation is given by the radial dividers.

394

5 Discussion

395

396

397

398

399

400

401

402

403

404

405

406

407

The V-pf method presented here is an implicit smeared approach which represents the fracture with a smoothly transitioning function that spans from intact to fully damaged state of the material. Natural fractures are represented in a non-conforming mesh with the reduced fracture toughness by enforcing energetic equivalence, which is one of the advantages of the method since it allows exploring multiple DFNs scenarios with a single discretization. As presented in this study, the ability of the V-pf is to handle complex fracture topologies with a unified criteria – energy minimization – that seeks for an admissible displacement and a set of fracture geometry that minimizes the total energy without a need for ad-hoc criteria for branching or turning. The model exhibits asymmetric crack growth under some circumstances: the phenomenon is intrinsic to the variational approach, where the energy minimization leads to the occurrence of asymmetric solutions whenever the total energy of the system is smaller than its symmetric counterpart (Gao & Rice, 1987; Bungler et al., 2008; Tanne, 2017).

408 The interaction behavior between hydraulic fracture and natural fractures depends:
 409 i) on the combination of the critically energy release rate ratio between natural fractures
 410 and bulk rock ($\tilde{G}_c^{\text{int}}/G_c$); ii) on the natural fractures orientation relative to the stress
 411 field; and iii) on the magnitude of principal stress components. Natural fractures can ei-
 412 ther favor or hamper the propagation of a hydro-fracture according to specific combi-
 413 nations of the input parameters. Natural fractures attract hydraulic fractures for rela-
 414 tively low values of critical energy release rate ratio, when they have orientations close
 415 to the critical ones and for relatively isotropic stress states. Natural fractures can be an
 416 obstacle to hydraulic fracture growth whenever the fracture resistance becomes higher
 417 than the one of the intact rock. Although counter-intuitive, the presence of higher strength
 418 discontinuities is a relatively frequent occurrence in deep geothermal systems: the en-
 419 vironmental conditions could enhance geochemical reactions of dissolution and precipi-
 420 tation (Singurindy & Berkowitz, 2005; Watanabe et al., 2020), such as silica precipita-
 421 tion (Scott & Driesner, 2018; Lu et al., 2018), and the existence of active volcanism could
 422 favor the presence of magmatic intrusions even at shallow depth (Elders et al., 2014) which,
 423 if old and cold enough, could represent higher strength and stiffness bodies.

424 In our analyzes, we have assumed a low permeability that is typical of poorly frac-
 425 tured crystalline rock, an hypothesis that entails no leak-off between the fracture and
 426 the porous rock. Such an assumption is equivalent to an undrained response where the
 427 change in effective stress within the porous rock is null during injection. Although the
 428 fracture toughness (critical energy release rate) is more predominant in controlling prop-
 429 agation conditions when compared to stiffness, Young’s modulus of the rock also plays
 430 a role. In particular, a more compliant rock requires higher injected volumes, but over-
 431 all generates lower over-pressure. On the contrary, stiff rocks generate higher over-pressure
 432 for a lower injected volume. Because of the high fracture strength, high stiffness and low
 433 permeability of basement crystalline rocks, during stimulation of a deep geothermal reser-
 434 voir high over-pressure can be achieved with relatively low values of injected volume (Ellsworth
 435 et al., 2019).

436 The V-pf simulations of the Acoculco reservoir highlighted a fluctuation in the pres-
 437 sure and crack-length response in time, with intermittent crack advancement and burst-
 438 like behavior—a phenomenon observed during several hydraulic stimulations (Milanese
 439 et al., 2016). The V-pf implementation adopted is numerically stable and provides con-
 440 tinuous pressure-volume response in absence of viscous flow dissipation. The intermit-
 441 tent advancements are a direct consequence of the interaction between existing fractures
 442 with lower crack resistance and the fluid driven crack: whenever the hydraulic fracture
 443 encounters a natural fracture, if the latter is favorably oriented, the hydraulic fracture
 444 encounters almost no resistance and propagates rapidly over a finite length. The pres-
 445 sure drop is associated with a stress release in the rock, which in combination with the
 446 crack length increment, can be associated with micro-earthquakes. Micro-seismicity has
 447 been widely observed during hydraulic fracturing (Davies et al., 2013; Schultz et al., 2015;
 448 Lopez-Comino et al., 2017) and our results suggest that, in crystalline reservoirs, the phe-
 449 nomenon is associated with hydraulic fractures propagating along pre-existing natural
 450 fractures.

451 Results show that the Marble formation in the Acoculco reservoir is the optimal
 452 one for a potential stimulation because the lowest values of propagation over-pressure.
 453 The orientation of the natural fractures controls the propagation extent and direction
 454 independently of the lithology and the fracture topology dominates the hydraulic frac-
 455 ture response in all cases analyzed. In the present case study we have analyzed homo-
 456 geneous rock matrix properties, although a more realistic approach should be based on
 457 representing fluctuation of the material properties within the rock matrix. Three-dimensional
 458 analyzes would be an additional improvement of the current scenarios. Nonetheless, the
 459 additional complexity of a three-dimensional reservoir model should be justified by a suf-
 460 ficient knowledge of the reservoir’s structure and its property—a current shortcoming for

461 the Acoculco reservoir. Although a normal fault regime is likely at Acoculco reservoir
462 and hydraulic fractures are expected to propagate mainly vertically, there are indications
463 that a strike-slip faulting system could also be active (Liotta et al., 2020), making the
464 full three-dimensional propagation topology rather complex and difficult to estimate a-
465 priori.

466 There is current uncertainty about the in-situ state of stress at the Acoculco geother-
467 mal reservoir and different values of the stress components could yield a different out-
468 put in terms of hydraulic fracture propagation. Although the DFNs that are built from
469 outcrop extrapolations are also a source of additional uncertainty, the small prominence
470 of fractures in the DFNs seems to be in good agreement with the very low permeabil-
471 ity that was observed during well logging: small and poorly connected fractures ham-
472 per fluid flow in the tight reservoir.

473 Stimulating a highly fractured zone of the Acoculco geothermal reservoir requires
474 a lower stimulation pressure, therefore reducing the drilling costs. Additionally, accord-
475 ing to the well temperature measurements, the Marble and Skarn formations are more
476 likely to be targeted for stimulation because they are present at a higher depth and there-
477 fore, they are at a higher temperature. The formation breakdown pressure is lower for
478 the Marble, which also has a lower density of natural fractures. Nonetheless, the nat-
479 ural fractures in the Marble are longer and better connected when compared to the ones
480 in the Skarn, which are shorter but more frequent. A trade-off arises between the ob-
481 jective of stimulating the hotter formations of the reservoir on the one hand, and stim-
482 ulating the formations that would yield a longer propagation of the hydraulic fracture
483 on the other hand. The optimal solution would depend on the ultimate goals of the EGS
484 development and a detailed cost-balance analysis is necessary to optimize the stimula-
485 tion depth.

486 6 Conclusions

487 We have presented a method for modeling hydraulic fracture propagation and in-
488 teraction with a network of natural fractures in a geothermal reservoir. The fracture sim-
489 ulations are based on a variational phase-field approach that proved high numerical sta-
490 bility. We have highlighted the main factors controlling the hydraulic fracture propaga-
491 tion and its interaction with natural fractures through sensitivity analyzes on simplified
492 models. We have applied the method to model a realistic EGS stimulation scenario of
493 the geothermal reservoir of Acoculco, Mexico. The numerical model is built from field
494 data and model parameters are derived from laboratory experiments.

495 Building a realistic DFN is an essential piece of the puzzle for numerical analyzes
496 of stimulation of complex reservoirs, which can lead to counter-intuitive findings of the
497 propagation mechanisms as opposed to simplified models of single-oriented crack fam-
498 ilies. Pressure fluctuations and burst-like crack propagation are intrinsically connected
499 to the presence of the complex network of natural fractures.

500 The numerical model is implemented in the open-source software OpenGeoSys ([www](http://www.opengeosys.org)
501 [.opengeosys.org](http://www.opengeosys.org)), which can be freely downloaded at <https://github.com/ufz/ogs>.
502 We provide a working methodology for the study of EGS systems and the feasibility an-
503 alyzes of hydraulic stimulation of geothermal reservoirs.

504 Acknowledgments

505 This work is part of the GEMex consortium, a European-Mexican collaboration, which
506 aims at investigating non-conventional geothermal systems: i) an enhanced geothermal
507 system, as studied in the case of Acoculco site; ii) and a supercritical system, as stud-
508 ied in the geothermal field of Los Humeros. We would like to thank all the GEMex team,
509 and especially our Mexican partners who guided us in the field. GEMex has received fund-

510 ing from the European Unions Horizon 2020 research and innovation programme under
 511 grant agreement No. 727550 and the Mexican Energy Sustainability Fund CONACYT-
 512 SENER, project 2015-04-268074. More information is available on: www.gemex-h2020.eu.

513 K.Y. gratefully acknowledges the funding provided by the German Federal Min-
 514 istry of Education and Research (BMBF) for the GeomInt project, Grant Number 03G0866A,
 515 within the BMBF Geoscientific Research Program "Geo:N Geosciences for Sustainabil-
 516 ity". The contribution of F.P. was funded by the Deutsche Forschungsgemeinschaft (DFG,
 517 German Research Foundation) project number PA 3451/1-1.

518 Laboratory works who not have been possible without help and support from the
 519 laboratory staff. B.L., R.B. and D.B. give thanks to the Delft University of Technology
 520 GSE laboratory staff.

521 The authors gratefully acknowledge the Earth System Modeling Project (ESM) for
 522 funding this work by providing computing time on the ESM partition of the supercom-
 523 puter JUWELS at the Jlich Supercomputing Centre (JSC)

524 The datasets generated during and/or analyzed during the current study are avail-
 525 able in the repository:

526 <https://doi.org/10.6084/m9.figshare.12033624.v2>

527 References

- 528 Adachi, J., Siebrits, E., Peirce, A., & Desroches, J. (2007). Computer simulation
 529 of hydraulic fractures. *International Journal of Rock Mechanics and Mining Sci-*
 530 *ences*, 44(5), 739–757. doi: 10.1016/j.ijrmms.2006.11.006
- 531 Adachi, J. I., & Detournay, E. (2002). Self-similar solution of a plane-strain frac-
 532 ture driven by a power-law fluid. *International Journal for Numerical and Analyt-*
 533 *ical Methods in Geomechanics*, 26(6), 579–604.
- 534 Alessi, R., Marigo, J. J., Maurini, C., & Vidoli, S. (2017). Coupling damage and
 535 plasticity for a phase-field regularisation of brittle, cohesive and ductile fracture:
 536 One-dimensional examples. *International Journal of Mechanical Sciences*, 1–18.
 537 Retrieved from <http://dx.doi.org/10.1016/j.ijmecsci.2017.05.047> doi:
 538 10.1016/j.ijmecsci.2017.05.047
- 539 Alessi, R., Vidoli, S., & De Lorenzis, L. (2018). A phenomenological approach to
 540 fatigue with a variational phase-field model: The one-dimensional case. *Engineer-*
 541 *ing Fracture Mechanics*, 190, 53–73. Retrieved from [https://doi.org/10.1016/j](https://doi.org/10.1016/j.engfracmech.2017.11.036)
 542 [engfracmech.2017.11.036](https://doi.org/10.1016/j.engfracmech.2017.11.036) doi: 10.1016/j.engfracmech.2017.11.036
- 543 Ambati, M., Gerasimov, T., & De Lorenzis, L. (2015). Phase-field model-
 544 ing of ductile fracture. *Computational Mechanics*, 55(5), 1017–1040. Re-
 545 trieved from <http://dx.doi.org/10.1007/s00466-015-1151-4> doi: 10.1007/
 546 s00466-015-1151-4
- 547 Ambrosio, L., & Tortorelli, V. M. (1990). Approximation of functional depending on
 548 jumps by elliptic functional via Γ convergence. *Communications on Pure and Ap-*
 549 *plied Mathematics*, 43(8), 999–1036.
- 550 Ambrosio, L., & Tortorelli, V. M. (1992). On the approximation of free discontinuity
 551 problems. *Boll. Un. Mat. Ital. B (7)*, 6(1), 105–123.
- 552 Amor, H., Marigo, J.-j., & Maurini, C. (2009). Regularized formulation of the vari-
 553 ational brittle fracture with unilateral contact: numerical experiments. *Journal of*
 554 *Mechanics and Physics of Solids*, 57(8), 1209–1229. doi: 10.1016/j.cardiores.2006
 555 .11.005
- 556 Balay, S., Abhyankar, S., Adams, M., Brown, J., Brune, P., Buschelman, K., . . .
 557 Zhang, H. (2019). *{PETS}c Users Manual* (Tech. Rep. No. ANL-95/11 - Revision
 558 3.11). Argonne National Laboratory.

- 559 Belytschko, T., & Black, T. (1999). Elastic crack growth in finite elements with
 560 minimal remeshing. *International Journal for Numerical Methods in Engineering*,
 561 45(5), 601–620. doi: 10.1002/(SICI)1097-0207(19990620)45:5<601::AID-NME598>3
 562 .0.CO;2-S
- 563 Belytschko, T., Moës, N., Usui, S., & Parimi, C. (2001). Arbitrary disconti-
 564 nuities in finite elements. *International Journal for Numerical Methods in*
 565 *Engineering*, 50(4), 993–1013. doi: 10.1002/1097-0207(20010210)50:4<993::
 566 AID-NME164>3.0.CO;2-M
- 567 Biot, M. A. (1941). General Theory of Three-Dimensional Consolidation. *Journal of*
 568 *Applied Physics*, 12(2), 155–164.
- 569 Borden, M. J., Verhoosel, C. V., Scott, M. A., Hughes, T. J. R., & Landis, C. M.
 570 (2012). A phase-field description of dynamic brittle fracture. *Computer Methods*
 571 *in Applied Mechanics and Engineering*, 217-220, 77–95. Retrieved from [http://](http://dx.doi.org/10.1016/j.cma.2012.01.008)
 572 dx.doi.org/10.1016/j.cma.2012.01.008 doi: 10.1016/j.cma.2012.01.008
- 573 Bourdin, B., Chukwudozie, C., & Yoshioka, K. (2012). A variational approach to the
 574 numerical simulation of hydraulic fracturing. *Proceedings - SPE Annual Technical*
 575 *Conference and Exhibition*, 2, 1442–1452. doi: 10.2118/159154-ms
- 576 Bourdin, B., Francfort, G. A., & Marigo, J.-J. (2000). Numerical experiments in re-
 577 visited brittle fracture. *J. Mech. and Phys. of Solids*, 48(4), 797–826.
- 578 Bourdin, B., Francfort, G. A., & Marigo, J.-J. (2008). The variational approach to
 579 fracture. *Journal of Elasticity*, 91(1-3), 5–148.
- 580 Bourdin, B., Larsen, C. J., & Richardson, C. L. (2011). A time-discrete model for
 581 dynamic fracture based on crack regularization. *International Journal of Fracture*,
 582 168(2), 133–143. doi: 10.1007/s10704-010-9562-x
- 583 Braides, A. (1998). *Approximation of Free-Discontinuity Problems* (No.
 584 1694). Springer. Retrieved from [http://www.springerlink.com/content/](http://www.springerlink.com/content/978-3-540-64771-3/)
 585 [978-3-540-64771-3/](http://www.springerlink.com/content/978-3-540-64771-3/)
- 586 Bruna, P. O., Straubhaar, J., Prabhakaran, R., Bertotti, G., Bisdorn, K., Mari-
 587 ethoz, G., & Meda, M. (2019). A new methodology to train fracture network
 588 simulation using multiple-point statistics. *Solid Earth*, 10(2), 537–559. doi:
 589 10.5194/se-10-537-2019
- 590 Bunger, A. P., & Detournay, E. (2008). Experimental validation of the tip asymp-
 591 totics for a fluid-driven crack. *Journal of the Mechanics and Physics of Solids*,
 592 56(11), 3101–3115.
- 593 Bungler, A. P., Gordeliy, E., & Detournay, E. (2013). Comparison between labo-
 594 ratory experiments and coupled simulations of saucer-shaped hydraulic fractures
 595 in homogeneous brittle-elastic solids. *Journal of the Mechanics and Physics of*
 596 *Solids*, 61(7), 1636–1654.
- 597 Bungler, A. P., Jeffrey, R. G., & Detournay, E. (2008). Evolution and morphology
 598 of saucer-shaped sills in analogue experiments. In *Structure and emplacement of*
 599 *high-level magmatic systems* (pp. 109–120). Geological Society, London.
- 600 Canet, C., Hernández-Cruz, B., Jiménez-Franco, A., Pi, T., Peláez, B., Villanueva-
 601 Estrada, R. E., . . . Salinas, S. (2015). Combining ammonium mapping and short-
 602 wave infrared (SWIR) reflectance spectroscopy to constrain a model of hydrother-
 603 mal alteration for the Acoculco geothermal zone, Eastern Mexico. *Geothermics*,
 604 53(July), 154–165. doi: 10.1016/j.geothermics.2014.05.012
- 605 Carrara, P., Ambati, M., Alessi, R., & Lorenzis, L. D. (2019). A framework to
 606 model the fatigue behavior of brittle materials based on a variational phase-
 607 field approach. *Computer Methods in Applied Mechanics and Engineering*,
 608 112731. Retrieved from [http://www.sciencedirect.com/science/article/](http://www.sciencedirect.com/science/article/pii/S0045782519306218)
 609 [pii/S0045782519306218](http://www.sciencedirect.com/science/article/pii/S0045782519306218) doi: <https://doi.org/10.1016/j.cma.2019.112731>
- 610 Choo, J., & Sun, W. C. (2018). Cracking and damage from crystallization in
 611 pores: Coupled chemo-hydro-mechanics and phase-field modeling. *Computer*
 612 *Methods in Applied Mechanics and Engineering*, 335(March), 347–379. doi:

- 10.1016/j.cma.2018.01.044
- Chukwudozie, C., Bourdin, B., & Yoshioka, K. (2019). A variational phase-field model for hydraulic fracturing in porous media. *Computer Methods in Applied Mechanics and Engineering*, *347*, 957–982. Retrieved from <https://doi.org/10.1016/j.cma.2018.12.037> doi: 10.1016/j.cma.2018.12.037
- Chukwudozie, C., Bourdin, B., Yoshioka, K., Buchmann, T., & Connolly, P. (2013). A new modeling approach to natural fracturing process. *47th US Rock Mechanics / Geomechanics Symposium 2013*, *4*, 2663–2672.
- Davies, R., Foulger, G., Bindley, A., & Styles, P. (2013). Induced seismicity and hydraulic fracturing for the recovery of hydrocarbons. *Marine and petroleum geology*, *45*, 171–185.
- Del Piero, G. (1989). Constitutive equation and compatibility of the external loads for linear elastic masonry-like materials. *Meccanica*, *24*(3), 150–162. doi: 10.1007/BF01559418
- Detournay, E. (2016). Mechanics of Hydraulic Fractures. *Annual Review of Fluid Mechanics*, *48*(1), 311–339. doi: 10.1146/annurev-fluid-010814-014736
- Detournay, E., & Cheng, A. H. D. (1993). Fundamentals of poroelasticity. *Comprehensive rock engineering. Vol. 2, II*, 113–171. doi: 10.1017/cbo9781139051132.003
- Economides, M. J., & Nolte, K. G. (1989). *Reservoir Stimulation* (No. Third Edition). Wiley. doi: 10.15713/ins.mmj.3
- Ehlers, W., & Luo, C. (2017). A phase-field approach embedded in the Theory of Porous Media for the description of dynamic hydraulic fracturing. *Comput. Methods Appl. Mech. Engrg.*, *315*, 348–368. Retrieved from <http://dx.doi.org/10.1016/j.cma.2016.10.045> doi: 10.1016/j.cma.2016.10.045
- Elders, W. A., Fridhlefsson, G. Ó., & Albertsson, A. (2014). Drilling into magma and the implications of the Iceland Deep Drilling Project (IDDP) for high-temperature geothermal systems worldwide. *Geothermics*, *49*, 111–118.
- Ellsworth, W. L., Giardini, D., Townend, J., Ge, S., & Shimamoto, T. (2019). Triggering of the Pohang, Korea, Earthquake (M w 5.5) by Enhanced Geothermal System Stimulation. *Seismological Research Letters*, *90*(5), 1844–1858.
- Fischer, A. G., & Marigo, J.-J. (2019). Gradient damage models applied to dynamic fragmentation of brittle materials. *International Journal of Fracture*. Retrieved from <https://doi.org/10.1007/s10704-019-00356-y> doi: 10.1007/s10704-019-00356-y
- Fox, D. B., Sutter, D., Beckers, K. F., Lukawski, M. Z., Koch, D. L., Anderson, B. J., & Tester, J. W. (2013). Sustainable heat farming: Modeling extraction and recovery in discretely fractured geothermal reservoirs. *Geothermics*, *46*, 42–54. Retrieved from <http://dx.doi.org/10.1016/j.geothermics.2012.09.001> doi: 10.1016/j.geothermics.2012.09.001
- Francfort, G. A., & Marigo, J.-J. (1998). Revisiting brittle fracture as an energy minimization problem. *J. Mech. and Phys. of Solids*, *46*(8), 1319–1342.
- Franklin, J. A., Zongqi, S., Atkinson, B. K., Meredith, P. G., Rummel, F., Muller, W., ... Bobrov, G. F. (1988). ISRM SUGGESTED METHODS FOR DETERMINING THE FRACTURE TOUGHNESS OF ROCK. *International Journal of Rock Mechanics and Mining Sciences & Geomechanics Abstracts*, *25*(2), 71–96. Retrieved from <http://linkinghub.elsevier.com/retrieve/pii/S0148906296000150> doi: 10.1016/S0148-9062(96)00015-0
- Freddi, F., & Royer-Carfagni, G. (2011). Variational fracture mechanics to model compressive splitting of masonry-like materials. *Annals of Solid and Structural Mechanics*, *2*(2-4), 57–67. doi: 10.1007/s12356-011-0018-4
- Fu, P., Settghost, R. R., Hao, Y., Morris, J. P., & Ryerson, F. J. (2017). The Influence of Hydraulic Fracturing on Carbon Storage Performance. *Journal of Geophysical Research: Solid Earth*, *122*(12), 9931–9949. doi: 10.1002/2017JB014942

- 667 Gao, H., & Rice, J. R. (1987). Somewhat circular tensile cracks. *International Jour-*
668 *nal of Fracture*, 155–174.
- 669 Garagash, D., & Detournay, E. (2000). The tip region of a fluid-driven fracture in an
670 elastic medium. *J. Appl. Mech.*, 67(1), 183–192.
- 671 Garagash, D. I., Detournay, E., & Adachi, J. I. (2011). Multiscale tip asymptotics in
672 hydraulic fracture with leak-off. *Journal of Fluid Mechanics*, 669, 260–297.
- 673 Garagash, D. I., & Germanovich, L. N. (2012). Nucleation and arrest of dy-
674 namic slip on a pressurized fault. *Journal of Geophysical Research: Solid Earth*,
675 117(B10).
- 676 Geertsma, J., & De Klerk, F. (1969). Rapid Method of Predicting Width and Extent
677 of Hydraulically Induced Fractures. *J Petroleum Technology*, 21(12), 1571–1581.
678 doi: 10.2118/2458-pa
- 679 Griffith, A. A. (1921). The Phenomena of Rupture and Flow in Solids. *Philo-*
680 *sophical transactions of the royal society of london. Series A, containing papers*
681 *of a mathematical or physical character*, 221(1921), 163–198. Retrieved from
682 <https://www.jstor.org/stable/91192>
- 683 Guo, H., Aziz, N. I., & Schmidt, L. C. (1993). Rock fracture-toughness determina-
684 tion by the Brazilian test. *Engineering Geology*, 33(3), 177–188. doi: 10.1016/0013
685 -7952(93)90056-I
- 686 Gupta, P., & Duarte, C. A. (2016). Coupled formulation and algorithms for the
687 simulation of non-planar three-dimensional hydraulic fractures using the general-
688 ized finite element method. *International Journal for Numerical and Analytical*
689 *Methods in Geomechanics*, 40(10), 1402–1437. doi: 10.1002/nag.2485
- 690 Hansen-Dörr, A. C., de Borst, R., Hennig, P., & Kästner, M. (2019). Phase-
691 field modelling of interface failure in brittle materials. *Computer Meth-*
692 *ods in Applied Mechanics and Engineering*, 346, 25–42. Retrieved from
693 <http://www.sciencedirect.com/science/article/pii/S0045782518305772>
694 doi: <https://doi.org/10.1016/j.cma.2018.11.020>
- 695 Heidbach, O., Rajabi, M., Reiter, K., Ziegler, M., & Team WSM. (2016). World
696 Stress Map Database Release 2016. *GFZ Data Services*. Retrieved from [http://](http://doi.org/10.5880/WSM.2016.001)
697 doi.org/10.5880/WSM.2016.001
- 698 Heider, Y., & Markert, B. (2017). A phase-field modeling approach of hydraulic frac-
699 ture in saturated porous media. *Mechanics Research Communications*, 80, 38–46.
700 Retrieved from <http://dx.doi.org/10.1016/j.mechrescom.2016.07.002> doi:
701 10.1016/j.mechrescom.2016.07.002
- 702 Hofacker, M., & Miehe, C. (2012). Continuum phase field modeling of dynamic frac-
703 ture: Variational principles and staggered FE implementation. *International Jour-*
704 *nal of Fracture*, 178(1-2), 113–129. doi: 10.1007/s10704-012-9753-8
- 705 Irwin, G. R. (1957). Analysis of Stresses and Strains Near the End of a Crack
706 Traversing a Plate. *Journal of Applied Mechanics*, 24, 361–364.
- 707 Jeffrey, R. G., Bungler, A. P., Lecampion, B., Zhang, X., Chen, Z. R., Van As, A., . . .
708 Mainguy, M. (2009). Measuring hydraulic fracture growth in naturally fractured
709 rock. *Proceedings - SPE Annual Technical Conference and Exhibition*, 6(January),
710 3750–3768. doi: 10.2118/124919-ms
- 711 Jeffrey, R. G., Weber, C. R., Vlahovic, W., & Enever, J. R. (1994). Hydraulic frac-
712 turing experiments in the great northern coal seam. *SPE - Asia Pacific Oil & Gas*
713 *Conference*, 361–371. doi: 10.2523/28779-ms
- 714 Karypis, G., & Kumar, V. (1998). A fast and high quality multilevel scheme for par-
715 titioning irregular graphs. *SIAM Journal of Scientific Computing*, 20(1), 359–392.
716 doi: 10.1137/S1064827595287997
- 717 Kolditz, O., Bauer, S., Bilke, L., Böttcher, N., Delfs, J. O., Fischer, T., . . . Zehner,
718 B. (2012). OpenGeoSys: An open-source initiative for numerical simulation of
719 thermo-hydro-mechanical/chemical (THM/C) processes in porous media. *Environ-*
720 *mental Earth Sciences*, 67(2), 589–599. doi: 10.1007/s12665-012-1546-x

- 721 Kuhn, C., Noll, T., & Müller, R. (2016). On phase field modeling of ductile fracture.
722 *GAMM Mitteilungen*, 39(1), 35–54. doi: 10.1002/gamm.201610003
- 723 Lecampion, B., Bungler, A., & Zhang, X. (2018). Numerical methods for hydraulic
724 fracture propagation: a review of recent trends. *Journal of natural gas science and*
725 *engineering*, 49, 66–83.
- 726 Lee, S., Wheeler, M. F., & Wick, T. (2017). Iterative coupling of flow, ge-
727 omechanics and adaptive phase-field fracture including level-set crack width
728 approaches. *Journal of Computational and Applied Mathematics*, 314, 40–
729 60. Retrieved from <http://dx.doi.org/10.1016/j.cam.2016.10.022> doi:
730 10.1016/j.cam.2016.10.022
- 731 Legarth, B. A., & Saadat, A. (2005). Energy Consumption for Geothermal Wells.
732 *Database*(April), 24–29.
- 733 Lepillier, B., Bruna, P.-O., Bruhn, D., Bastesen, E., Daniilidis, A., Garcia, Ó.,
734 ... Wheeler, W. (2020). From outcrop scanlines to discrete fracture net-
735 works, an integrative workflow. *Journal of Structural Geology*, 133(January),
736 103992. Retrieved from [http://www.sciencedirect.com/science/article/pii/](http://www.sciencedirect.com/science/article/pii/S0191814119303050)
737 [S0191814119303050](http://www.sciencedirect.com/science/article/pii/S0191814119303050) doi: <https://doi.org/10.1016/j.jsg.2020.103992>
- 738 Lepillier, B., Daniilidis, A., Gholizadeh, N., Bruna, P.-o., Juliane, K., & Bruhn,
739 D. (2019). A fracture flow permeability and stress dependency simulation ap-
740 plied to multi-reservoirs , multi-production scenarios analysis. *Geothermal En-*
741 *ergy*. Retrieved from <https://rdcu.be/bPyIc> doi: [https://doi.org/10.1186/](https://doi.org/10.1186/s40517-019-0141-8)
742 [s40517-019-0141-8](https://doi.org/10.1186/s40517-019-0141-8)
- 743 Li, T., Marigo, J.-J., Guilbaud, D., & Potapov, S. (2016). Gradient damage mod-
744 eling of brittle fracture in an explicit dynamic context. *International Journal for*
745 *Numerical Methods in Engineering*, 00(March), 1–25. doi: 10.1002/nme
- 746 Liotta, D., Bastesen, E., Bianco, C., Brogi, A., Caggianelli, A., Garduño-Monroy,
747 V.-H., ... Zucchi, M. (2020). Analogue Geothermal Systems In Mexico : Insights
748 Into The Deep Part Of Los Humeros Geothermal Field From The Las Minas
749 Mining Area (Eastern Mexico). *Proceedings World Geothermal Congress 2020*,
750 1–9.
- 751 Lopez-Comino, J. A., Cesca, S., Kriegerowski, M., Heimann, S., Dahm, T., Mirek,
752 J., & Lasocki, S. (2017). Monitoring performance using synthetic data for induced
753 microseismicity by hydrofracking at the Wysin site (Poland). *Geophysical Journal*
754 *International*, 42–55.
- 755 López-Hernández, A., García-Estrada, G., Aguirre-Díaz, G., González-Partida, E.,
756 Palma-Guzmán, H., & Quijano-León, J. L. (2009). Hydrothermal activity in
757 the Tulancingo-Acozol Caldera Complex, central Mexico: Exploratory studies.
758 *Geothermics*, 38(3), 279–293. doi: 10.1016/j.geothermics.2009.05.001
- 759 Lu, R., Nagel, T., Shao, H., Kolditz, O., & Shao, H. (2018). Modeling of
760 Dissolution-Induced Permeability Evolution of a Granite Fracture Under Crustal
761 Conditions. *Journal of Geophysical Research: Solid Earth*, 123(7), 5609–5627.
- 762 McClure, M. W., & Horne, R. N. (2014). An investigation of stimulation mecha-
763 nisms in Enhanced Geothermal Systems. *International Journal of Rock Mechan-*
764 *ics and Mining Sciences*, 72(November), 242–260. Retrieved from [http://dx.doi](http://dx.doi.org/10.1016/j.ijrmms.2014.07.011)
765 [.org/10.1016/j.ijrmms.2014.07.011](http://dx.doi.org/10.1016/j.ijrmms.2014.07.011) doi: 10.1016/j.ijrmms.2014.07.011
- 766 McClure Mark, W., Mohsen, B., Sogo, S., & Jian, H. (2015). Fully coupled hy-
767 dromechanical simulation of hydraulic fracturing in 3D discrete-fracture networks.
768 *SPE Journal*, 21(4), 1302–1320. doi: 10.2118/173354-ms
- 769 Miehe, C., Hofacker, M., Schänzel, L. M., & Aldakheel, F. (2015). Phase field
770 modeling of fracture in multi-physics problems. Part II. Coupled brittle-to-
771 ductile failure criteria and crack propagation in thermo-elastic-plastic solids.
772 *Computer Methods in Applied Mechanics and Engineering*, 294, 486–522. doi:
773 10.1016/j.cma.2014.11.017
- 774 Miehe, C., Mauthe, S., & Teichtmeister, S. (2015). Minimization principles for the

- 775 coupled problem of Darcy-Biot-type fluid transport in porous media linked to
 776 phase field modeling of fracture. *Journal of the Mechanics and Physics of Solids*,
 777 *82*, 186–217. Retrieved from <http://dx.doi.org/10.1016/j.jmps.2015.04.006>
 778 doi: 10.1016/j.jmps.2015.04.006
- 779 Miehe, C., Welschinger, F., & Hofacker, M. (2010). Thermodynamically con-
 780 sistent phase-field models of fracture: Variational principles and multi-field FE
 781 implementations. *International Journal for Numerical Methods in Engineering*,
 782 *83*(10), 1273–1311. Retrieved from <http://dx.doi.org/10.1002/nme.2861> doi:
 783 10.1002/nme.2861
- 784 Mikelić, A., Wheeler, M. F., & Wick, T. (2015). A Phase-Field method for prop-
 785 agating fluid-filled fractures coupled to a surrounding porous medium. *Multiscale*
 786 *Modeling & Simulation*, *48*(1), 162–186.
- 787 Milanese, E., Rizzato, P., Pesavento, F., Secchi, S., & Schrefler, B. A. (2016). An
 788 explanation for the intermittent crack tip advancement and pressure fluctuations
 789 in hydraulic fracturing. *Hydraul Fract J*, *3*(2), 30–43.
- 790 Moës, N., Dolbow, J., & Belytschko, T. (1999). A finite element method for crack
 791 growth without remeshing. *International Journal for Numerical Methods in En-*
 792 *gineering*, *46*(1), 131–150. doi: 10.1002/(SICI)1097-0207(19990910)46:1<131::AID-
 793 -NME726>3.0.CO;2-J
- 794 Nordgren, R. P. (1972). Propagation of a Vertical Hydraulic Fracture. *Society of*
 795 *Petroleum Engineers Journal*, *12*(04), 306–314. doi: 10.2118/3009-pa
- 796 Perkins, T. K., & Kern, L. R. (1961). Widths of Hydraulic Fractures. *Journal of*
 797 *Petroleum Technology*, *13*(09), 937–949. doi: 10.2118/89-pa
- 798 Renshaw, C. E., & Pollard, D. D. (1995). An experimentally verified criterion for
 799 propagation across unbounded frictional interfaces in brittle, linear elastic mate-
 800 rials. *International Journal of Rock Mechanics and Mining Sciences and*, *32*(3),
 801 237–249. doi: 10.1016/0148-9062(94)00037-4
- 802 Santillán, D., Juanes, R., & Cueto-Felgueroso, L. (2017). Phase field model of fluid-
 803 driven fracture in elastic media: Immersed-fracture formulation and validation
 804 with analytical solutions. *J Geophys. Res.-Sol Ea.* doi: 10.1002/2016JB013572
- 805 Savitski, A. A., & Detournay, E. (2002). Propagation of a penny-shaped fluid-driven
 806 fracture in an impermeable rock: asymptotic solutions. *International journal of*
 807 *solids and structures*, *39*(26), 6311–6337.
- 808 Schlüter, A., Willenbücher, A., Kuhn, C., & Müller, R. (2014). Phase field approx-
 809 imation of dynamic brittle fracture. *Computational Mechanics*, *54*(5), 1141–1161.
 810 doi: 10.1007/s00466-014-1045-x
- 811 Schultz, R., Stern, V., Novakovic, M., Atkinson, G., & Gu, Y. J. (2015). Hydraulic
 812 fracturing and the Crooked Lake Sequences: Insights gleaned from regional seismic
 813 networks. *Geophysical Research Letters*, *42*(8), 2750–2758.
- 814 Scott, S. W., & Driesner, T. (2018). Permeability changes resulting from quartz pre-
 815 cipitation and dissolution around upper crustal intrusions. *Geofluids*, *2018*.
- 816 Seiler, M., Hantschke, P., Brosius, A., & Kästner, M. (2018). A numerically efficient
 817 phase-field model for fatigue fracture - 1D analysis. *Pamm*, *18*(1), e201800207.
 818 doi: 10.1002/pamm.201800207
- 819 Shiozawa, S., Lee, S., & Wheeler, M. F. (2019). The effect of stress boundary con-
 820 ditions on fluid-driven fracture propagation in porous media using a phase-field
 821 modeling approach. *International Journal for Numerical and Analytical Methods*
 822 *in Geomechanics*(February 2018), 1–25. doi: 10.1002/nag.2899
- 823 Singurindy, O., & Berkowitz, B. (2005). The role of fractures on coupled dissolution
 824 and precipitation patterns in carbonate rocks. *Advances in water resources*, *28*(5),
 825 507–521.
- 826 Tanne, E. (2017). *Thèse de doctorat de l ’ université Paris-Saclay* (Unpublished doc-
 827 toral dissertation).
- 828 Tanné, E., Li, T., Bourdin, B., Marigo, J.-J., & Maurini, C. (2018). Crack nucle-

- 829 ation in variational phase-field models of brittle fracture. *J. Mech. Phys. Solids*,
830 110, 80–99. doi: 10.1016/j.jmps.2017.09.006
- 831 Tsai, V. C., & Rice, J. R. (2010). A model for turbulent hydraulic fracture and
832 application to crack propagation at glacier beds. *Journal of Geophysical Research:*
833 *Earth Surface*, 115(F3).
- 834 Wang, H. Y. (2019). Hydraulic fracture propagation in naturally fractured reser-
835 voirs: Complex fracture or fracture networks. *Journal of Natural Gas Science*
836 *and Engineering*, 68(June), 102911. Retrieved from [https://doi.org/10.1016/](https://doi.org/10.1016/j.jngse.2019.102911)
837 [j.jngse.2019.102911](https://doi.org/10.1016/j.jngse.2019.102911) doi: 10.1016/j.jngse.2019.102911
- 838 Warpinski, N. R., & Teufel, L. W. (1987). Influence of Geologic Discontinuities on
839 Hydraulic Fracture Propagation (includes associated papers 17011 and 17074).
840 *Journal of Petroleum Technology*, 39(02), 209–220. doi: 10.2118/13224-pa
- 841 Watanabe, N., Saito, K., Okamoto, A., Nakamura, K., Ishibashi, T., Saishu, H., ...
842 Tsuchiya, N. (2020). Stabilizing and enhancing permeability for sustainable and
843 profitable energy extraction from superhot geothermal environments. *Applied*
844 *Energy*, 260, 114306.
- 845 Weng, X. (2014). Modeling of complex hydraulic fractures in naturally fractured for-
846 mation. *Journal of Unconventional Oil and Gas Resources*, 9, 114–135. Retrieved
847 from [http://dx.doi.org/10.1016/j.juogr.](http://dx.doi.org/10.1016/j.juogr.2014.07.001)2014.07.001 doi: 10.1016/j.juogr
848 .2014.07.001
- 849 Weng, X., Kresse, O., Cohen, C., Wu, R., & Gu, H. (2011). Modeling of hydraulic
850 fracture network propagation in a naturally fractured formation. *Society of*
851 *Petroleum Engineers - SPE Hydraulic Fracturing Technology Conference 2011*,
852 i, 298–315. doi: 10.2118/140253-ms
- 853 Weydt, L., Bär, K., Colombero, C., Comina, C., Deb, P., Lepillier, B., ... Sass,
854 I. (2018). Outcrop analogue study to determine reservoir properties of the Los
855 Humeros and Acoculco geothermal fields, Mexico. *Geophysical Research Abstracts*
856 *EGU General Assembly*, 20(727550), 2018–7228. doi: 10.5194/adgeo-45-281-2018
- 857 Wheeler, M. F., Wick, T., & Wollner, W. (2014). An augmented-Lagrangian
858 method for the phase-field approach for pressurized fractures. *Computer Meth-*
859 *ods in Applied Mechanics and Engineering*, 271, 69–85. Retrieved from [http://](http://dx.doi.org/10.1016/j.cma.2013.12.005)
860 dx.doi.org/10.1016/j.cma.2013.12.005 doi: 10.1016/j.cma.2013.12.005
- 861 Wilson, Z., & Landis, C. (2016). Phase-field modeling of hydraulic fracture. *J. Mech.*
862 *Phys. Solids*, 96, 264–290. Retrieved from [http://dx.doi.org/10.1016/j.jmps](http://dx.doi.org/10.1016/j.jmps.2016.07.019)
863 .2016.07.019 doi: 10.1016/j.jmps.2016.07.019
- 864 Xia, L., Yvonnet, J., & Ghabezloo, S. (2017). Phase field modeling of hydraulic
865 fracturing with interfacial damage in highly heterogeneous fluid-saturated
866 porous media. *Engineering Fracture Mechanics*, 186(October), 158–180. doi:
867 10.1016/j.engfracmech.2017.10.005
- 868 Yazid, A., Abdelkader, N., & Abdelmadjid, H. (2009). A state-of-the-art review
869 of the X-FEM for computational fracture mechanics. *Applied Mathematical Mod-*
870 *elling*, 33(12), 4269–4282. doi: 10.1016/j.apm.2009.02.010
- 871 Yew, C. H., & Weng, X. (2015). Fracture propagation in a naturally fractured for-
872 mation. *Mechanics of Hydraulic Fracturing*, 1, 133–175. doi: 10.1016/b978-0-12
873 -420003-6.00007-0
- 874 Yoshioka, K., & Bourdin, B. (2016). A variational hydraulic fracturing model cou-
875 pled to a reservoir simulator. *International Journal of Rock Mechanics and Mining*
876 *Sciences*, 88, 137–150. Retrieved from [http://dx.doi.org/10.1016/j.ijrmmms](http://dx.doi.org/10.1016/j.ijrmmms.2016.07.020)
877 .2016.07.020 doi: 10.1016/j.ijrmmms.2016.07.020
- 878 Yoshioka, K., Parisio, F., Naumov, D., Lu, R., Kolditz, O., & Nagel, T. (2019).
879 Comparative verification of discrete and smeared numerical approaches for the
880 simulation of hydraulic fracturing. *GEM - International Journal on Geomathemat-*
881 *ics*, 10(1), 1–35. Retrieved from <https://doi.org/10.1007/s13137-019-0126-6>
882 doi: 10.1007/s13137-019-0126-6

883 Zoback, M. D., Barton, C. A., Brudy, M., Castillo, D. A., Finkbeiner, T., Grol-
884 limund, B. R., . . . Wiprut, D. J. (2003). Determination of stress orientation and
885 magnitude in deep wells. *International Journal of Rock Mechanics and Mining*
886 *Sciences*, 40(7-8), 1049–1076. doi: 10.1016/j.ijrmms.2003.07.001

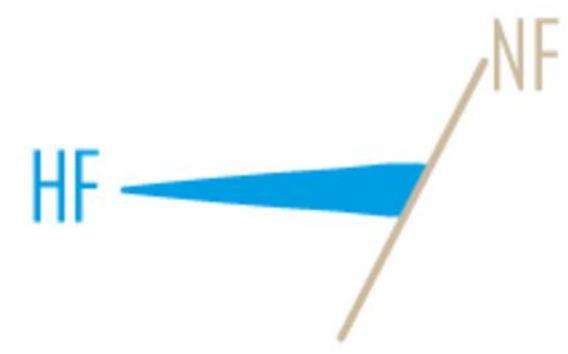
Figure 1.

Time Step = [initial]

Time Step = [intermediate]

HF stopped

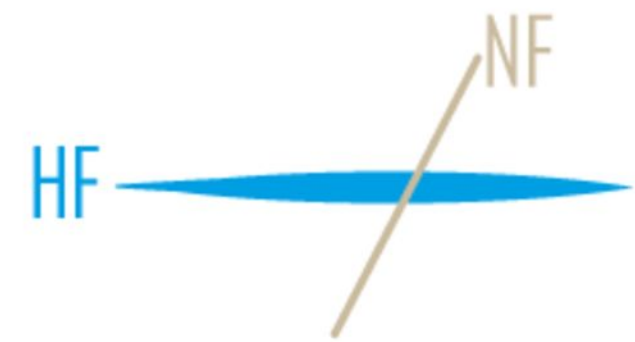
HF propagates in NF (=branching)



HF approaching NF...

HF crosses

HF branches + crosses NF



HF crosses with offset

HF branches + crosses + with offset

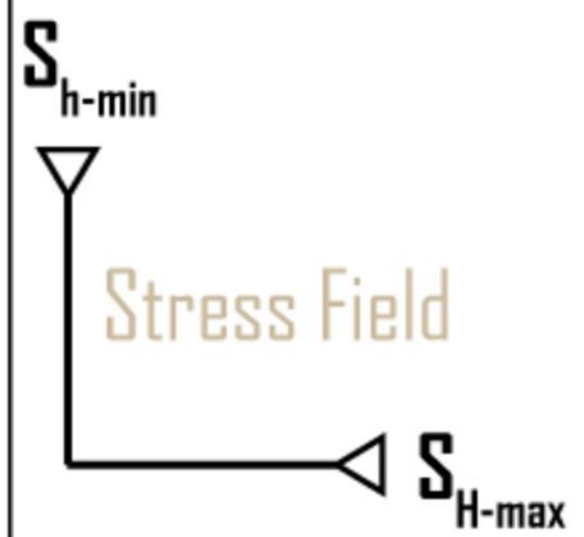


Figure 2.

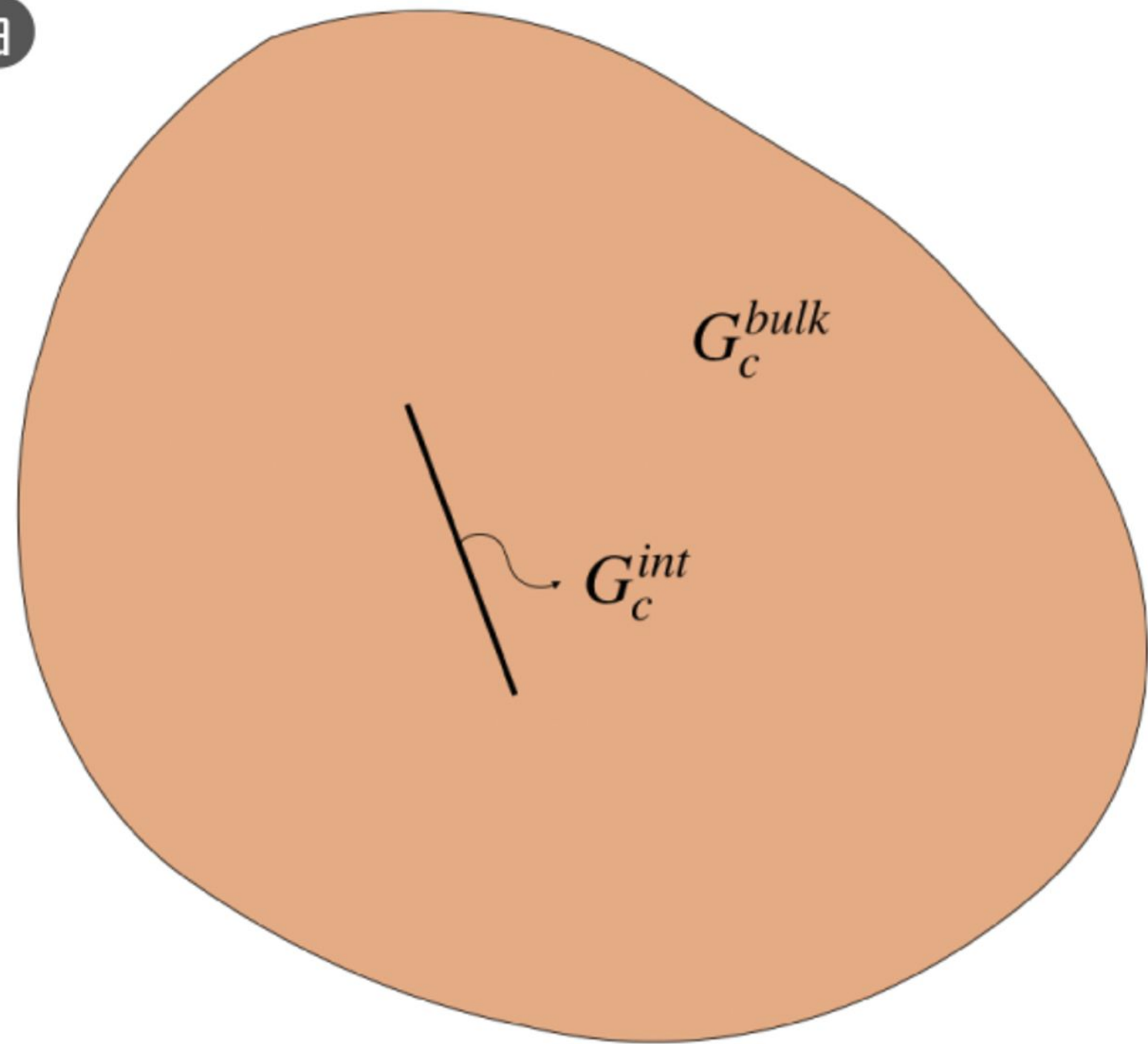
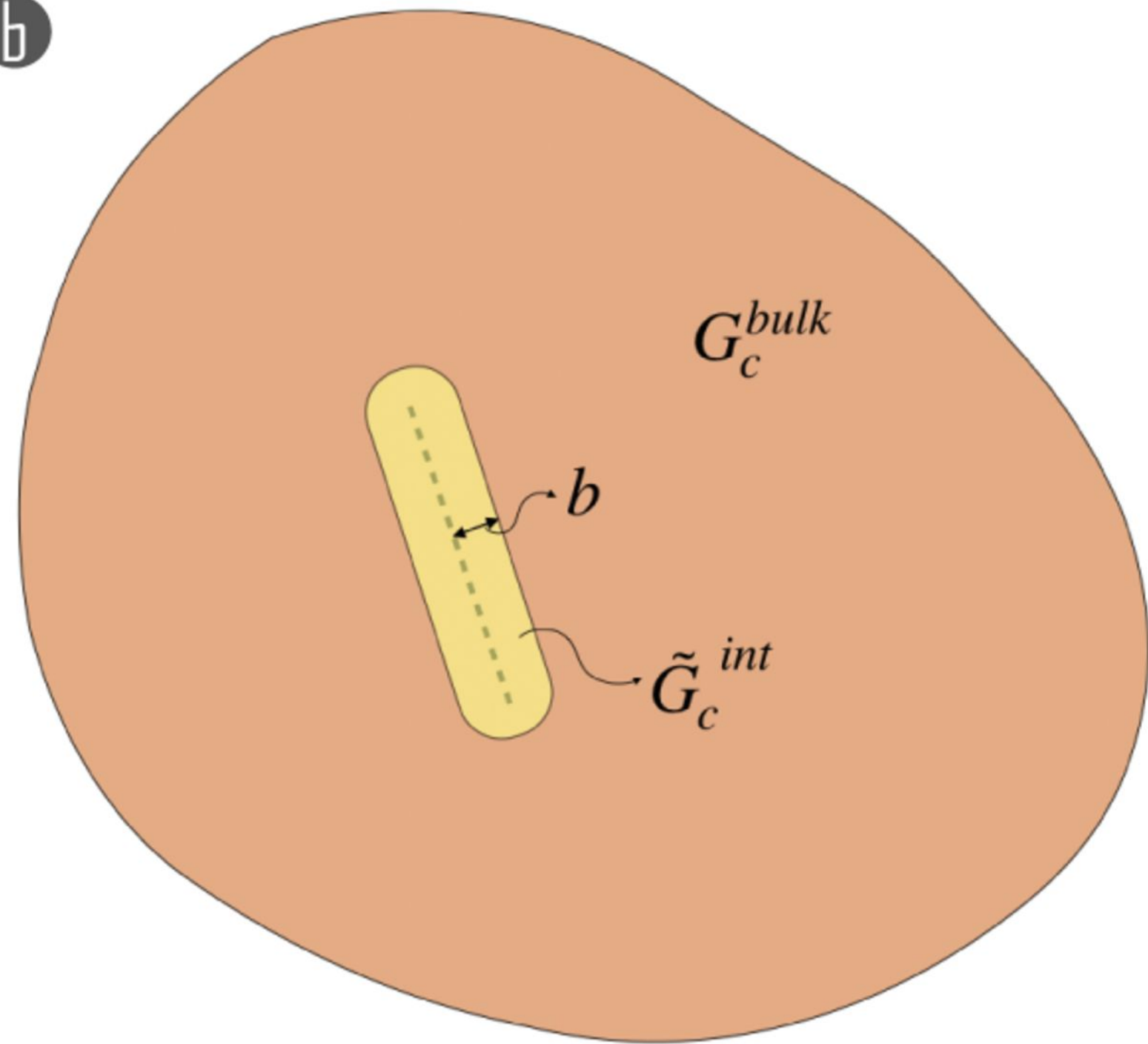
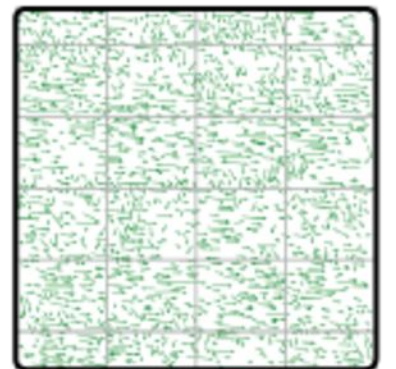
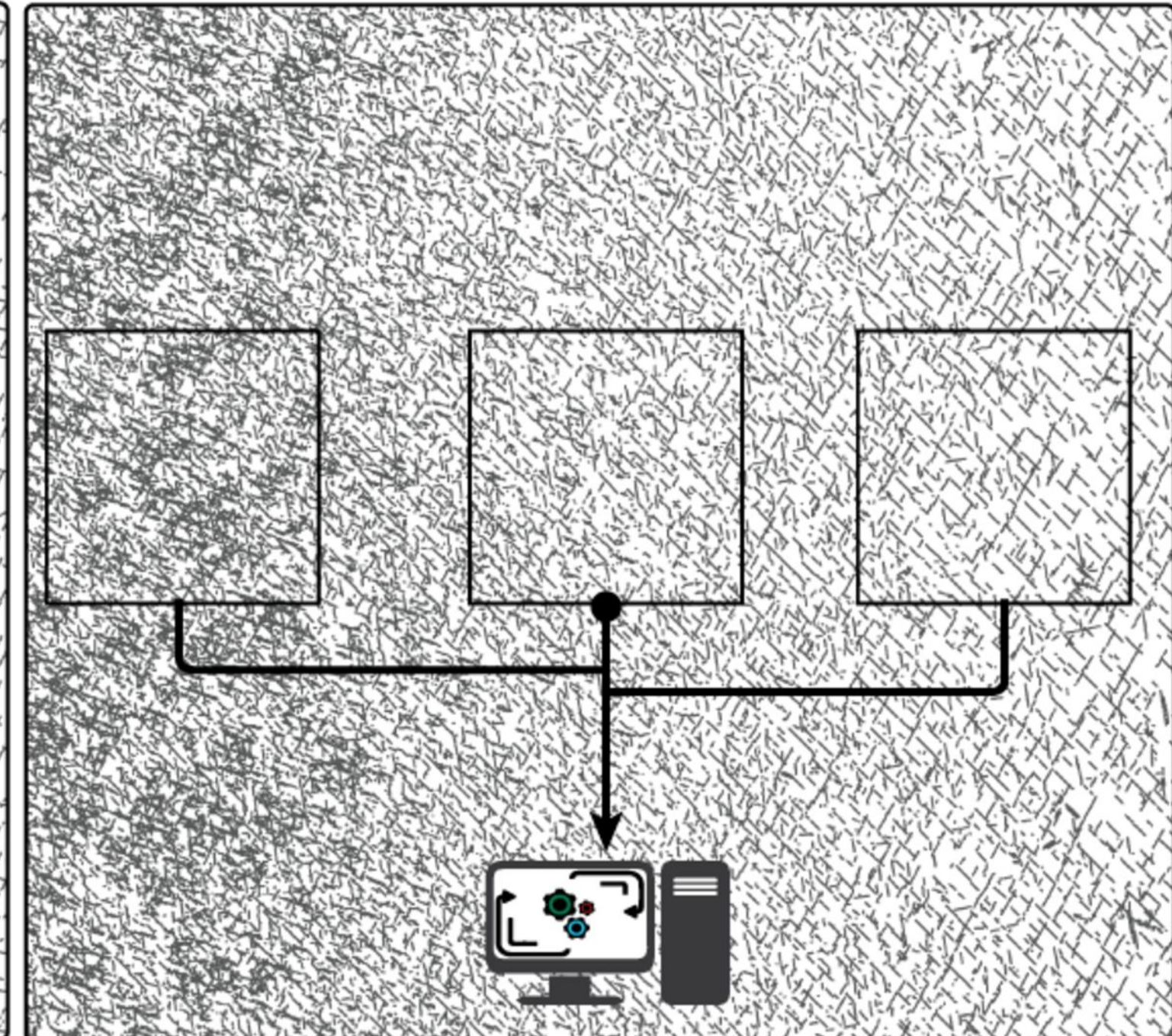
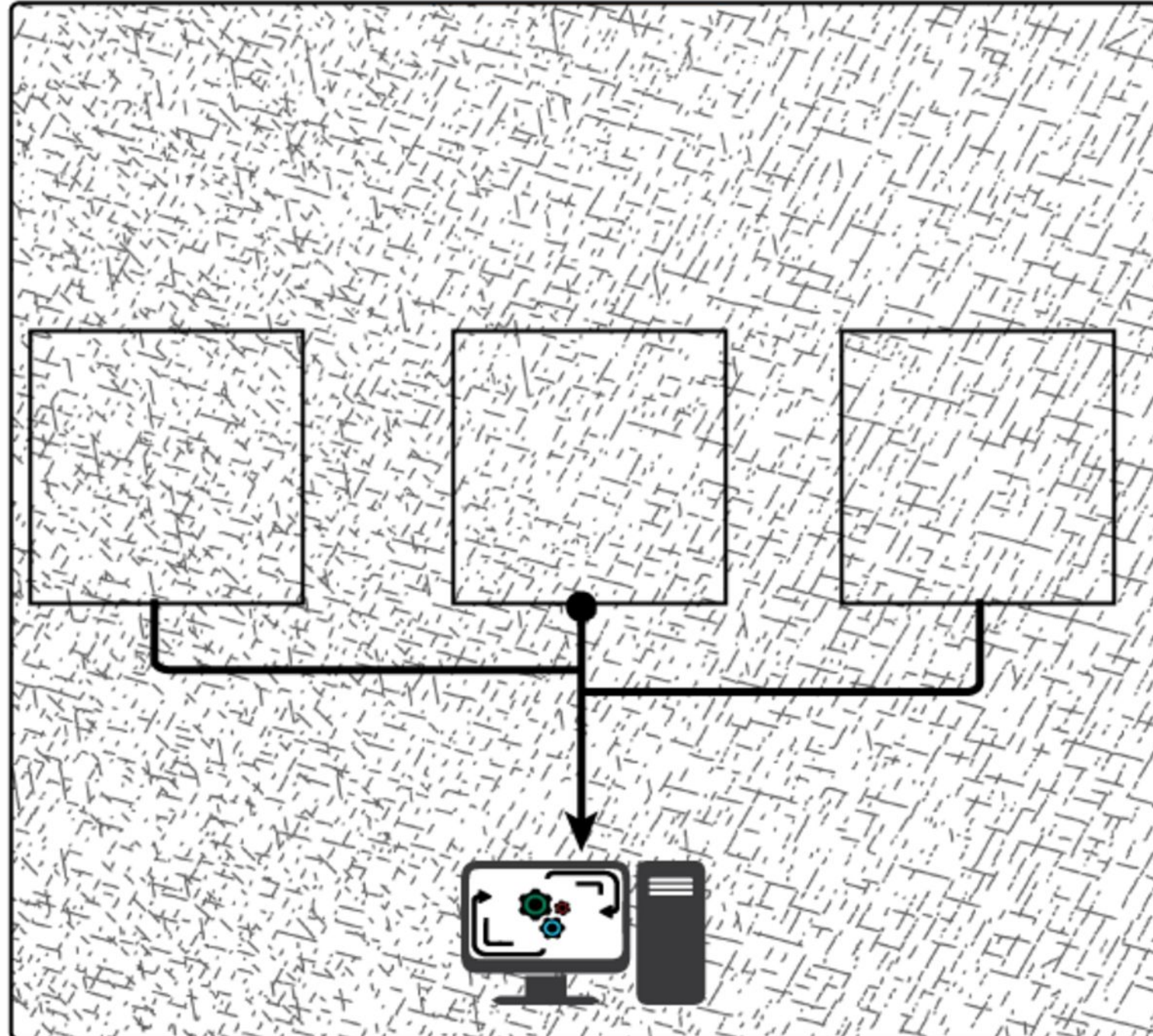
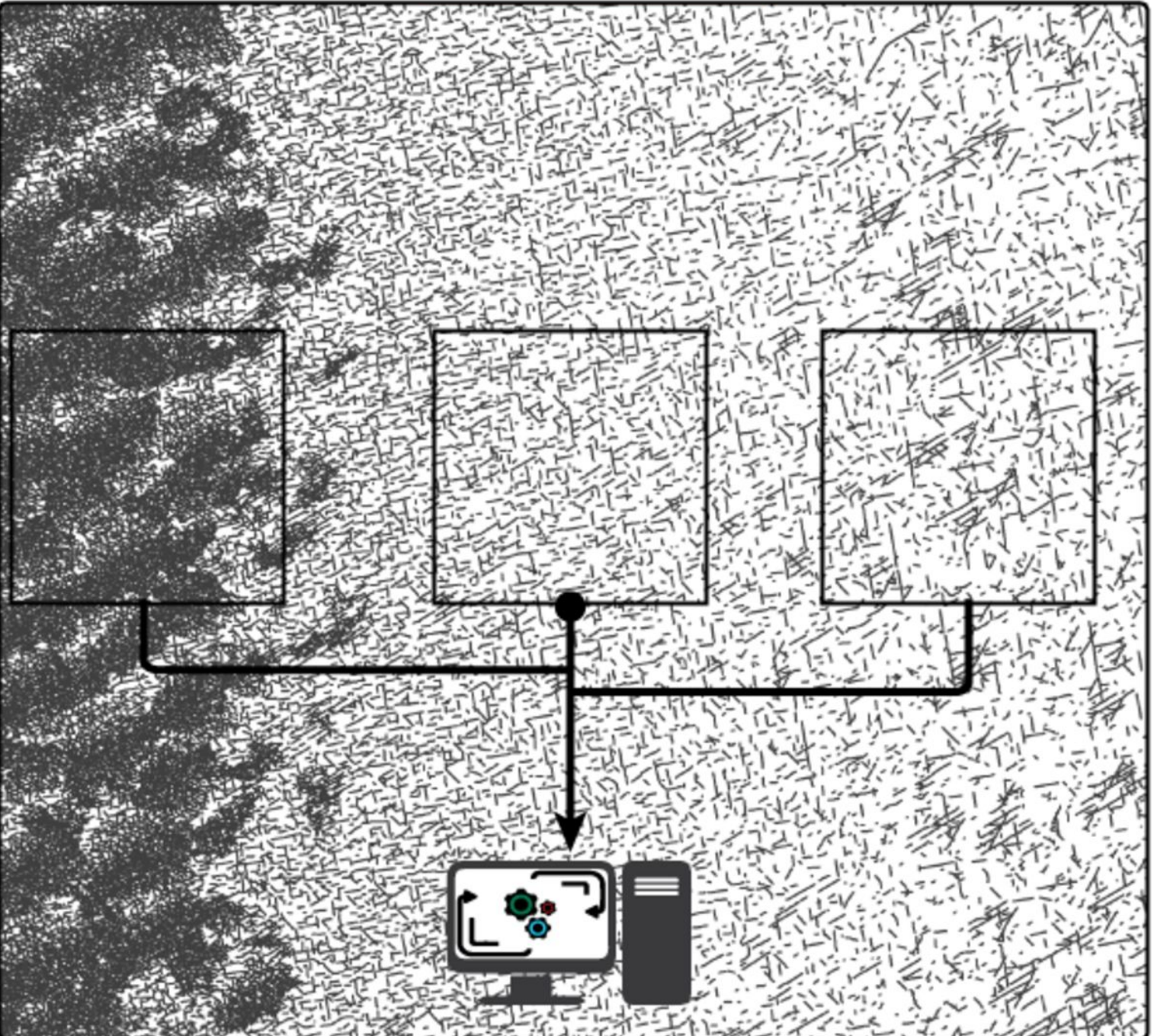
a**b**

Figure 3.

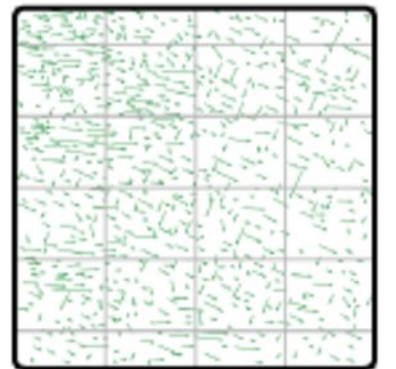
 Limestone

 Marble

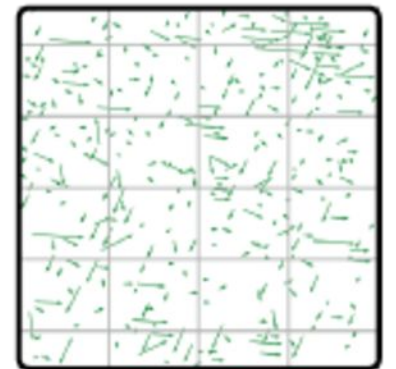
 Skarn



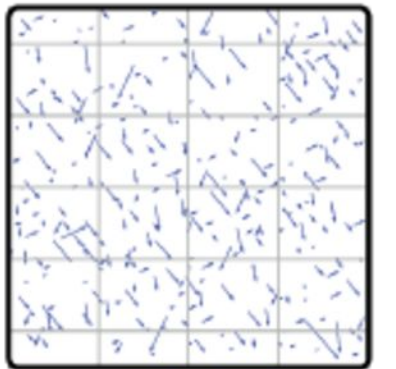
Lm-01



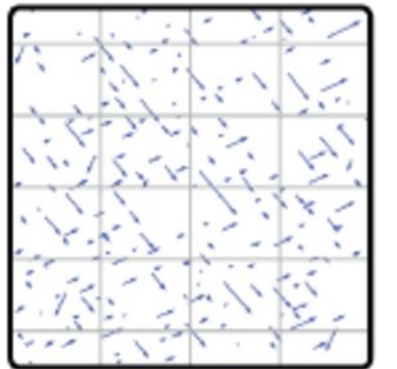
Lm-02



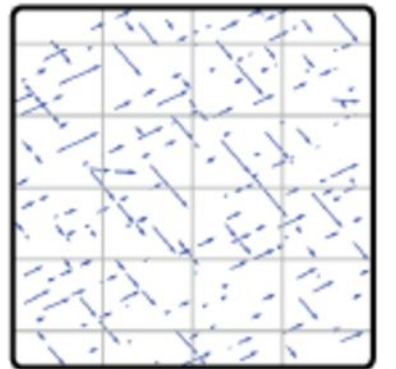
Lm-03



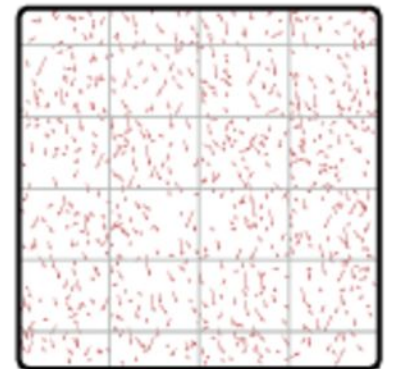
Ma-01



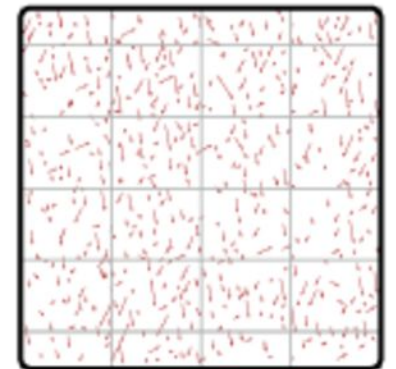
Ma-02



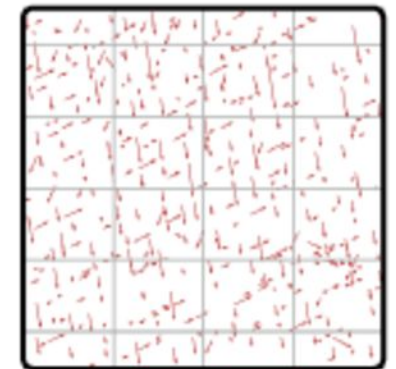
Ma-03



Sk-01



Sk-02



Sk-03

Figure 4.

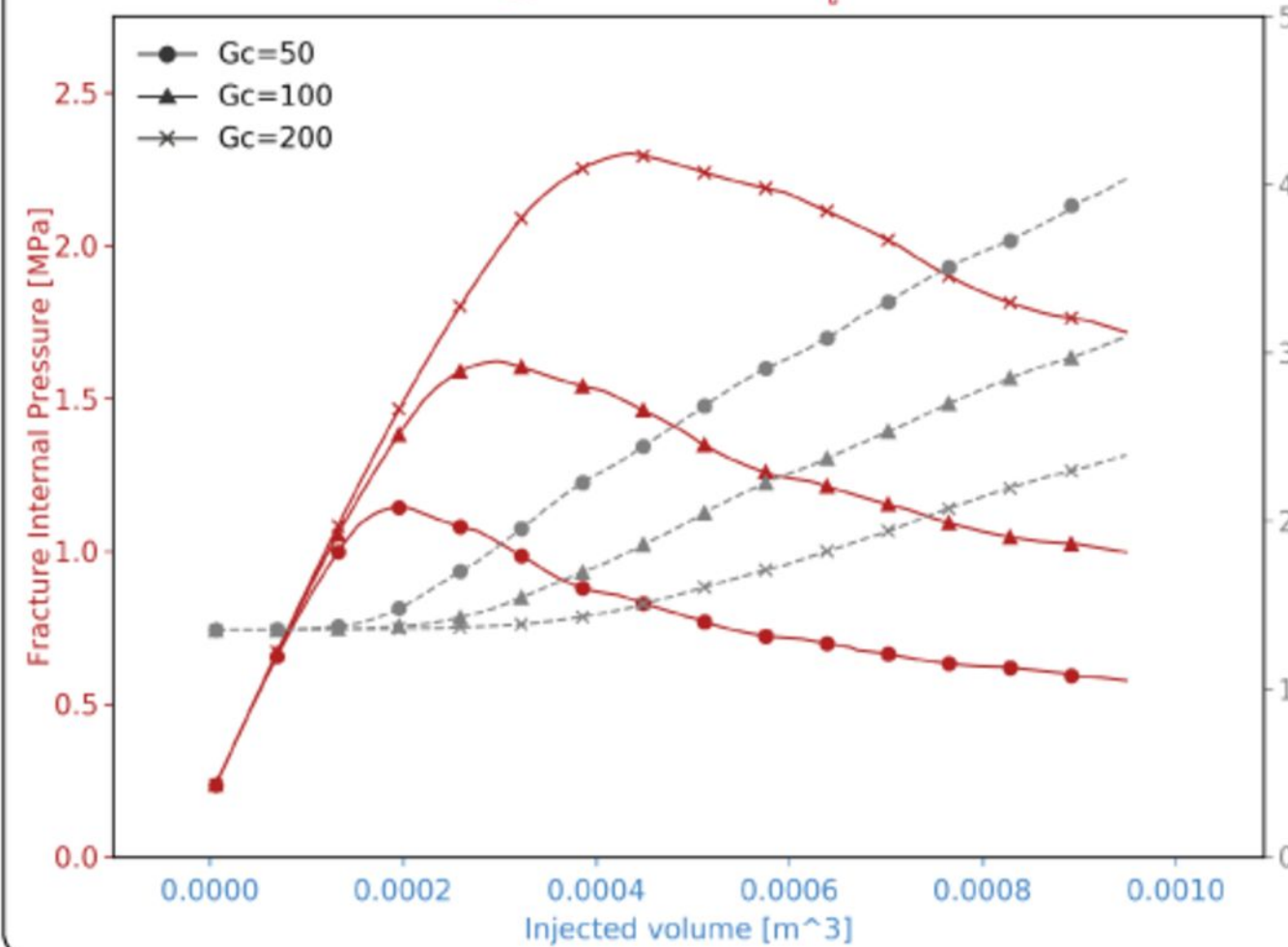
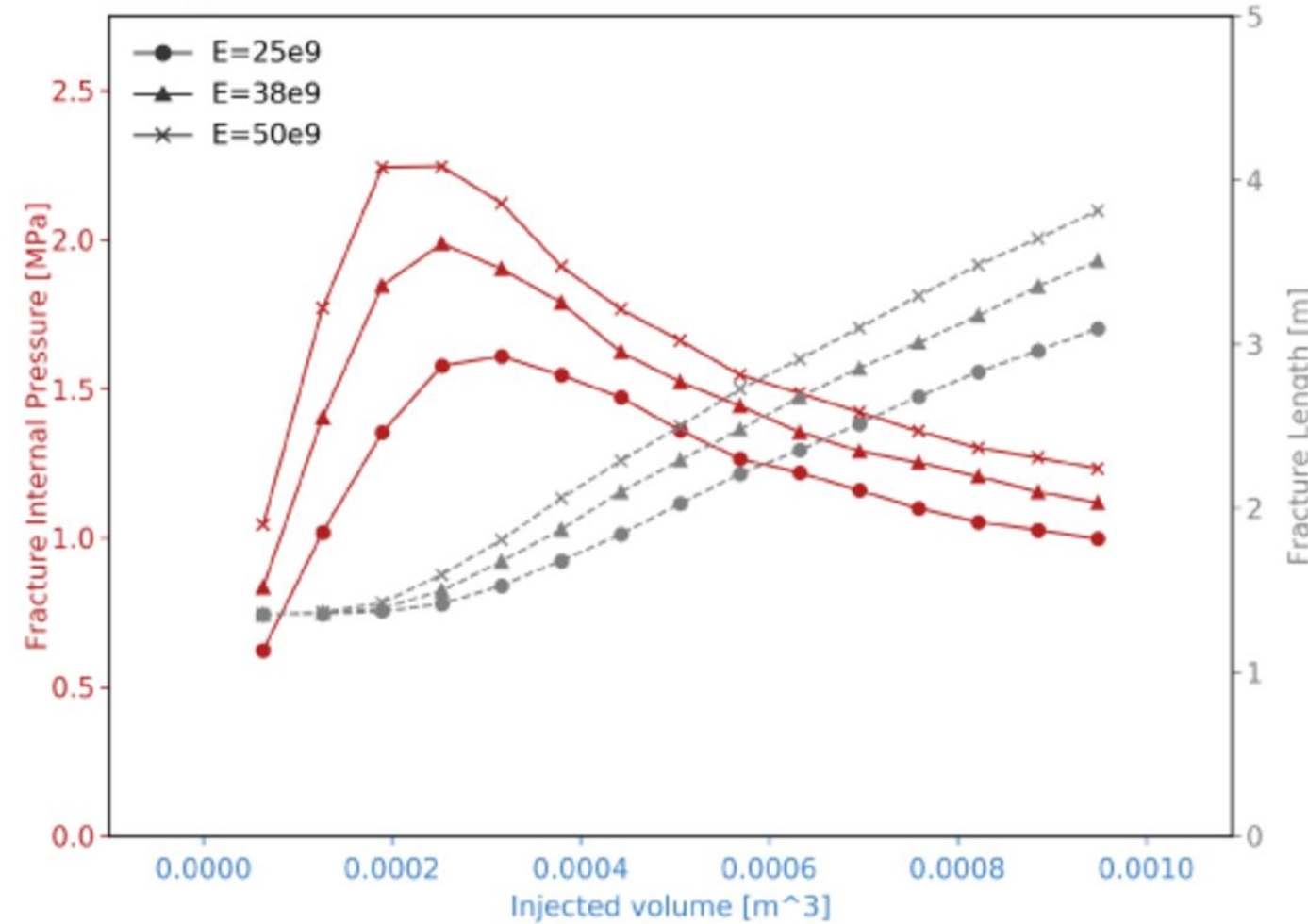
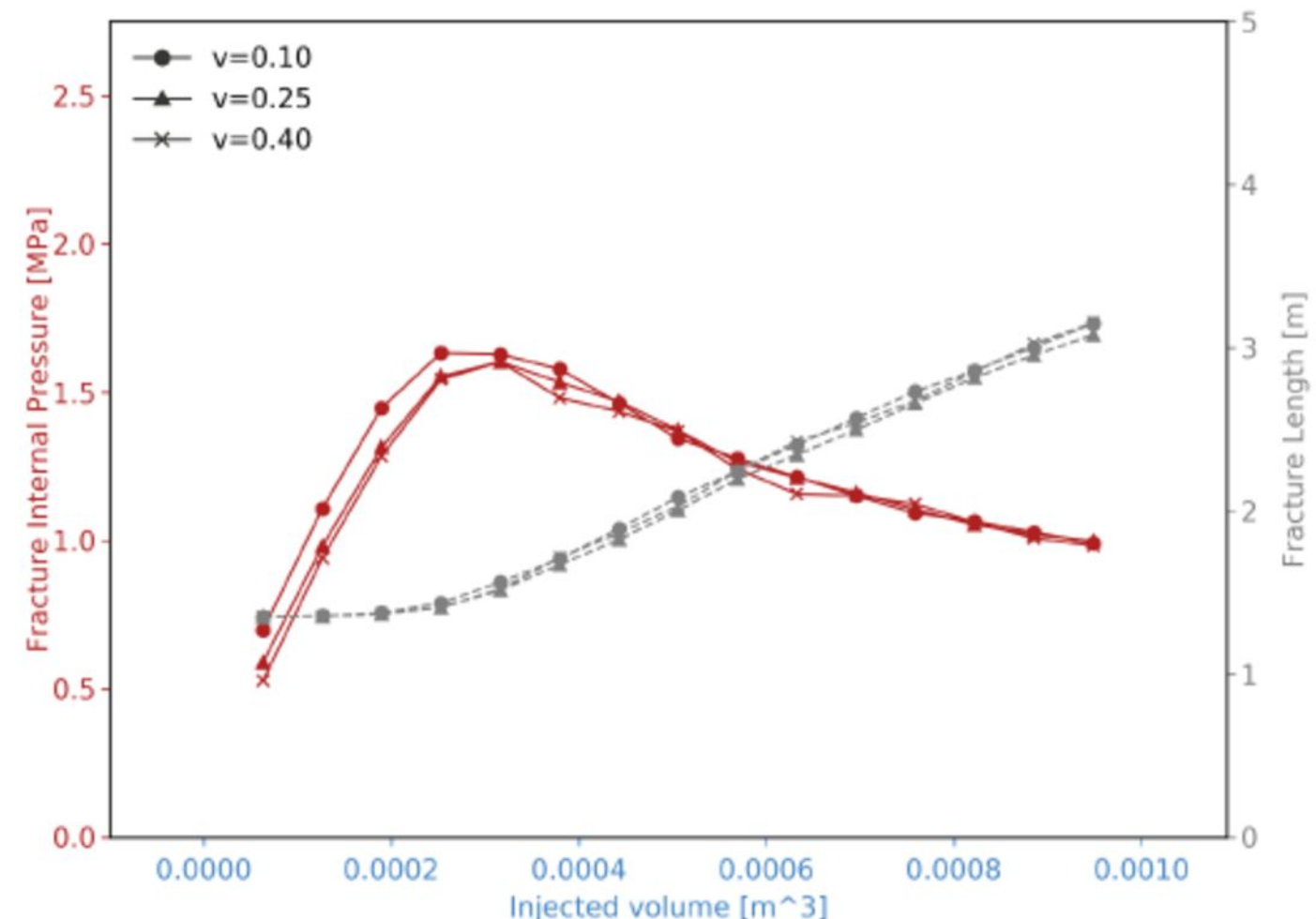
a Griffith's critical energy release rate (G_c)**b** Young's modulus (E)**c** Poisson's ratio (ν)

Figure 5.

NF [$G_c=0.01$]

NF [$G_c=0.05$]

NF [$G_c=0.1$]

NF [$G_c=10$]

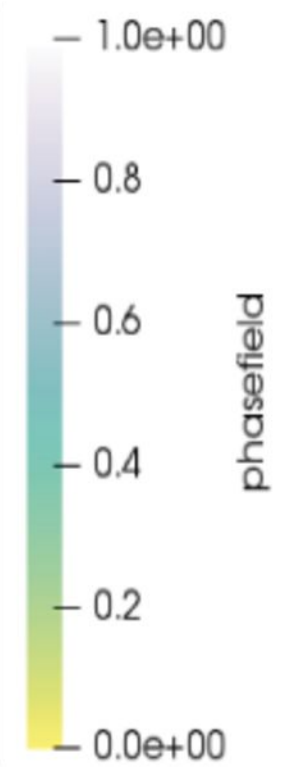
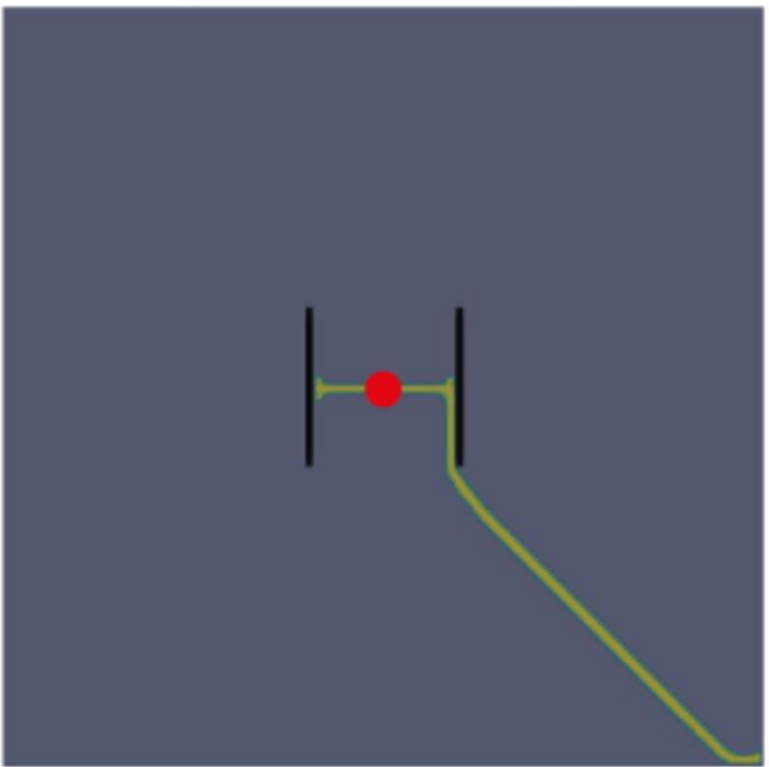
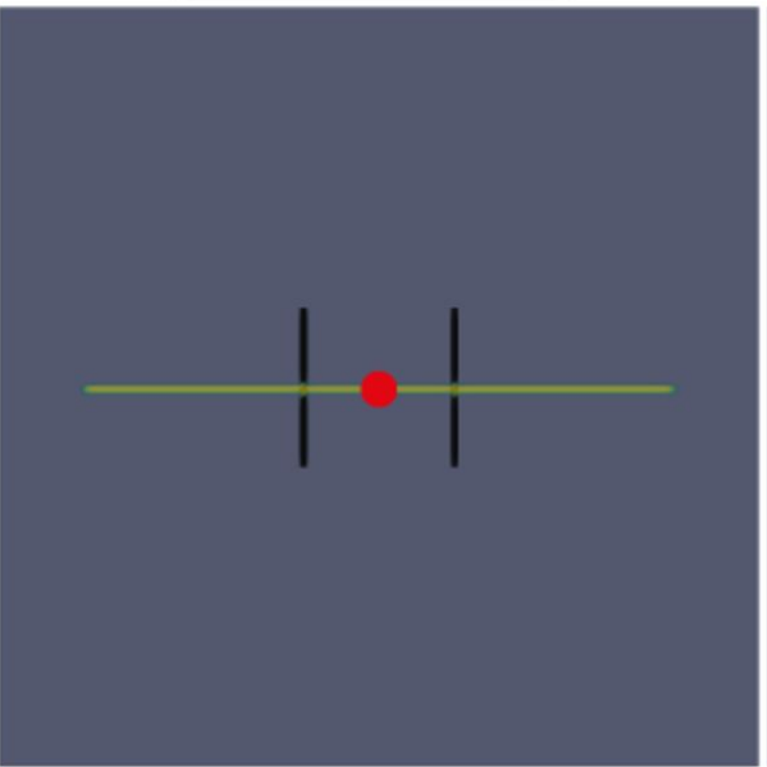
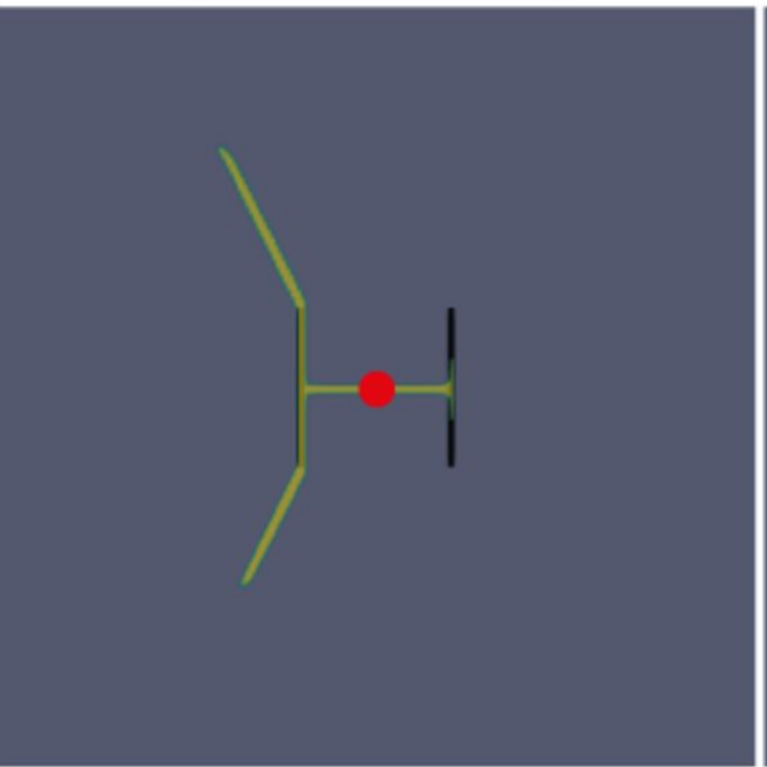
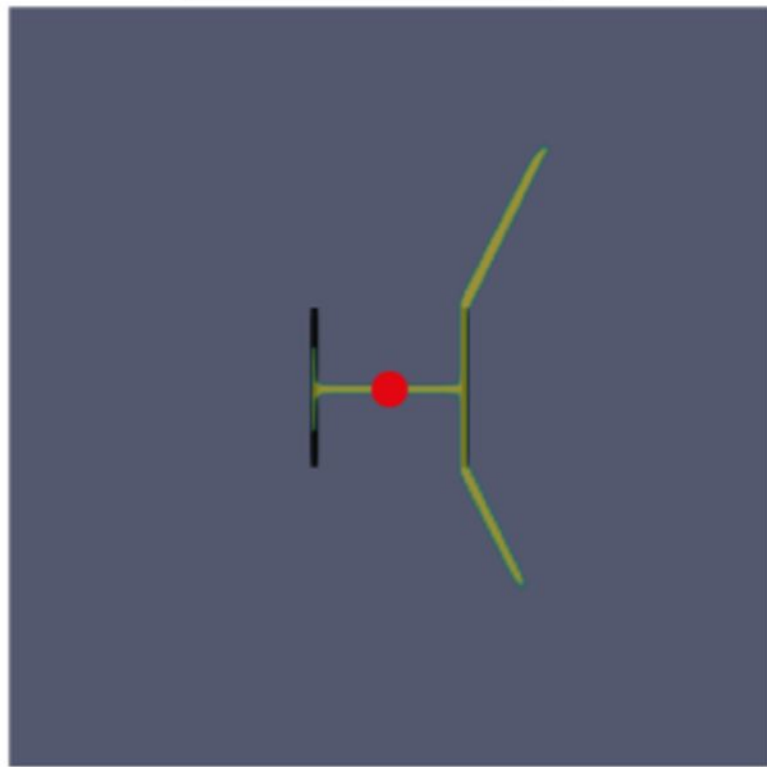
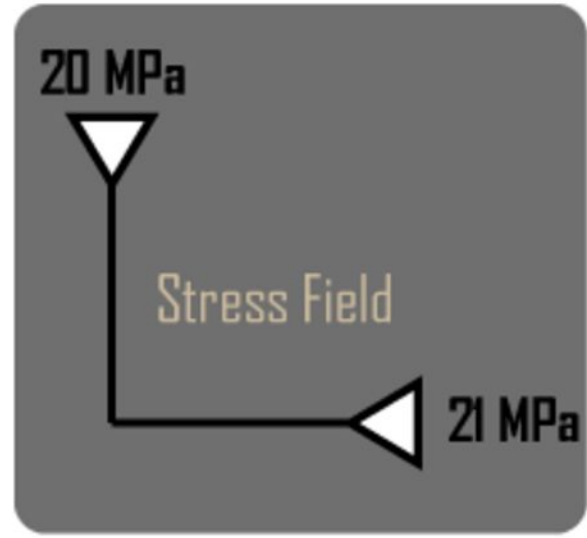
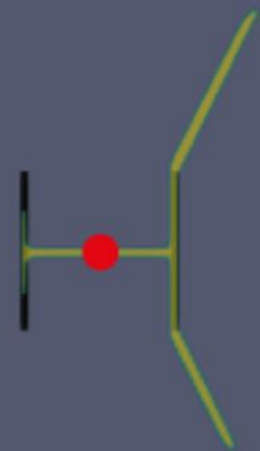


Figure 6.

NF [$G_c=0.01$]

$$S_{Hmax} = 21 \text{ MPa}$$



$$S_{Hmax} = 30 \text{ MPa}$$



$$S_{Hmax} = 40 \text{ MPa}$$



$$S_{Hmax} = 60 \text{ MPa}$$

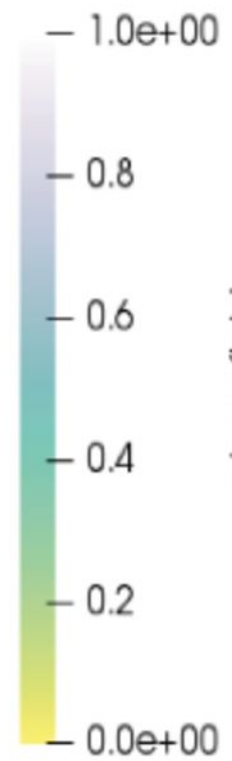
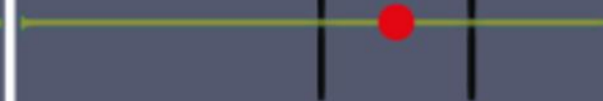


Figure 7.

a

NF [$G_c=0.01$]NF [$G_c=0.1$]NF [$G_c=10$]

20 MPa

Stress Field

21 MPa

- 1.0e+00

- 0.8

- 0.6

- 0.4

- 0.2

- 0.0e+00

phasefield

b

 $S_{Hmax} = 21$ MPa $S_{Hmax} = 30$ MPa $S_{Hmax} = 40$ MPa $S_{Hmax} = 60$ MPaNF [$G_c=0.01$]

- 1.0e+00

- 0.8

- 0.6

- 0.4

- 0.2

- 0.0e+00

phasefield

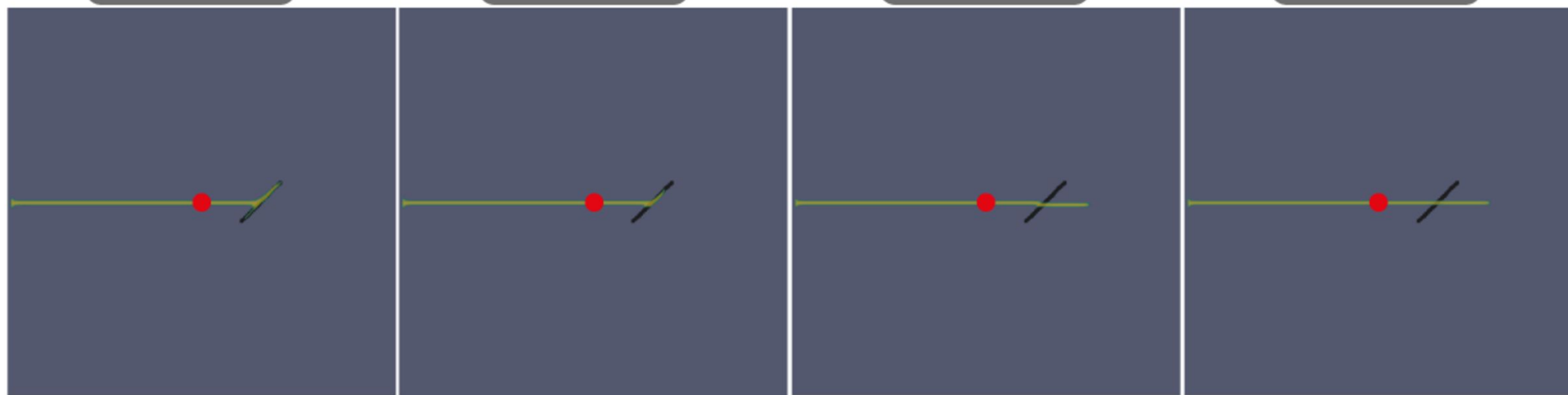
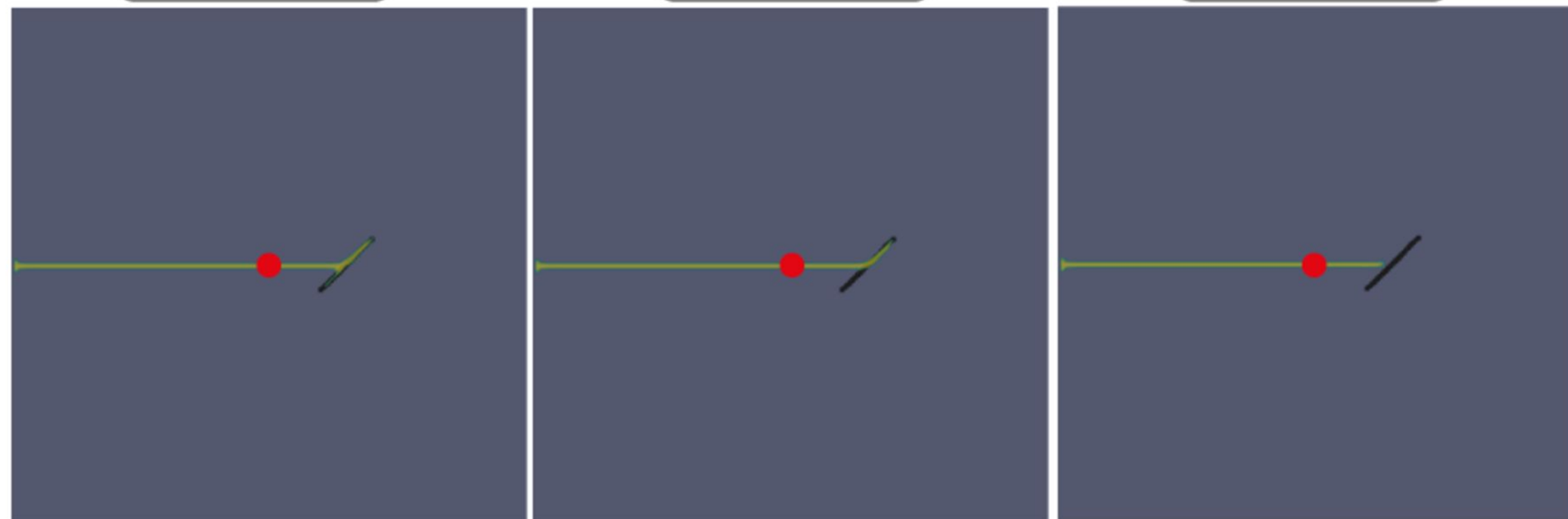
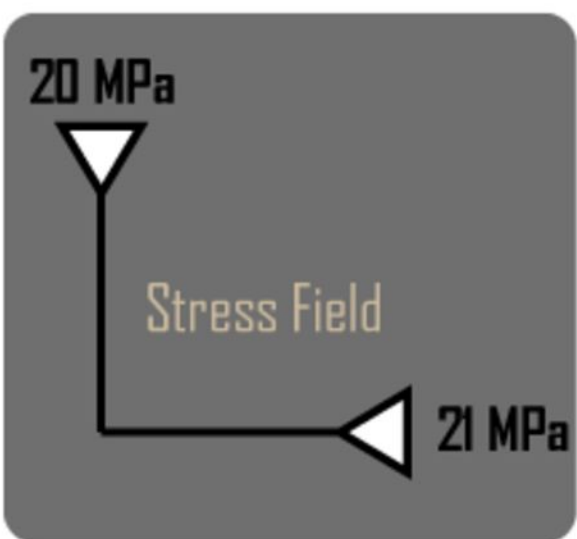
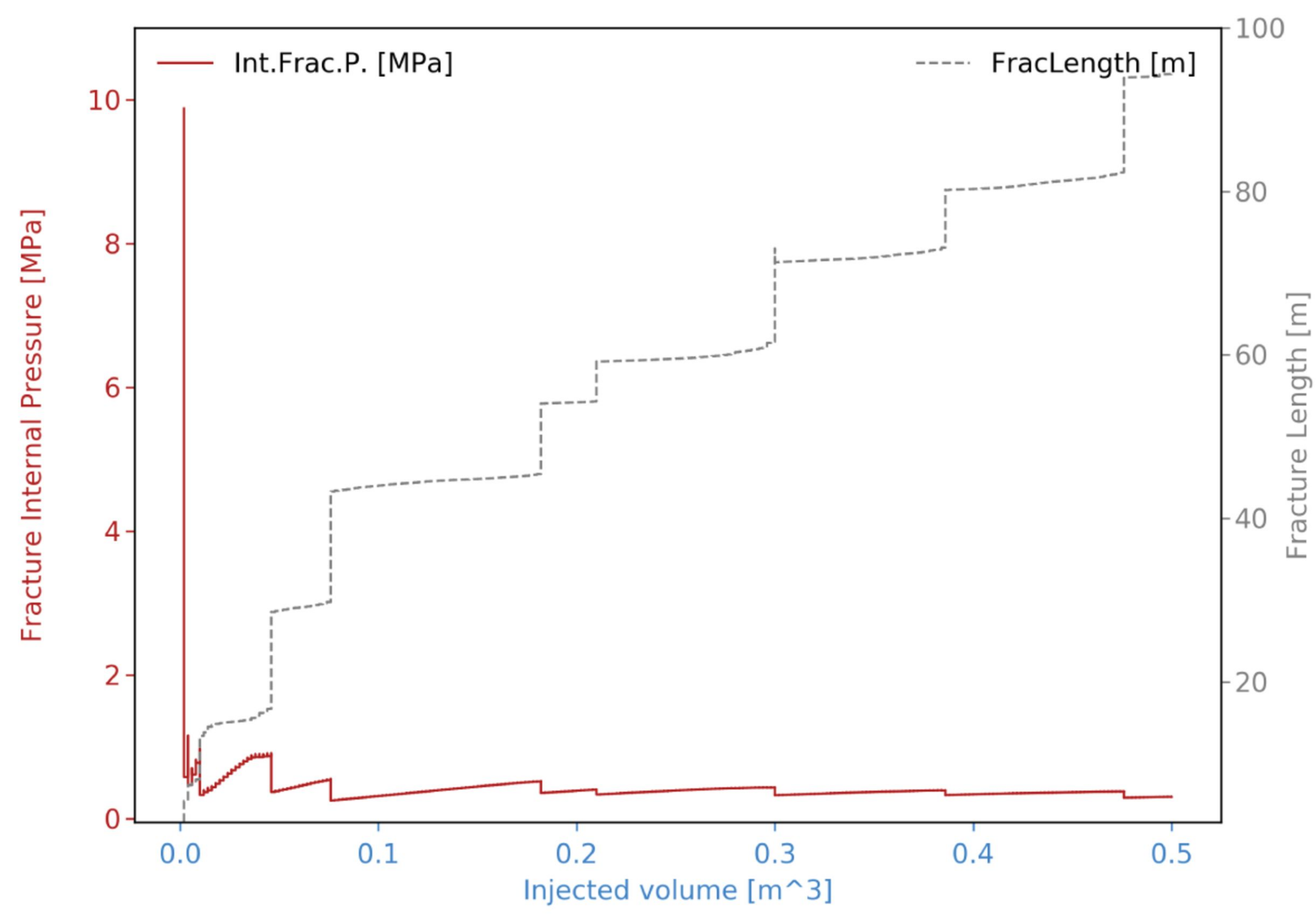
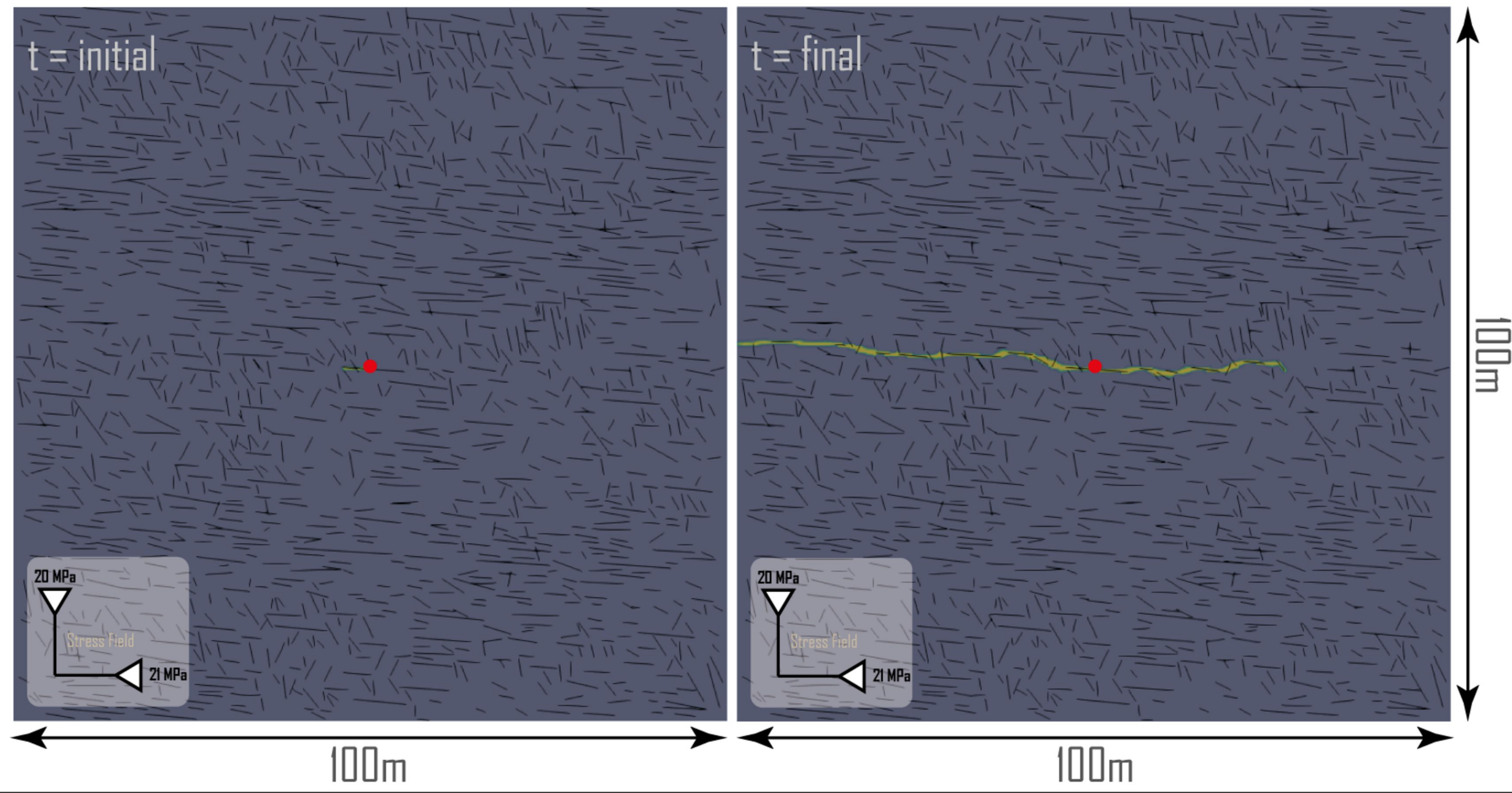
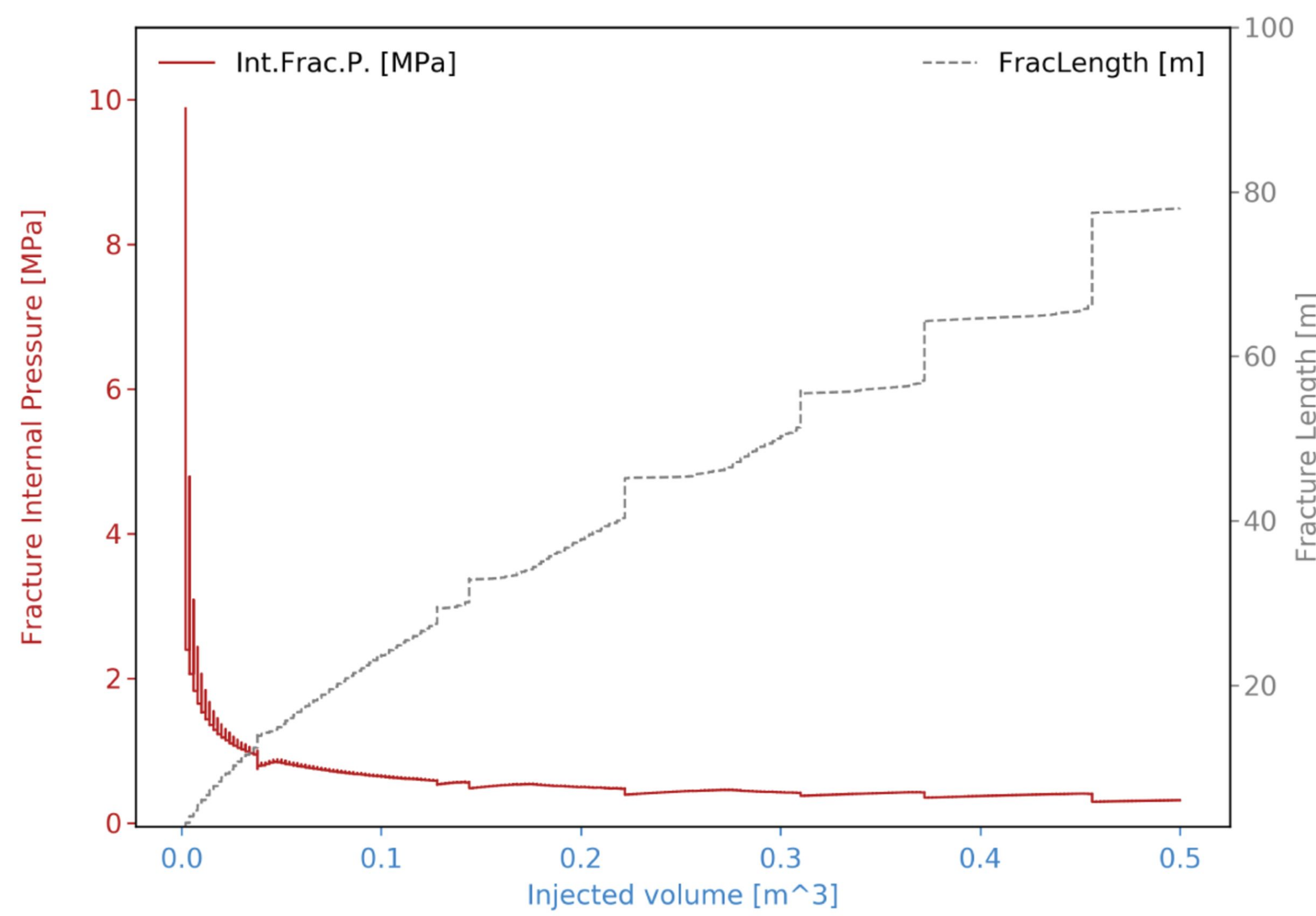
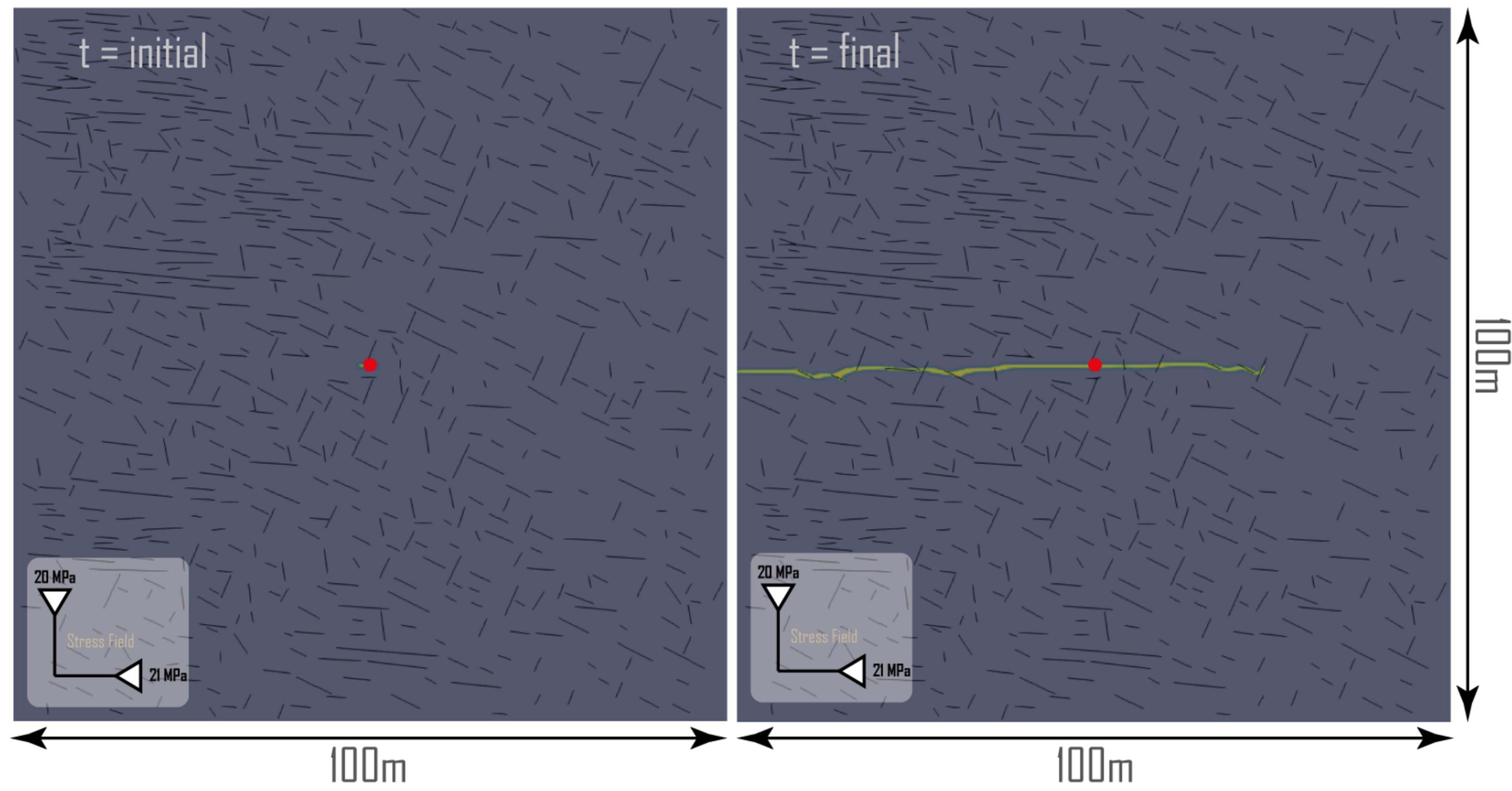


Figure 8.

HF propagation plot

 $\Omega + \Gamma$ Limestone: Lm01

HF propagation plot

 $\Omega + \Gamma$ Limestone: Lm02

HF propagation plot

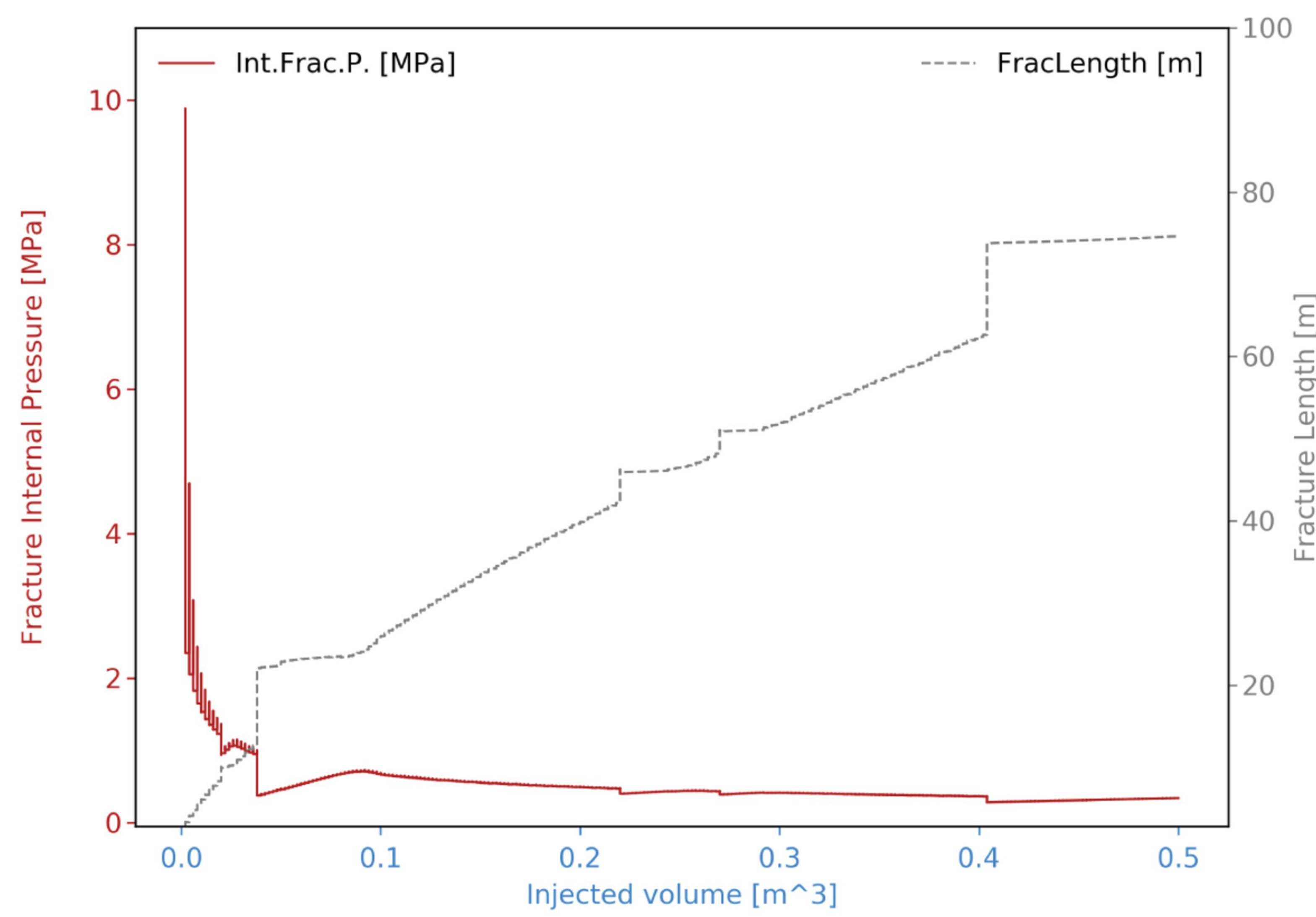
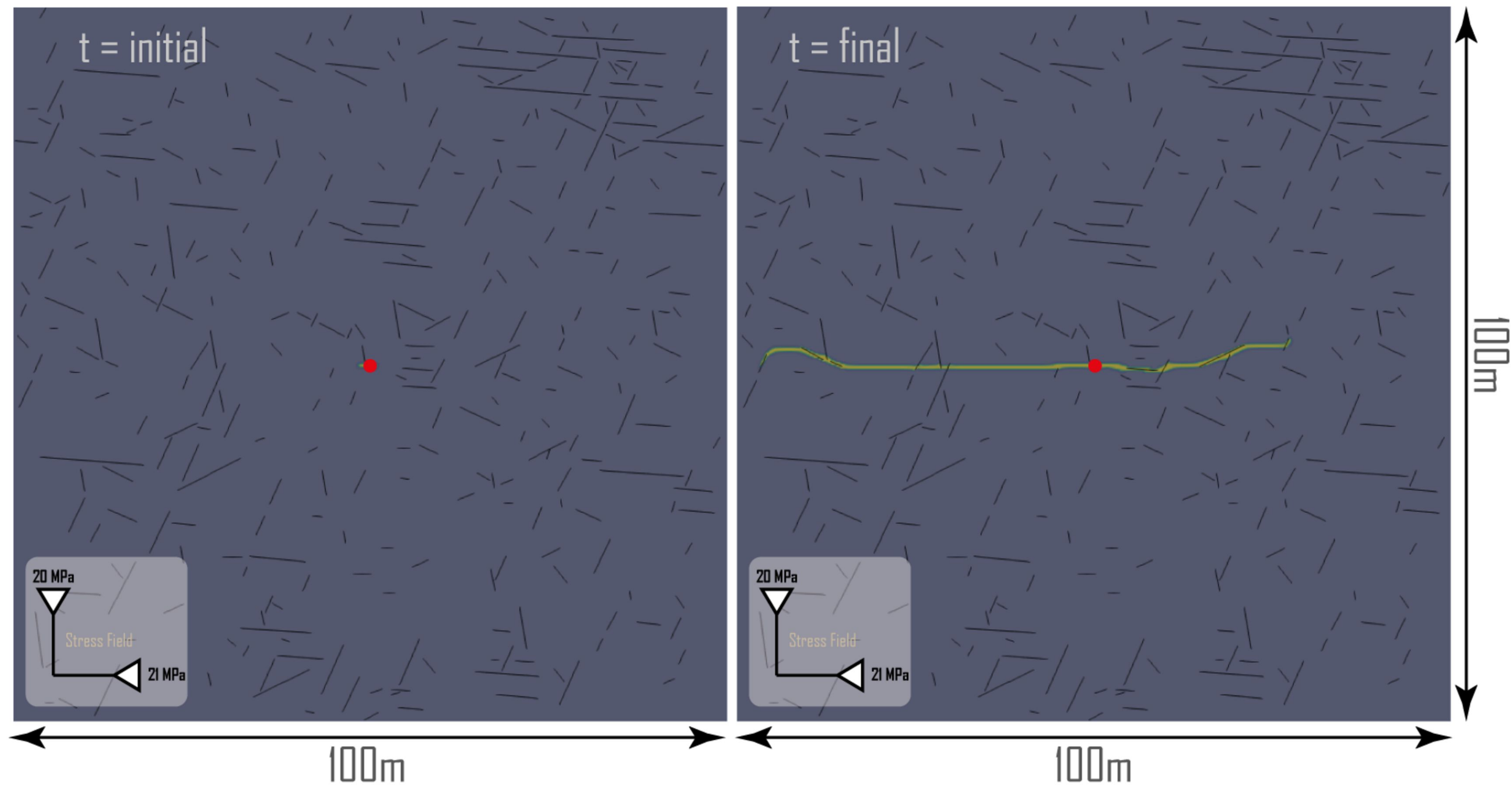
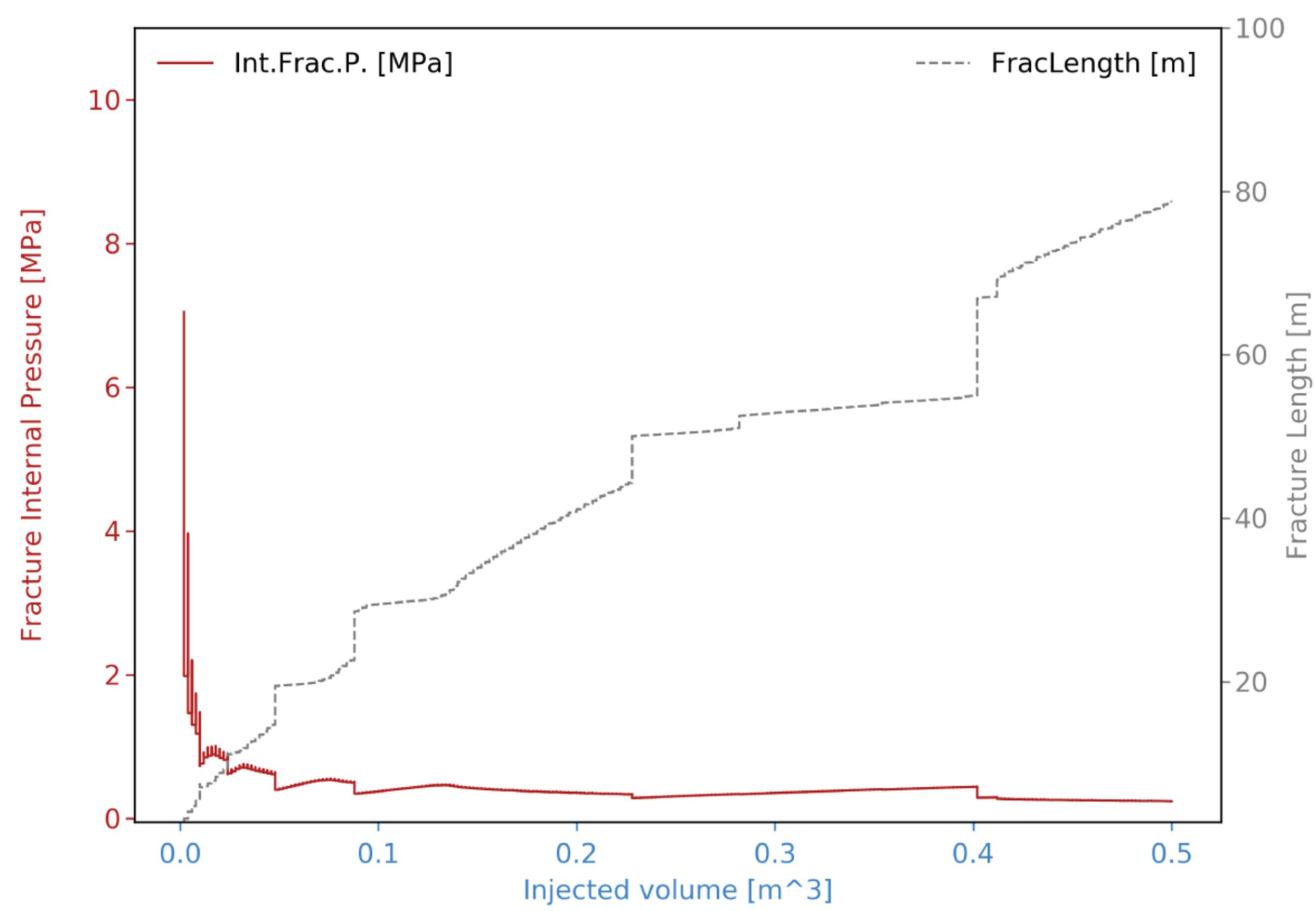
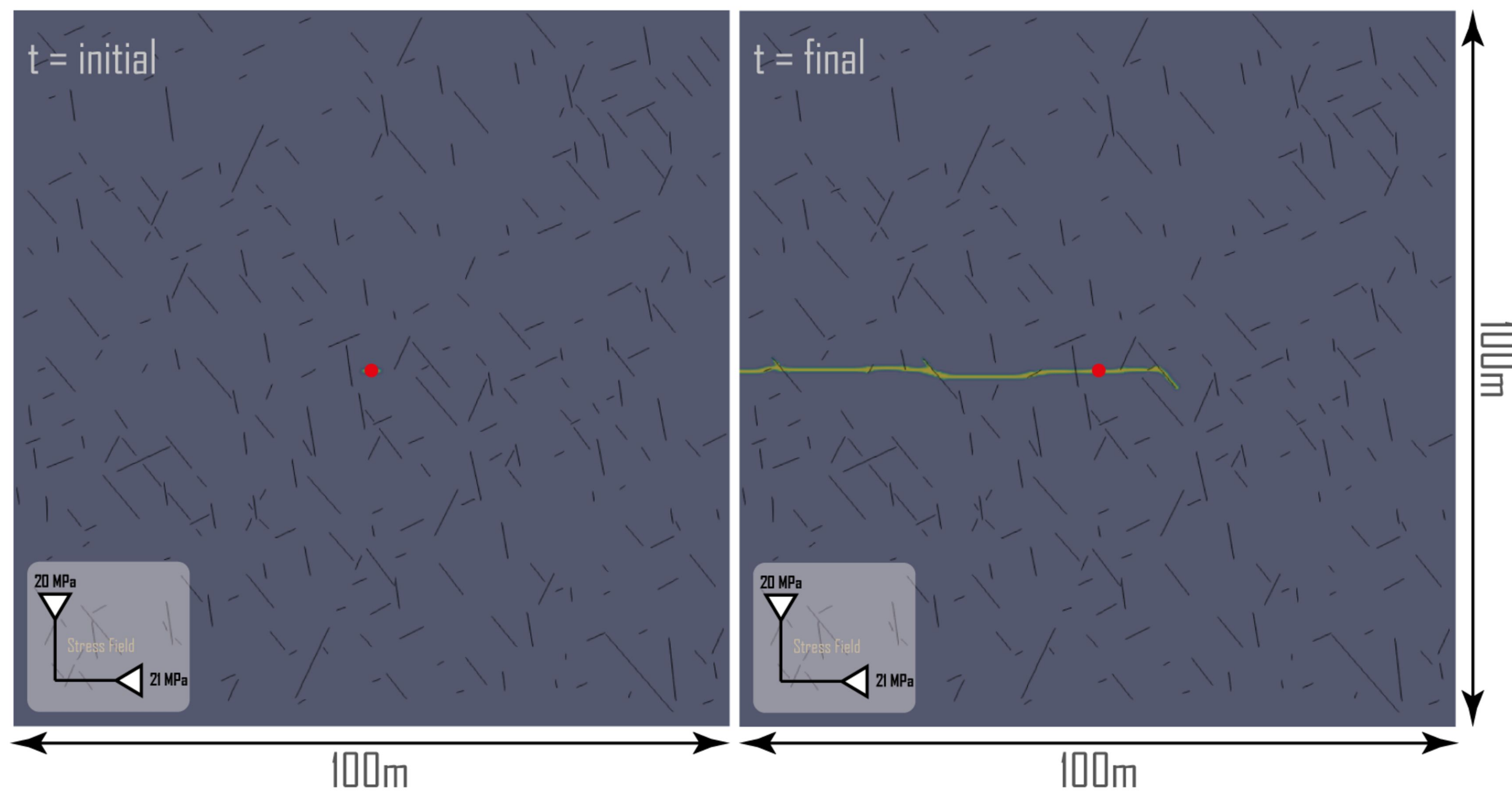
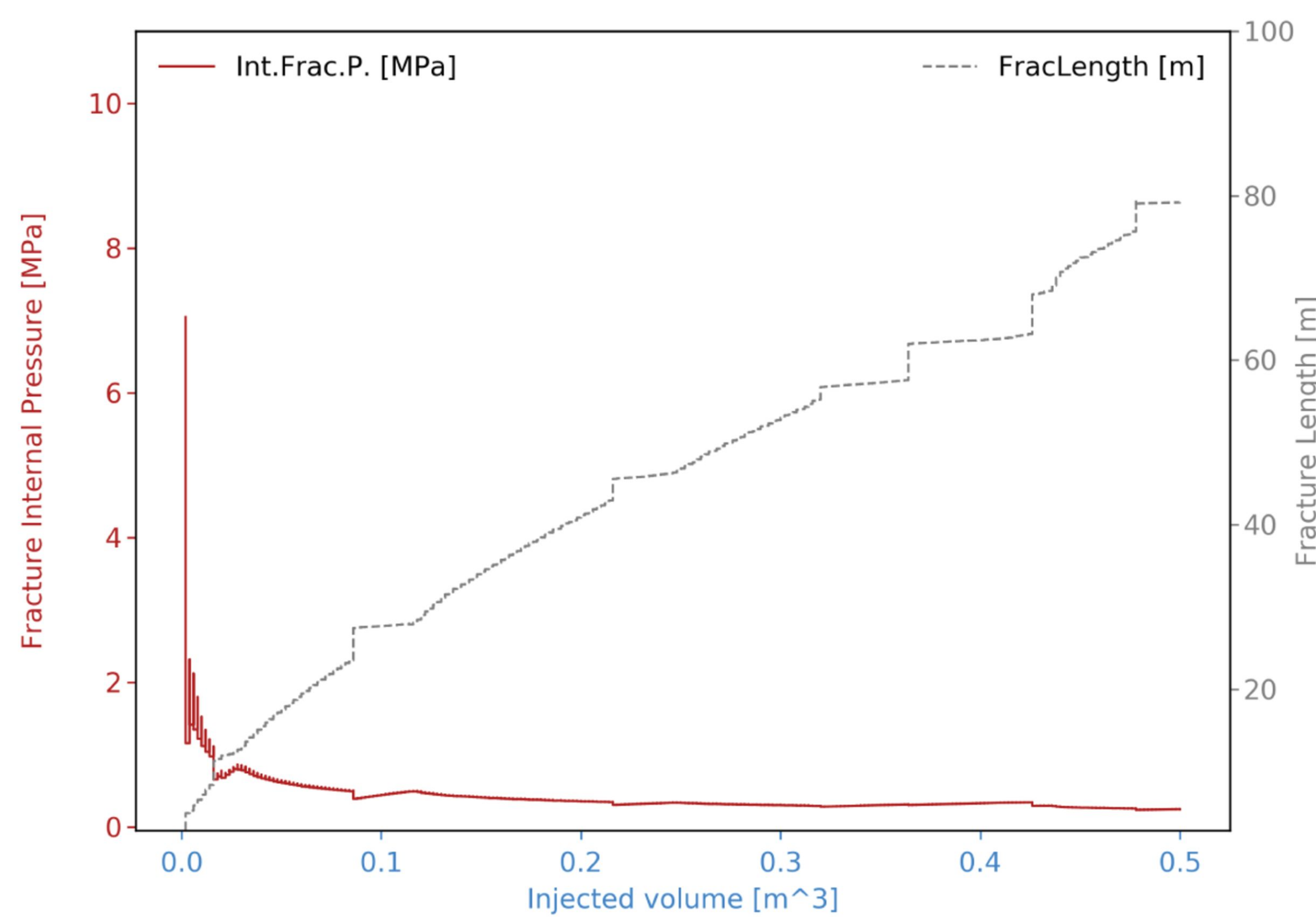
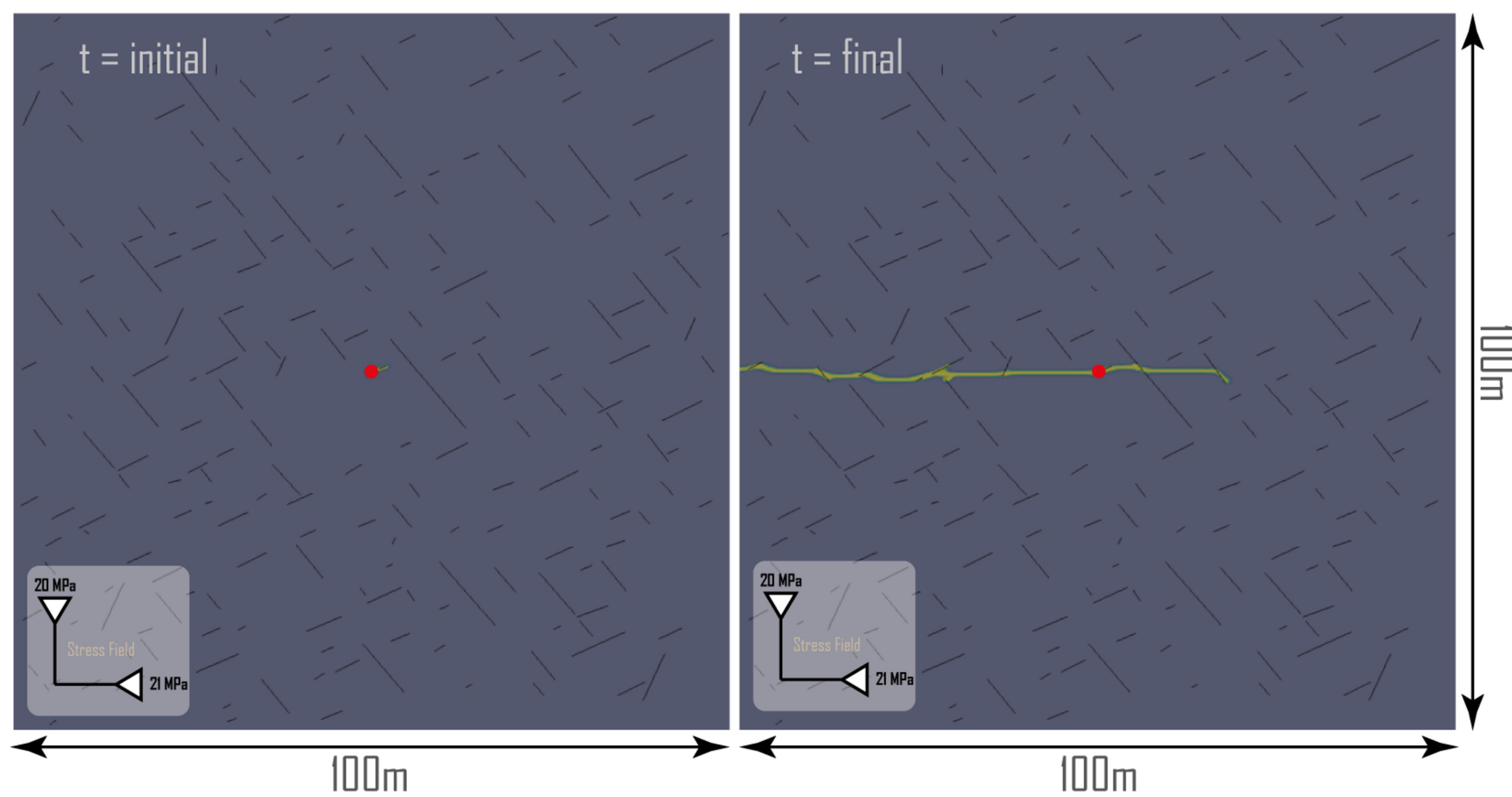
 $\Omega + \Gamma$ Limestone: Lm03

Figure 9.

HF propagation plot

 $\Omega + \Gamma$ Marble: Ma01

HF propagation plot

 $\Omega + \Gamma$ Marble: Ma02

HF propagation plot

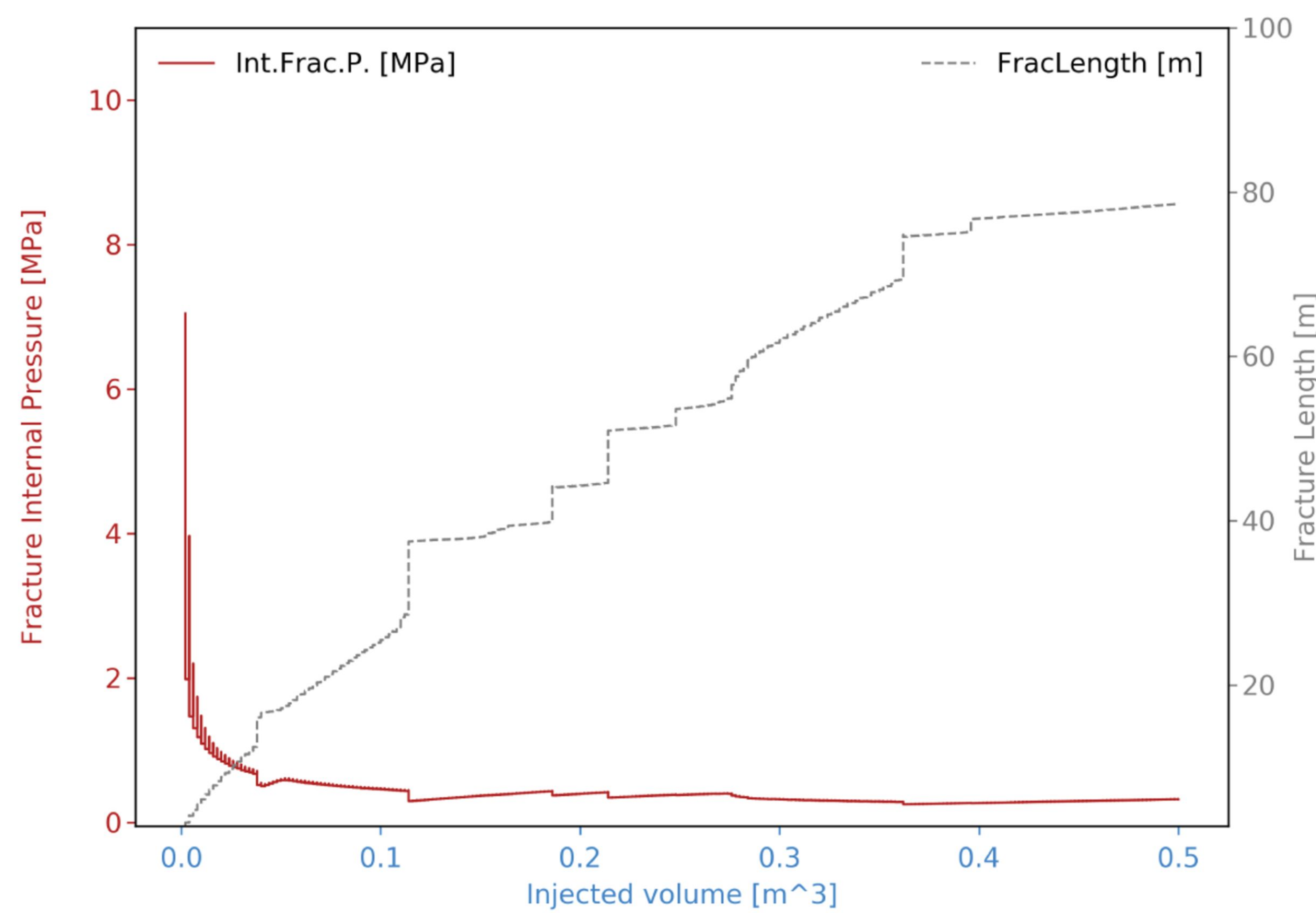
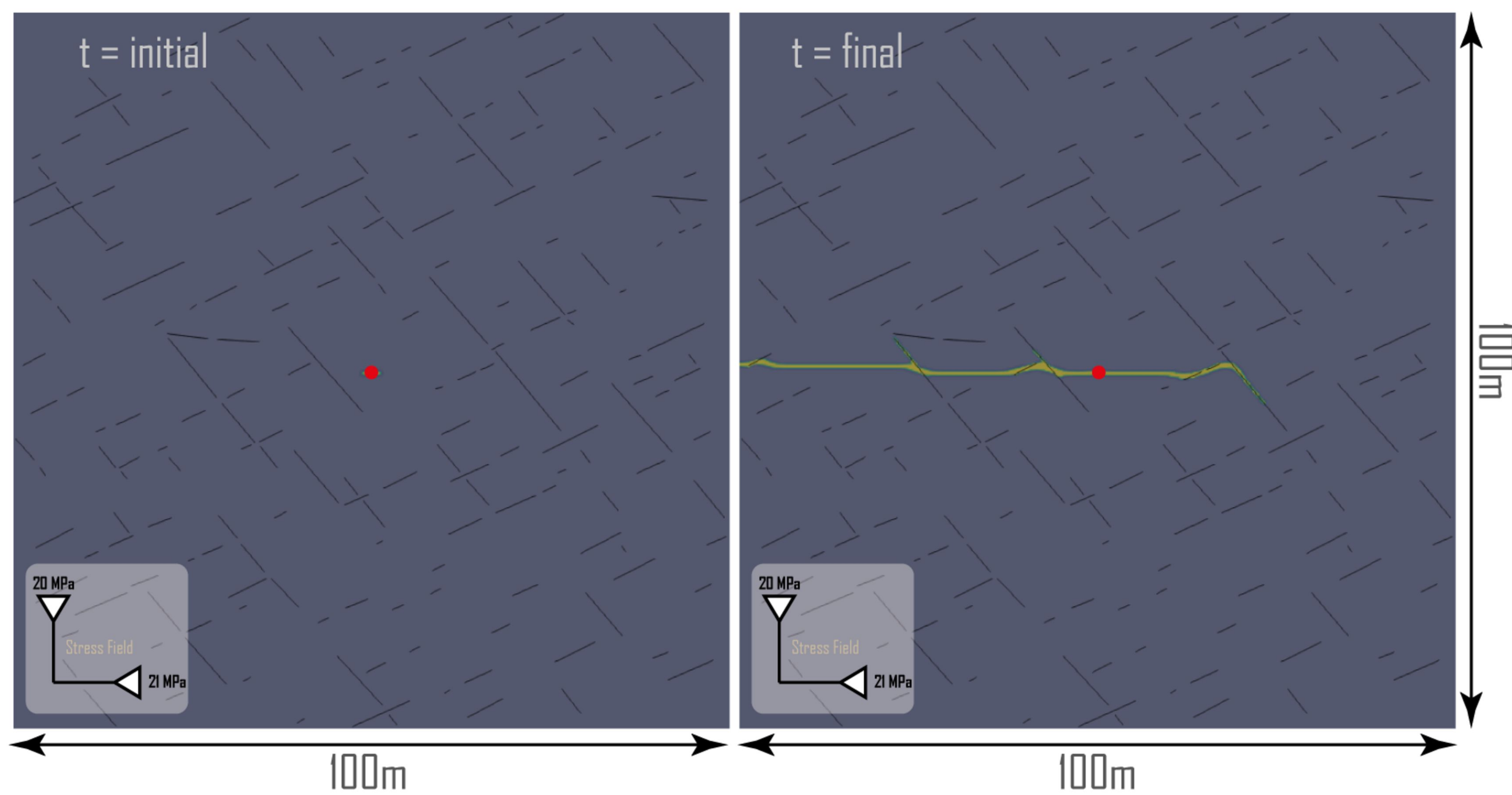
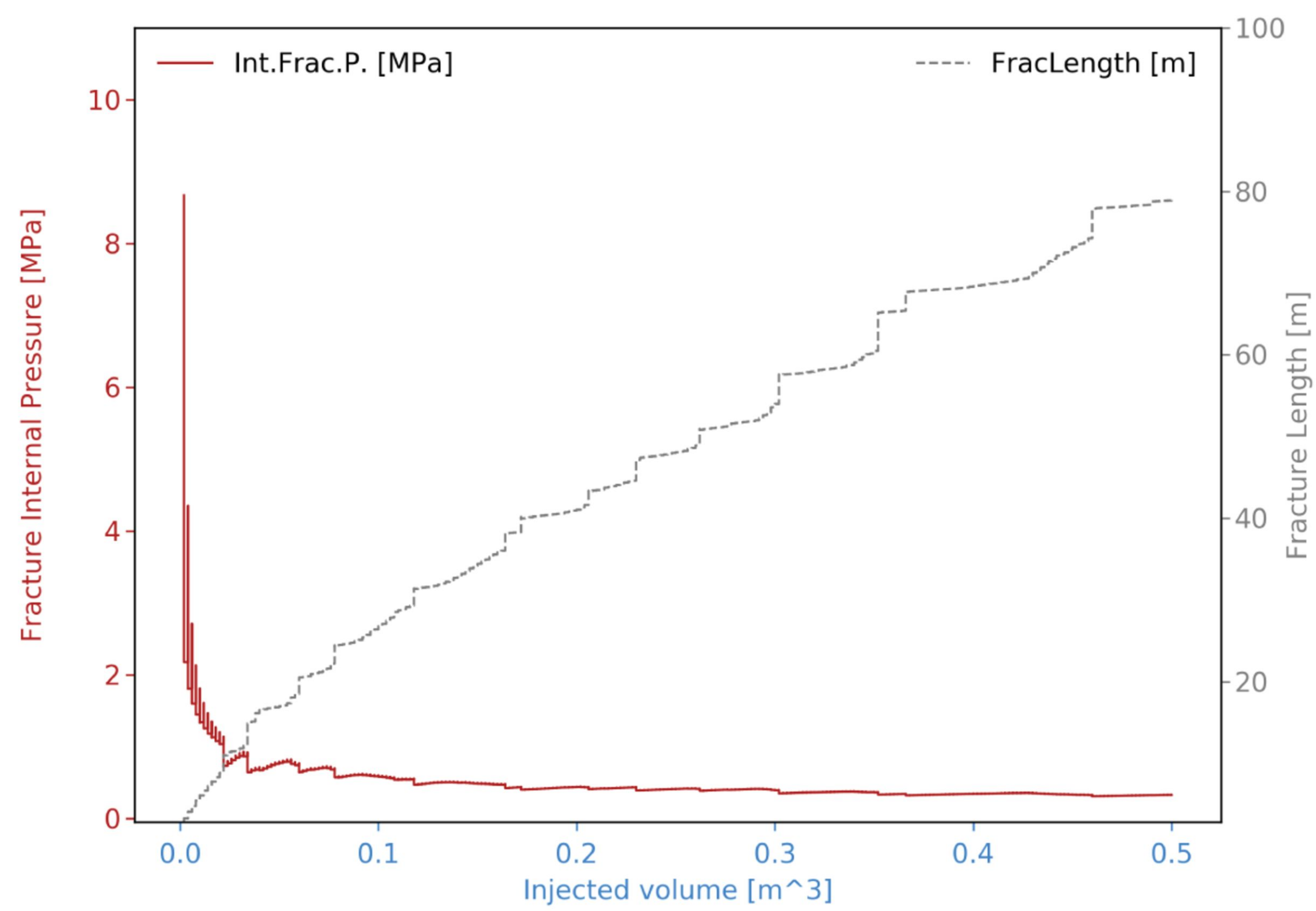
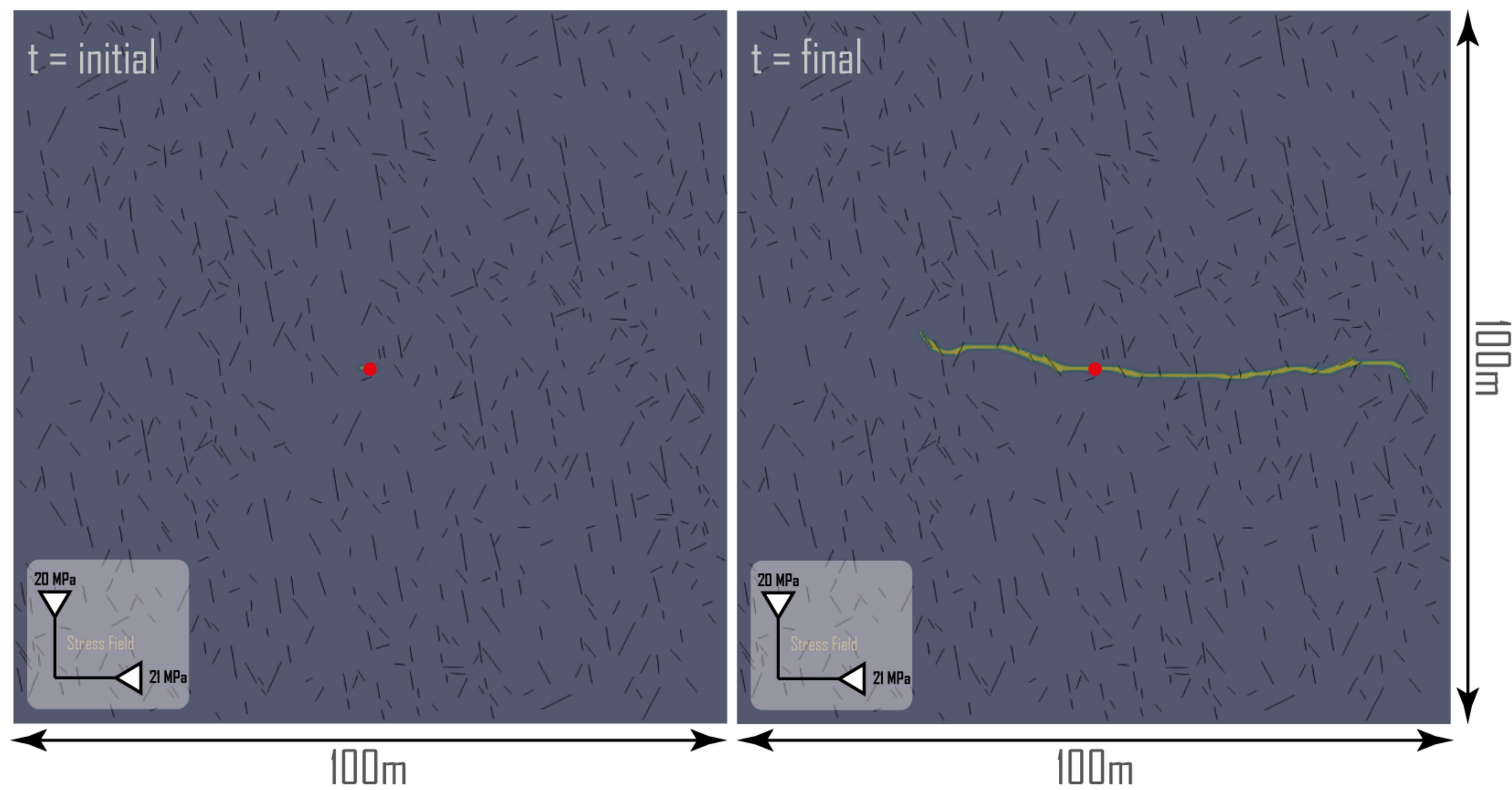
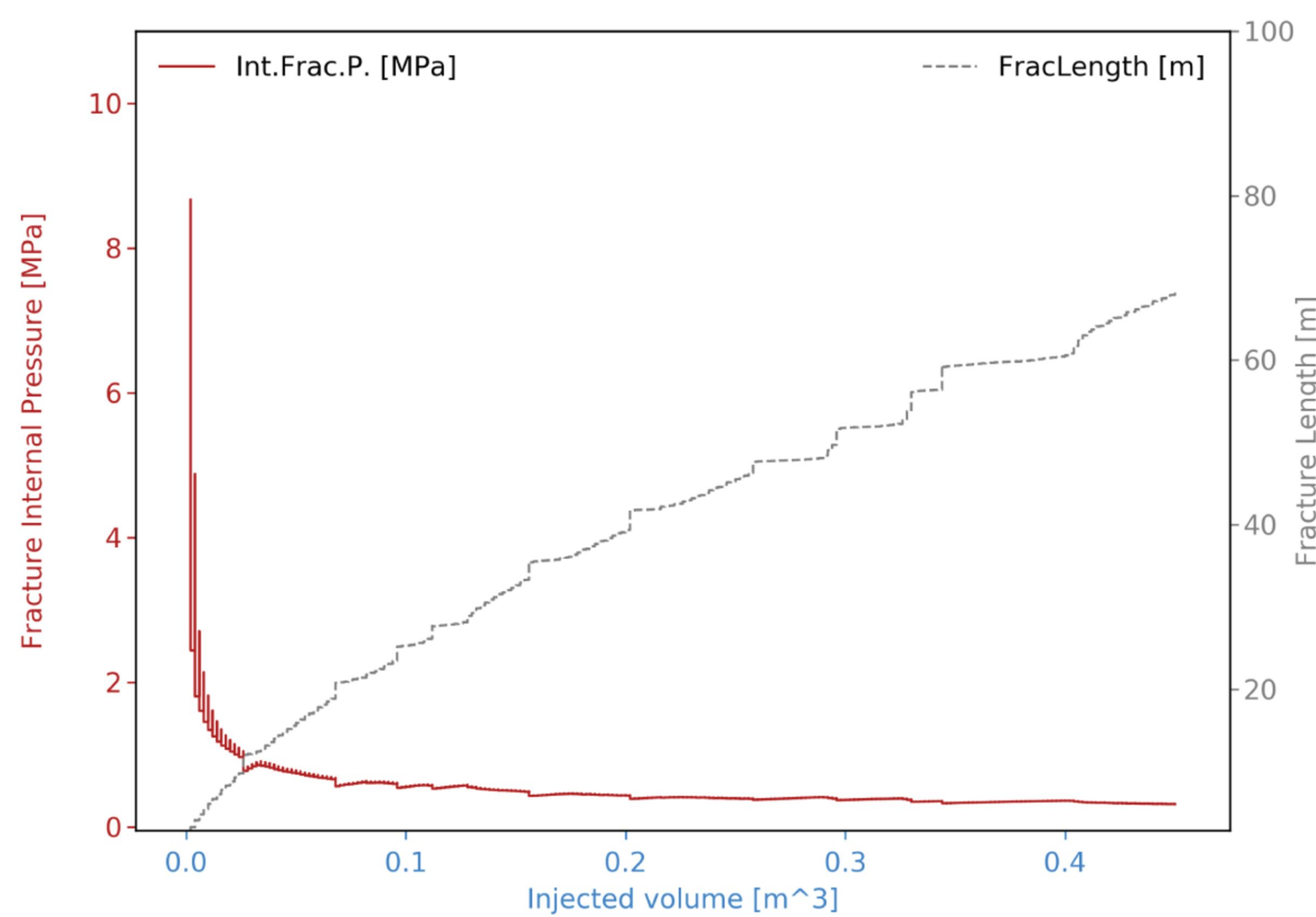
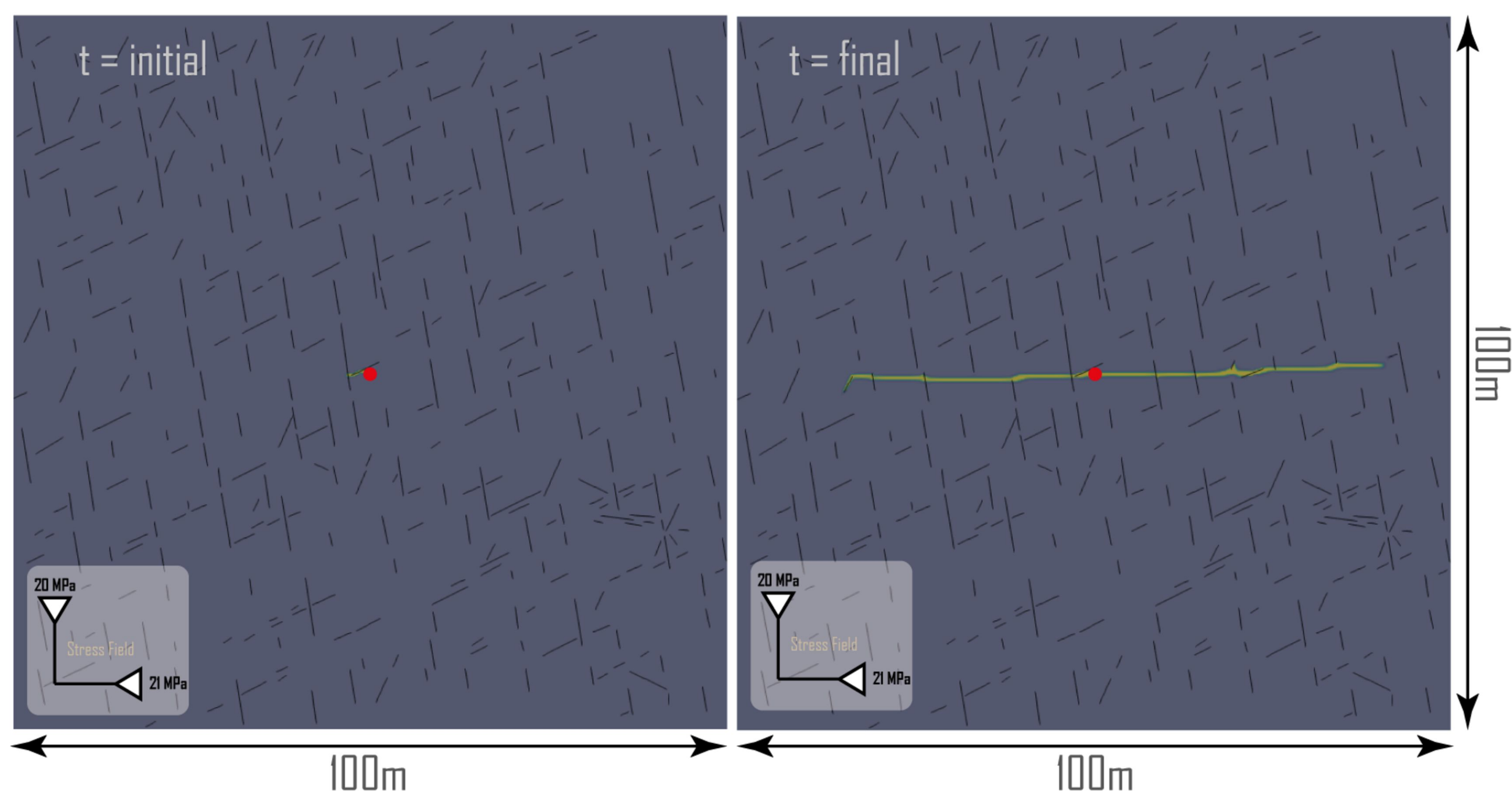
 $\Omega + \Gamma$ Marble: Ma03

Figure 10.

HF propagation plot

 $\Omega + \Gamma$ Skarn: Sk01

HF propagation plot

 $\Omega + \Gamma$ Skarn: Sk02

HF propagation plot

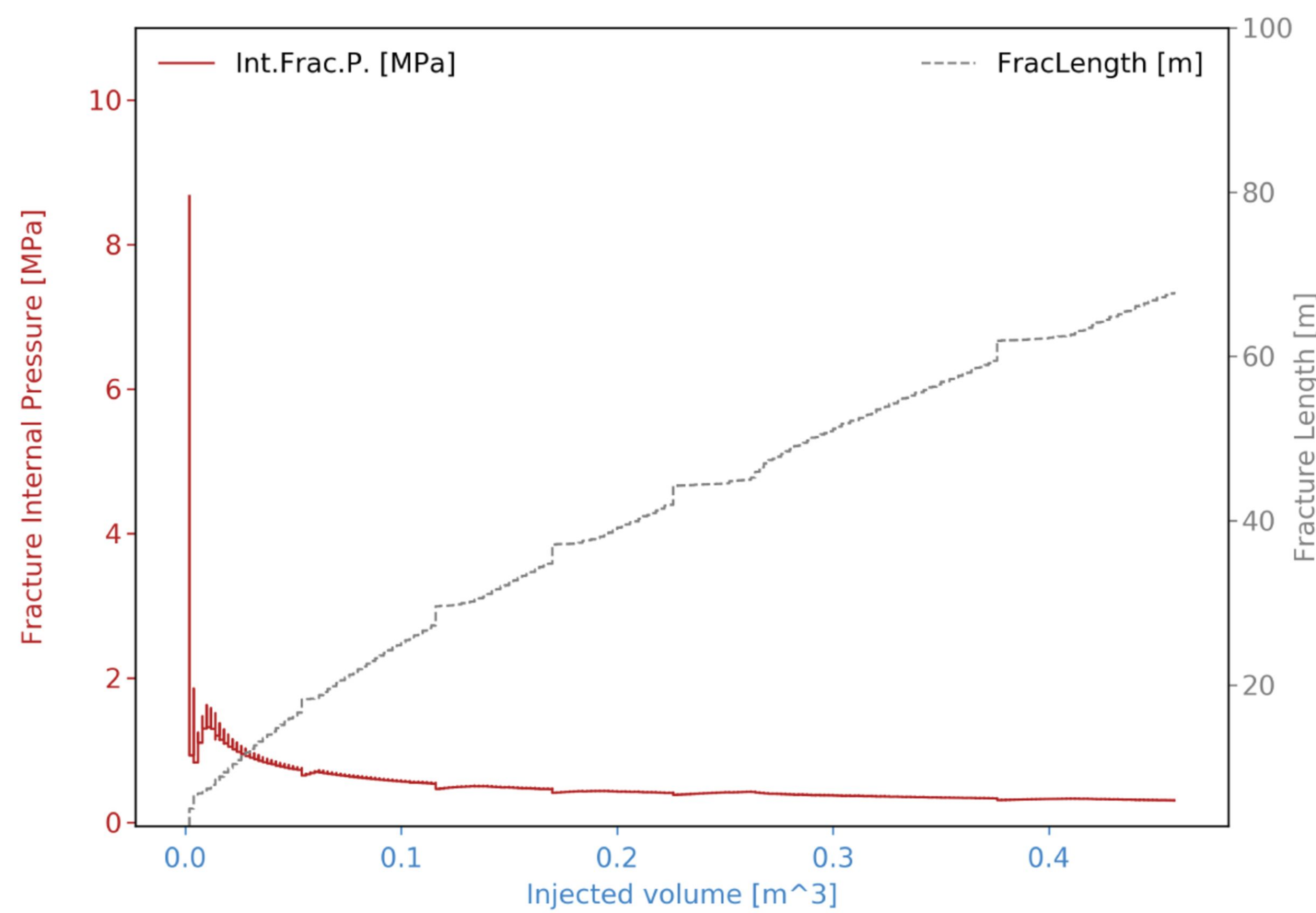
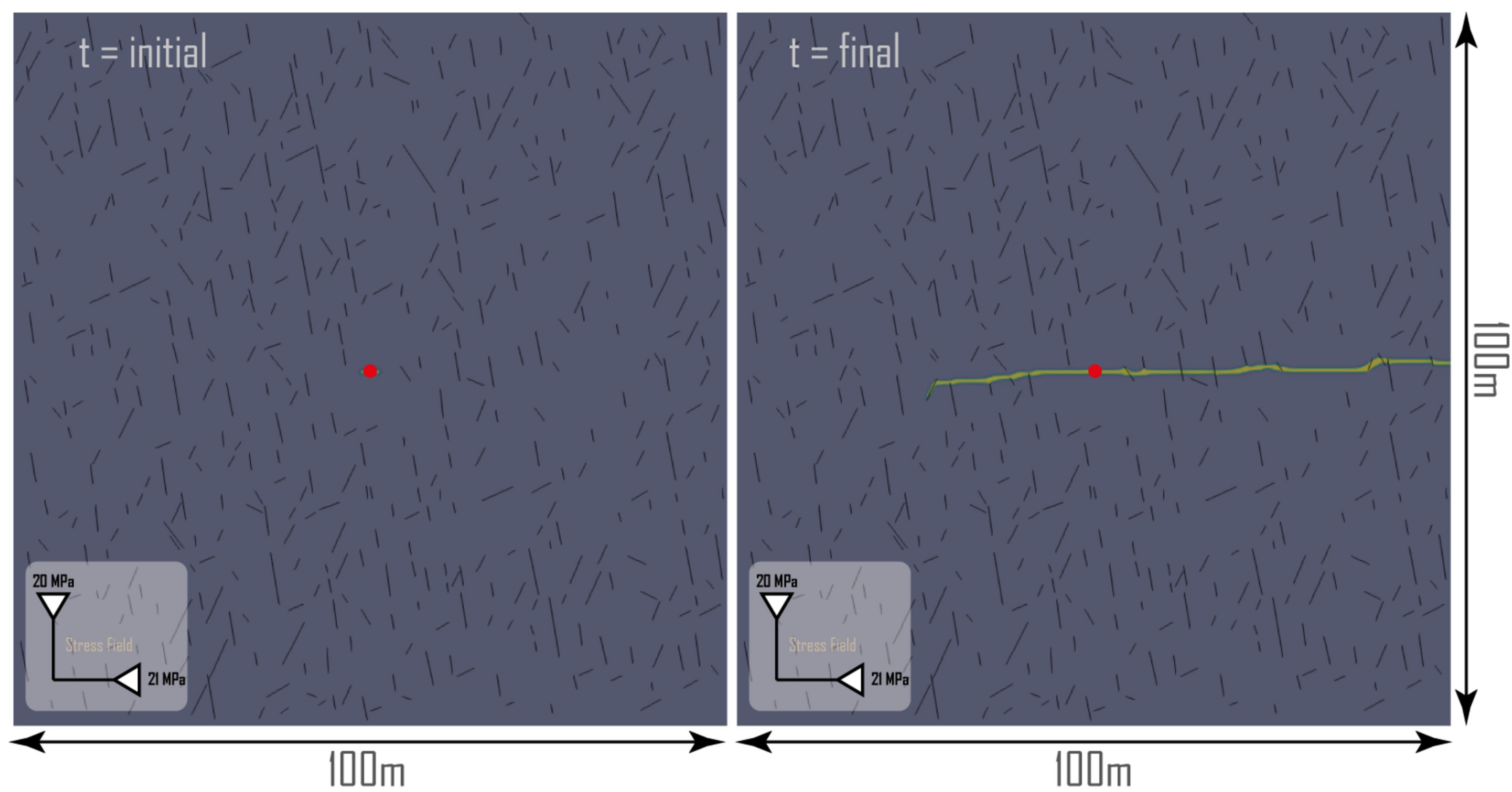
 $\Omega + \Gamma$ Skarn: Sk03

Figure 11.

